THEORETICAL INVESTIGATIONS IN NUCLEAR OPTICAL MODEL WITH SPECIAL REFERENCE TO ANTIPROTON-NUCLEUS AND NUCLEUS-NUCLEUS SCATTERINGS

ABSTRACT

BASABADUTTA DEY

DEPARTMENT OF PHYSICS
SCHOOL OF PHYSICAL SCIENCES

A THESIS
SUBMITTED
IN
FULFILMENT OF THE REQUIREMENT FOR THE DEGREE OF

DOCTOR OF PHILOSOPHY

To

THE NORTH-EASTERN HILL UNIVERSITY

SHILLONG - 793 001

INDIA

JULY, 1991

Phy
(Thesis)

ABSTRACT

The optical model for nuclear scattering is very important to analyse the elastic and reaction cross sections in the nucleon-nucleus and nucleus-nucleus scatterings. In this approach, the nucleon-nucleus and nucleus-nucleus systems can be treated as a two body problem governed by complex effective interaction. This effective interaction is known as the optical potential. The availability of many reaction channels in addition to elastic channel in the nuclear scattering leads to the complex effective interaction in the nucleon-nucleus or the nucleus-nucleus scattering. The imaginary part of the complex potential is responsible for the removal of the flux from the incident beam leading to reaction and other non-elastic processes. Thus, the potential based on optical model is a useful tool for the study of nucleon-nucleus and nucleus-nucleus scatterings.

Recently, the production of antiproton ($\bar{p}$) beams with high flux and good resolution from the LEAR facility at CERN has opened up a new and wider field of research work. Due to the advent of the LEAR facility exploration of nucleus using antiproton as probes has become possible. The study of $\bar{p}$-A scattering is of great importance because it may generate new information on nuclear structure, antiproton-nucleus interaction, strange particle production etc. Atomic type bound states of antiproton with the nucleus has generated antiprotonic atom physics research.

We have studied several aspects of low energy $\bar{p}$-nucleus collisions based on some of the experimental results which have become available. In Chapter 2, a brief review of various aspects of low energy $\bar{p}$-nucleus collision, which forms the background for our work, is discussed.

Experimental results and theoretical analyses carried out so far provide interesting similarities between antiproton-nucleus ($\bar{p}$-A) scattering and heavy ion scattering (HIS). The angular distribution of $\bar{p}$-A systems shows a diffraction pattern which is similar to the Fraunhofer diffraction occuring in several cases of HIS. This is in contrast with the corresponding case of proton-nucleus scattering at the same energy. Moreover, both (HIS as well as $\bar{p}$-A) the scattering processes are surface dominant. These similarities indicate that some of the techniques developed for the analysis of HIS can also be adopted for the analysis of $\bar{p}$-A scattering. Semiclassical approaches like one-turning point and three-turning point WKB approximation are found to be quite successful in HIS. It has also been suggested that, for strongly absorbed particles, the elastic and inelastic scattering data can be analysed using a technique known as closed formalism or parametric S matrix approach. In this approach one parametrises the nuclear S matrix in terms of several parameters appropriate to reproduce the scattering data and the associated physical features. Two commonly used parametrisations of S matrix are the Ericson and McIntyre parametrisations. In Chapter 3, we have described antiproton-nucleus collision using semiclassical and closed formalism techniques, thereby demonstrating that phenomenological and semiphenomenological theoretical approaches which are useful in heavy ion scattering can also be applied in the case of antiproton-nucleus scattering.

Another interesting feature of $\bar{p}$-A scattering that we have studied in Chapter 4 pertains to the relative sensitivity of the optical potential in different regions of the interaction volume. Using the technique of region-wise absorption it is possible to study the absorption of the incident flux in different shells around the scattering centre. In view of the similarity between $\bar{p}$-A and HIS, it is interesting to examine the interaction regions which contribute maximum to the reaction cross section in the $\bar{p}$-A scattering. This, and some related aspects are discussed in Chapter 4.

The heavy ion scattering has been found to be a very powerful tool in the study of nucleus during the last two decades. Many of the important reaction processes which have been studied are elastic and inelastic scatterings, fusion cross section, nuclear-molecular resonances, deep inelastic scattering etc. In Chapter 5, we have described the heavy ion fusion cross section results obtained using the recently proposed effective fusion barrier transmission model. This model is formulated within the framework of nuclear optical model and transmission across the effective barrier and is complimentary to the direct reaction model of fusion. The model is very successful in interpreting the fusion cross section over a wide range of energies below and above the Coulomb barrier. This approach also brings out the role of absorption and transmission across the barrier, in heavy ion fusion. Thus, the thesis incorporates several aspects of nuclear scattering which are of current and general interest within the broad framework of nuclear optical model.

THEORETICAL INVESTIGATIONS IN NUCLEAR OPTICAL MODEL WITH SPECIAL REFERENCE TO ANTIPROTON-NUCLEUS AND NUCLEUS-NUCLEUS SCATTERINGS

BASABADUTTA DEY
DEPARTMENT OF PHYSICS
SCHOOL OF PHYSICAL SCIENCES

A THESIS
SUBMITTED
IN
FULFILMENT OF THE REQUIREMENT FOR THE DEGREE OF

DOCTOR OF PHILOSOPHY

To

THE NORTH-EASTERN HILL UNIVERSITY
SHILLONG - 793 001
INDIA

JULY, 1991

in memory of
my
grandfather

Phone :
Grams : NEHU

North - Eastern Hill University
Bijni Complex
Bhagyakul, Shillong - 793003 (Meghalaya)

Department of.. Physics

CERTIFICATE

This is to certify that the thesis entitled **Theoretical Investigations in Nuclear Optical Model with Special Reference to Antiproton-Nucleus and Nucleus-Nucleus Scatterings**, submitted by **Miss. Basabadutta Dey** for the fulfillment of the degree of Doctor of Philosophy of the North-Eastern Hill University, Shillong, embodies the record of an original investigation carried out by her under my supervision. She has been duly registered, and the thesis submitted is worthy of being considered for the award of the Ph.D degree.

This work has not been submitted for any other degree to any other University or Institution.

Date: 12-7-1991
Place: Shillong

Dr. C. S. Shastry
Supervisor

Phone :
Grams : NEHU

North - Eastern Hill University
Bijni Complex
Bhagyakul, Shillong - 793003 (Meghalaya)

Department of.. Physics ...

Pre-Ph.D Course Grade Certificate

This is to certify that Miss Basabadutta Dey secured the grades mentioned below in the following Pre-Ph.D. courses.

COURSES	GRADES
1. Many Body Theory	A
2. Solid State Physics	A
3. Statistical Method	A
4. French Language	A

Prabodh Shukla
12/7/91

Dr. P. Shukla
Professor & Head

Professor and Head
Department of Physics
North-Eastern Hill University
Shillong-793003

ACKNOWLEDGEMENT

I take this opportunity to express my deepest sense of gratitude to my thesis supervisor Prof. C.S.Shastry, Department of Physics, N.E.H.U, Shillong for introducing me to this work. I am immensley grateful to him for his inspiring guidance, keen interest and encouragement throughout the period of my research. I owe my debt of gratitude to Dr. Raghuvir Singh, Physics Department, N.E.H.U, for his guidance and encouragement right from the years of my Post-graduation.

Parts of the computations contained in this thesis were carried out at Saha Institute of Nuclear Physics, Calcutta. I sincerely thank Dr.T.K.Roy of S.I.N.P, Calcutta, for all his help and collaboration.

It would have been difficult to complete my thesis and bring it to its present form without the help of my friends and colleagues - Susan, Sahu, Rao, Srinivas, Jayanta, Joe and Sudarshan, who were always ready to help me through valuable discussions and other odd jobs whenever required. To them I convey my deepest appreciation , specially to Susan, Jayanta, Joe and Sudarshan, who helped me immensely during the last, but most crucial stage of my work. Encouragement and moral support from all my friends, whose names have not been mentioned here, are humbly acknowledged.

Last but not the least, I am deeply indebted to all my family members for their cheerful cooperation and endless encouragement throughout this period.

I thank the Council of Scientific and Industrial Research, New Delhi, for financial assistance in the form of a Research Fellowship (Individual) during the years 1985-1990.

Basabadutta Dey

Date: 12-07-'91 **Basabadutta Dey**

Shillong

LIST OF PUBLICATIONS

1. Semiclassical approach to antiproton-nucleus scattering : B.Dey, C.S.Shastry and T.K.Roy, Pramāna-J.Phys. **31** (1988) 173

2. Region-wise absorption, interaction time and annihilation cross section in antiproton-nucleus collision : B.Dey and C.S.Shastry, Nuovo. Cim. **103A** (1990) 1199

3. Closed formalism approach to antiproton-nucleus scattering : B.Dey and C.S.Shastry, Nuovo. Cim. **104A** (1991) 139.

4. Interesting features of relativistic and non-relativistic quantal bound states in one, two, and three dimensions: B.Sahu, M.Z.Rahman Khan, C.S.Shastry, B.Dey and S.C.Phatak, Am. J. Physics. **57** (1989) 886 (not included in the thesis).

CONTENTS

PAGE NO.

CHAPTER 1

CHAPTER 2

REVIEW OF SOME ASPECTS OF ANTIPROTON-NUCLEUS COLLISION

CHAPTER 3

SEMICLASSICAL AND CLOSED FORMALISM APPROACHES TO ANTIPROTON-NUCLEUS SCATTERING

CHAPTER 4

REGION-WISE ABSORPTION, INTERACTION TIME AND ANNIHILATION CROSS SECTION IN ANTIPROTON-NUCLEUS COLLISION

CHAPTER 5

FUSION CROSS SECTION OF HEAVY ION SYSTEM USING EFFECTIVE FUSION BARRIER TRANSMISSION MODEL

CHAPTER 1

INTRODUCTION

The optical model for nuclear scattering [Ho 71, Ma 70] is very important to analyse the elastic and reaction cross sections in the nucleon-nucleus and nucleus-nucleus scattering. In this approach, the nucleon-nucleus and nucleus-nucleus system can be treated as a two body problem governed by complex effective interaction. This effective interaction is known as the optical potential. The availability of many reaction channels in addition to elastic channel in the nuclear scattering leads to the complex effective interaction in the nucleon-nucleus or the nucleus-nucleus scattering. The imaginary part of the complex potential leads to the absorption of the incident flux from the incident channel to various possible reaction channels leading to the total reaction cross section. Apart from describing the scattering data, optical model is useful in studying the properties of nuclear matter, density distribution and effective nucleon-nucleon interaction in the nuclear medium.

Since the discovery of atomic nucleus, it has been studied by collision experiments using various probes such as electrons, protons, α-particles, light ions, etc. Recently an additional probe namely, the antiproton has become available to study the nucleus. Antiproton ($\bar{p}$) which is the antiparticle of proton was discovered in 1955 . The availability of $\bar{p}$ source [Ga 84] at CERN, Geneva and Fermilab, etc. provides an experimental facility to carry out a variety of research using $\bar{p}$ as probes. In particular, it was realised that low energy antiproton can provide an interesting probe to study atomic nucleus and this gave rise to the LEAR (low energy antiproton ring) facility at CERN which has generated some interesting data [Ga 84, Ga 84a] on antiproton-nucleus ($\bar{p}$-A) collisions.

We now briefly summarise some areas of physics which benefit from the research carried out using $\bar{p}$ as probe, the most important area being Particle Physics. In particular, low energy antiproton machines can be useful in the study of weak symmetry breakdown, the origin of CP violation, etc. [Pi 86]. It can also be useful in the study of quark structure of matter, because $\bar{p}$-p offers appropriate initial states to couple directly to the rich spectroscopy of heavy quark systems. It has been visualised that very low energy antiprotons can be used in condensed matter studies, gravitation, etc. Atomic type bound states of antiproton with nucleus has generated antiprotonic atom physics research [Ba 87, Po 88, Th 85]. Antiproton-nucleus collisions, apart from giving an extra knowledge of the nuclear matter, has the potential to lead to a proper understanding of quark-gluon plasma [Mc 86, Ra 80, Ra 88, Ra 89]. Further the availability of polarised antiprotons can provide a useful tool for the study of spin dependent of interactions.

We have studied several aspects of low energy $\bar{p}$-nucleus collisions based on some of the experimental results which have become available. In Chapter 2, we have given a brief review of various aspects of low energy $\bar{p}$-nucleus collision which forms the background for our work.

Experimental results and theoretical analyses [Da 84, Ja 86, Ku 85, Li 85] show that antiproton-nucleus scattering has several similarities with heavy ion scattering (HIS). The angular distribution of $\bar{p}$-A systems shows a diffraction pattern which is similar to the Fraunhofer diffraction occuring in several cases of HIS. This is in contrast with the corresponding case of proton-nucleus scattering at the same energy. Moreover, both (HIS as well as $\bar{p}$-A) the scattering processes are surface dominant. These similarities indicate that some of the techniques developed for the analysis of HIS can also be adopted for the analysis of $\bar{p}$-A scattering.

Semiclassical approaches like one-turning point and three-turning point WKB approximation are found to be quite successful in HIS. Apart from some other well known techniques like optical model calculation and distorted wave Born approximation, another technique, developed mainly by Frahn [Fr 75, Fr 76] is used in the case of HIS. It has been suggested that, for strongly absorbed particles, the elastic and inelastic scattering data can be analysed using this technique which is known as closed formalism or parametric S matrix approach. In this approach one parametrises the nuclear S matrix in terms of several parameters appropriate to reproduce the scattering data and the associated physical features. Two commonly used parametrisations of S matrix are the Ericson and McIntyre parametrisations [Fr 78, Ma 78, Mc 60]. In Chapter 3, we have described antiproton-nucleus collision using semiclassical and closed formalism techniques, thereby demonstrating that phenomenological and semiphenomenological theoretical approaches which are useful in heavy ion scattering can also be applied in the case of antiproton-nucleus scattering.

Another interesting feature of $\bar{p}$-A scattering that we have studied in Chapter 4 pertains to the relative sensitivity of the optical potential in different regions of the interaction volume. It is well known that, in most of the HIS, optical potential is sensitive only to the surface region. To investigate the relative importance of different regions Shastry and Gambhir [Sh 83] have formulated a procedure to calculate the absorption of the incident flux in different shells around the scattering centre. Using this procedure, they have demonstrated that, in heavy ion scattering, the absorption cross section generated by both the fully absorbed and partially absorbed partial waves are confined to the surface region even when volume absorptive optical potential is used. In their work it is also demonstrated [Sh 84] as to how the inner regions of the potential become sensitive in the case of light ion-nucleus scattering and nucleon-nucleus scattering. In view of the similarity between $\bar{p}$-A and HIS, it is interesting to examine the interaction regions which contribute maximum to the reaction cross section in the $\bar{p}$-A scattering. This, and some related aspects are discussed in Chapter 4.

The heavy ion scattering has been found to be a very powerful tool in the study of nucleus during the last two decades. Many of the important reaction processes which have been studied are elastic and inelastic scatterings, fusion cross section, nuclear-molecular resonances, deep inelastic scattering etc. In

Chapter 5, we have described the heavy ion fusion cross section results obtained using the effective fusion barrier transmission model [Sa 89]. This model is formulated within the framework of nuclear optical model and transmission across the effective barrier. This model correlates the relationship between the direct reaction model [Ud 84, Ud 85] and barrier penetration model [Bi 83, Hi 53, Va 81] of fusion and is very successful in interpreting the fusion cross section over a wide range of energies below and above the Coulomb barrier. This approach also brings out the role of absorption and transmission across the barrier, in heavy ion fusion. Thus, the thesis incorporates several aspects of nuclear scattering which are of current and general interest within the broad framework of nuclear optical model.

Reference

[Ba 87] Batty. C.J, Phys.Lett. 189B(1987) 393

[Bi 83] Birkelund. J.R and Huizenga. J.R, Ann.Rev.Nucl. Part.Sc. 33(1983) 265

[Da 84] Dalkarov. O.D and Karmanov. V.A, Phys.Lett. 147B(1984) 1

[Fr 75] Frahn. W.E, *Heavy ion high spin states and nuclear structure* ,Vol I (International Atomic Energy Agency,1975) p.157

[Fr 76] Frahn. W.E, Nucl.Phys. A272(1976) 413

[Fr 78] Frahn. W.E and Rehm. K.E, Phys.Reports 37(1978) 1

[Ga 84] Garreta. D et al., Phys. Lett. 135B(1984) 266; ibid 139B(1984) 464; CERN Courier 23(1983) 416

[Ga 84a] Garreta. D et al., Phys. Lett. 149B(1984) 64; ibid 151B(1985) 473

[Hi 53] Hill. D.L and Wheeler. J.A, Phys.Rev. 89(1953) 1102

[Ho 71] Hodgson. P.E, *Nuclear reactions and nuclear structure* (Oxford University Press, 1971)

[Ja 86] Janouin. S et al., Nucl.Phys. A451(1986) 541

[Ku 85] Kubo. K.-I, Toki. H and Igarashi. M, Nucl.Phys. A435(1985) 708

[Li 85] Lichtenstadt. J et al., Phys.Rev. C32(1985) 1096

[Ma 70] Marmier. P and Sheldon. E, *Physics of nuclei and particles* , Vol II (Academic Press, 1970)

[Ma 78] Marty. C, *An analysis of heavy ion scattering amplitudes*, Lectures given at SUNY, Stoney Brook, USA (preprint, 1978)

[Mc 60] McIntyre. J.A, Wong. K.H and Becker. L.C, Phys.Rev. 117 (1960) 1337

[Mc 86] Mclerran. L. D, Rev. Mod. Phys. 58(1986) 102

[Pi 86] Pinsky. Lawrence S, *Eighth European symposium on nucleon-antinucleon interactions* Ed. by S.Charalambous, C.Papastefanou and P.Pavlopoulos (1986) p.315

[Po 88] Poth. H, Nucl.Phys. A478(1988) 655c

[Ra 80] Rafelski. J, Phys.Lett. 91B(1980) 281

[Ra 88] Rafelski. J, Phys.Lett. 207B(1988) 371

[Ra 89] Raha. S and Sinha. B, Phys.Lett. 218B(1989) 413

[Sa 89] Sahu. B and Shastry. C.S, J. Phys.G : 15(1989) L149

[Sh 83] Shastry. C.S and Gambhir. Y.K, Phys.Rev. C28(1983) 1109

[Sh 84] Shastry. C.S and Gambhir. Y.K, Pramāna-J.Phys. 23 (1984) 175

[Th 85] Thaler. J, J. Phys. G : 11(1985) 689

[Ud 84] Udagawa. T, Kim. B.T and Tamura. T, Phys.Rev. C29(1984) 1922

[Ud 85] Udagawa. T, Kim. B.T and Tamura. T, Phys.Rev. C32(1985) 124

[Va 81] Vaz. L.C, Alexander. J.M and Satchler. G.R, Phys.Reports 69(1981) 373

CHAPTER 2

REVIEW OF SOME ASPECTS OF ANTIPROTON-NUCLEUS COLLISION

2.1 General features of antiproton-nucleon reaction

2.1.1 Introduction

The antiproton-nucleon interaction can lead to various reaction channels like elastic, inelastic and charge exchange scattering and to annihilation. Among them annihilation is most dominant and is not associated with the corresponding nucleon-nucleon interaction. We discuss briefly $\bar{p}$- annihilation involving one nucleon and also the possibility of annihilations involving several nucleons. The other relevant topics which follow annihilation are [Ca 83] : (1) regions of annihilation, (2) transfer or dissipation of the energy released, (3) pion multiplicity, (4) the time evolution of the system, etc. All these aspects are discussed in great detail by Cahay [Ca 83]. The deposit of energy of about 2 GeV due to $\bar{p}$ annihilation inside the nucleus opens up new and interesting prospects as first mentioned by Rafelski [Ra 80]. Energy of this magnitude can excite the nucleus to high temperature or can result in nuclear explosion. It may also create large bags from coalescence of nucleons.

For the last few years annihilation of $\bar{p}$ in light nuclei [Ba 87, Na 87, Ph 87] as well as in heavy nuclei [Ca 83, Ra 80] has been studied in great detail. There is also a considerable discussion about the possibility of annihilation involving more than one nucleon [Cu 84, He 87, Ka 84, Ra 84]. Such a possibility i.e., occurence of annihilation involving more than one nucleon has been suggested long time back [Po 56]. The $\bar{p}$-nucleus annihilation may give rise to the production of strange particles. Strange particles produced in hot matter can carry information about the dense phase of the annihilation, as particles having strangeness are mostly produced in hot and dense zone. The abundance of strange particles can be considered as an important signal [Ko 87] in the search of quark matter present in the hot zone.

2.1.2 $\bar{p}$-p cross sections

Different $\bar{p}$-p cross sections which were parametrised [Cu 89] in terms of p, the incident antiproton laboratory momentum, are given below:

(1) Annihilation cross section:

$$\sigma_{ANN} = \frac{24}{p^{1.1}} + \frac{38}{p^{0.5}} \tag{2.1.1}$$

(2) Charge exchange cross section:
$(\bar{p}\ p \longrightarrow \bar{n}\ n)$

$$\begin{aligned} \sigma_{CEX} &= 10.9\ \frac{p - 0.1}{p^{1.6}}, \quad p < 0.5 \\ &= 7.1\ p^{-0.9}, \quad p > 0.5 \end{aligned} \tag{2.1.2}$$

(3) Elastic cross section:

$$\sigma_{EL} = 42.3\ p^{-0.54} + 4.3\ \exp\left[-\left(p - 1.5\right)^2 \right] \tag{2.1.3}$$

(4) Non strange production cross section:

(with a nucleon and an antinucleon in the final state)

$$\sigma_{PROD} = 30 \frac{(p-0.793)^{3/2}}{2 + (p-0.793)^{3/2}} \qquad (2.1.4)$$

(5) Strange production cross section:

(with atleast one hyperon (antihyperon) in the final state)

$$\sigma_{Y} = 3 \frac{(p - 1.435)}{10 + (p - 1.435)} . \qquad (2.1.5)$$

Here cross sections are expressed in mb and momentum p in GeV/c. Variations of the cross sections as a function of p are shown in Fig. 2.1.1. A glance at the figure indicates that various reaction channels open at different $\bar{p}$ momentum. At very low momentum annihilation channel ($\bar{N}\,N \longrightarrow$ mesons) is the most dominating one. In such cases, elastic and total cross sections can be described by the strong absorption model or by a boundary condition model with R ≈ 1 fm [De 78]. At about 0.1 GeV/c, the charge exchange ($\bar{p}\,p \longrightarrow \bar{n}\,n$) reaction starts. The inelastic channels with the production of a nucleon and an antinucleon in the final state ($\bar{N}\,N \longrightarrow \bar{N}\,N$ + mesons) starts contributing at energies ≈ 0.79 GeV/c whereas the momentum required for the production of strange particles in the inelastic channel is ≈ 1.43 GeV/c. It is also to be noted that, in the case of $\bar{p}$-p scattering, the total cross section σ_{TOT} is much larger than in the case of

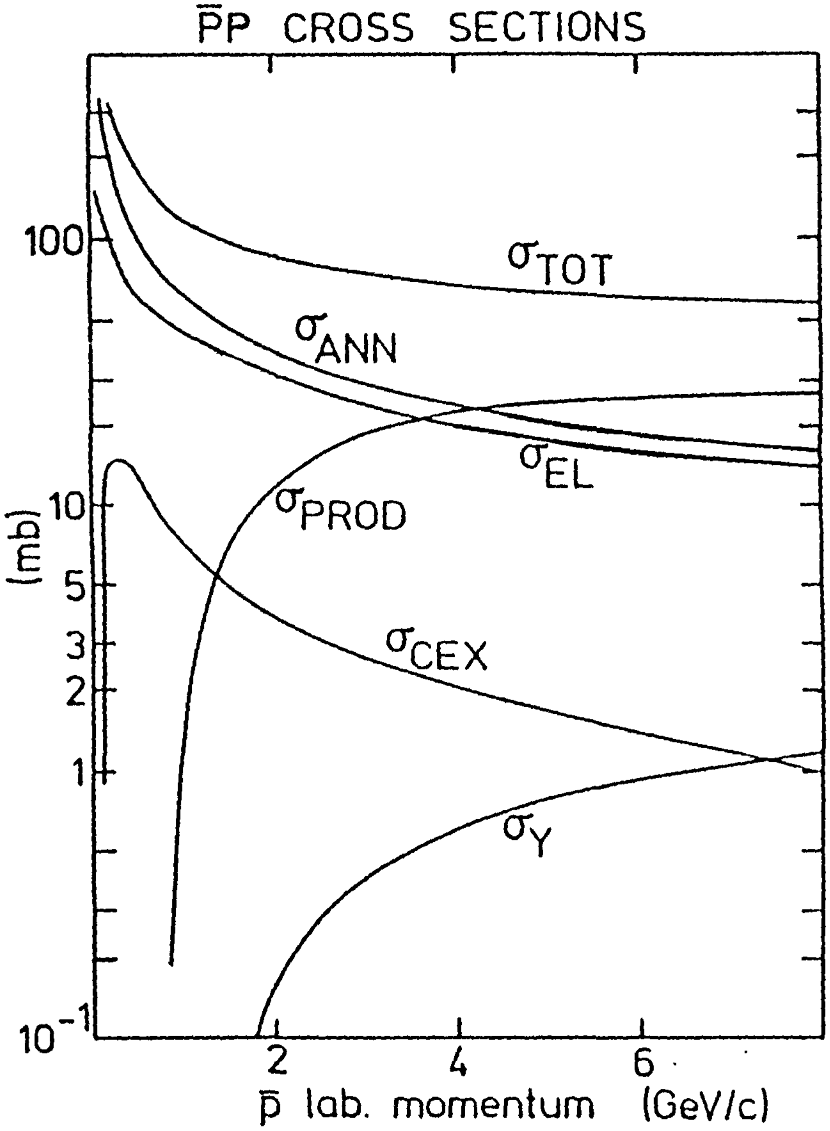

Fig.2.1.1 Dependence of the different $\bar{p}$ p cross sections on the antiproton laboratory momentum [Cu 89].

p-p scattering [Ya 87]. This is mainly due to the annihilation process involved in $\bar{p}$-p case. From Fig. 2.1.1 it is seen that σ_{ANN} is ≈ 60% of σ_{TOT} whereas σ_{EL} is ≈ 30% .

One can formulate the $\bar{N}$ N collision problem at low momentum (≤ 1 GeV/c) within the framework of the potential model [Br 68, Ya 87]. The nucleon-antinucleon potential has two parts. The first part is obtained from the corresponding nucleon-nucleon potential V_{NN} using the G - parity transformation. However, this will not be adequate to describe $\bar{N}$ N interaction because of the presence of annihilation channels. The other part accounts for annihilation, which is not present in NN collision. Phenomenologically one can represent the potentials corresponding to the annihilation channel by the complex potential V_{ann}. As a result the nucleon - antinucleon potential ($V_{\bar{N}N}$) can be indicated as follows [Ya 87]:

$$\begin{aligned} V_{\bar{N}N} = V_c + V_\sigma\, \bar{\sigma}_{\bar{N}}\cdot\bar{\sigma}_N + V_\tau\, \bar{\tau}_{\bar{N}}\cdot\bar{\tau}_N + V_{\sigma\tau}\, \bar{\sigma}_{\bar{N}}\cdot\bar{\sigma}_N\, \bar{\tau}_{\bar{N}}\cdot\bar{\tau}_N \\ +\text{(tensor, spin-orbit, and other terms)} \\ + V_{ann} \qquad\qquad (2.1.6) \end{aligned}$$

The first two lines which include the central, spin dependent, isospin dependent, tensor, spin-orbit and other terms, represent the interactions, which are deduced from V_{NN} using the G-parity transformation.

There are two widely used $\bar{N}N$ potentials in the literature. The first one due to Dover and Richard [Do 80, Do 82] uses a complex annihilation potential V_{ann}. The second one known as Paris potential [Co 82] uses an imaginary, but strongly spin dependent annihilation potential . $V_{\bar{N}N}$ contains interesting physics and can be expected to be deep to account for the $\bar{N}N$ bound state and resonances [Ya 87]. The imaginary part of $V_{\bar{N}N}$ can be expected to make resonant state widths large.

2.1.3 Annihilation range

With the availability of LEAR facility elastic scattering, charge exchange, reaction and annihilation cross sections have been measured in the scattering of $\bar{p}$-p interaction in the momentum range between 180 and 600 MeV/c [Br 85, Br 86, Br 86a, Sh 88]. As it is clear from Fig.2.1.1 that in $\bar{p}$-p interaction, annihilation is the most dominant channel it is interesting to know at what distance annihilation takes place [Po 86, Sh 87]. It is expected that annihilation proceeds via quark rearrangement and consequently it can be determined by the short range potential whereas elastic scattering and charge exchange reactions are determined by the long range part of nuclear force such as one-pion-exchange. The ranges of these three interactions have been investigated [Sh 87, Sh 88] within the framework of a model having a long range one-pion-exchange potential and a short range complex Woods-Saxon potential. The results of the investigation show that antiproton-proton annihilation takes place at short distances of less than 2 fm while charge exchange reaction can extend upto 4 fm.

2.1.4 Models of $\bar{N}$-N annihilation

$\bar{N}$-N annihilation can be handled either by statistical model [Cu 84, Cu 89, Cu 89c] or by quark model [Ru 66]. The special features of $\bar{p}$-p annihilation at rest and low momentum can be interpreted well by using the simple statistical approach. Here, we have briefly summarised the important aspects of the statistical approach. In this model there are a number of parameters which are able to interpret the pion multiplicities [Ma 76, Mö 75, Or 73, Va 74, Va 80]. There is a free parameter which is related to the interaction volume. This model is suitable for low momentum annihilation and can be extended to intermediate energies by varying interaction volume with energy. The new version of the statistical model explains the $\bar{p}$-p experimental data upto about 10 GeV/c [Va 78, Va 80]. To account for the strange particle production in annihilation, the statistical model requires extra parameters [Cu 87]. The model describes fairly well the data for baryon number $B = 0$ annihilation and is generalised for $B > 0$ cases also. Although there exists experimental evidence [Bi 69, Oh 73] in support of the annihilation involving several nucleons the corresponding statistical picture, however, is not yet fully explored. Summarising, the statistical model is found to be quite successful in describing many properties of $\bar{p}N$ annihilation. One also expects that during the process of $\bar{N}N$ annihilation, overlapping of the interacting particles lead to the development of quark model. In Fig. 2.1.2 , we schematically represent the $\bar{N}N$ annihilation within the framework of quark picture [Cu 89]. The symbol $\substack{\longrightarrow \\ \longrightarrow \\ \longrightarrow}$ represents a nucleon and $\substack{\longrightarrow \\ \longleftarrow}$ represents a meson.

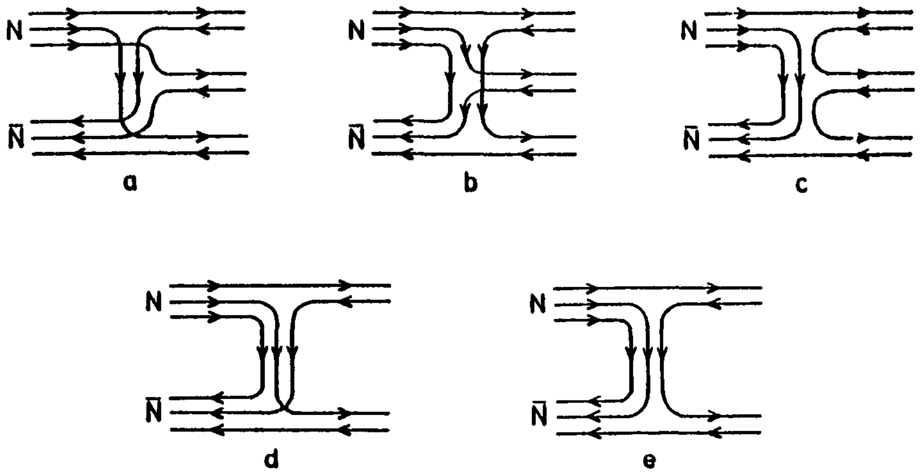

Fig.2.1.2 A schematic diagram illustrating $\bar{N}N$ annihilation in quark model : (a) rearrangement, (b) and (c) annihilation ; all three leading to three mesons, (d) rearrangement and (e) annihilation ; both leading to two mesons.

2.1.5 Interaction at rest

Slow antiprotons [Ba 86a, Cu 89, Re 88] captured in a Bohr orbit having high principal quantum number form antiprotonic atoms [Ba 87a, Po 88, Th 85] which deexcite by radiative transition (lasts for $\sim 10^{-10}$s in dense targets) or by Auger emission. The antiprotonic atom finally reaches a state where $\bar{p}$ overlaps with the nucleus which subsequently annihilates on the surface of the nucleus (lifetime of the captured state is $\approx 10^{-18}$s.) generating few pions. These pions cascade through the nucleus in the process of successive collision with nucleons of the nucleus. The residual nucleus is then left in an excited state and the nucleus dissipates this excitation energy either by evaporating few nucleons (in the case of light nuclei) or by fission (in the case of heavy nuclei). The $\bar{p}$-p annihilation at rest, follows the capture of an antiproton in a Bohr orbit around a proton. In this kind of annihilation about 5% of the events produce a $K\bar{K}$ pair, with two pions on the average [Ba 64, Ba 66]. Measurement of non-strange $\bar{p}$-p annihilation in liquid hydrogen produces a mean number 3.05 of charged pions and 1.96 ± 0.23 of neutral pions per annihilation [Gh 74]. The theoretical calculation of Montanet [Mo 75] gives the mean number of neutral pion to be ≈ 1.80. The production rates for some final states in $\bar{p}p$ and $\bar{p}n$ reaction at rest are given in details in reference [Cu 89]. The fraction of strange annihilation increases from $\approx$ 5% at rest to $\approx$ 10% at a few GeV/c.

2.1.6 Annihilation probability density

As antiproton is a strongly absorbed particle the probability density inside the nucleus decreases. The probability density distribution $P(r)$ represented by the solid curve (——) and the nuclear density $\rho(r)$ represented by the dashed curve (---) are shown as a function of $(r-R_0)$ in Fig.2.1.3 for various nuclei ranging from ^{16}O to ^{238}U [Cu 89, Ja 88]. Here, R_0 denotes the half density radius and r is the distance between the centre of the nucleus and the annihilation site. The annihilation probability density $P(r)$ for the annihilation of quantal state with the principal quantum number n and orbital quantum number $l = n-1$ is defined by the expression $P(r) = r^2\rho(r)|\psi_{n,n-1}(r)|^2$. The numerical results obtained by Jasselette et al. [Ja 88] (shown in Fig.2.1.3) indicate that, annihilation state is not precisely known in the case of heavy nuclei unlike that of light nuclei. In the former, several states may make a contribution. This figure also indicates that annihilation takes place on the surface of the nucleus where nuclear density is quite low. This result could be used to test the neutron sensitivity at the surface of the nucleus [Le 74]. The variation of annihilation probability density with r is of much relevance to the result described in Chapter 4 where we have discussed the contribution to the reaction cross section from different shells of the nuclei.

2.1.7 Annihilation Channel

In the study of $\bar{p}$- nucleus interaction, annihilation is an important factor which is to be taken into account. Two

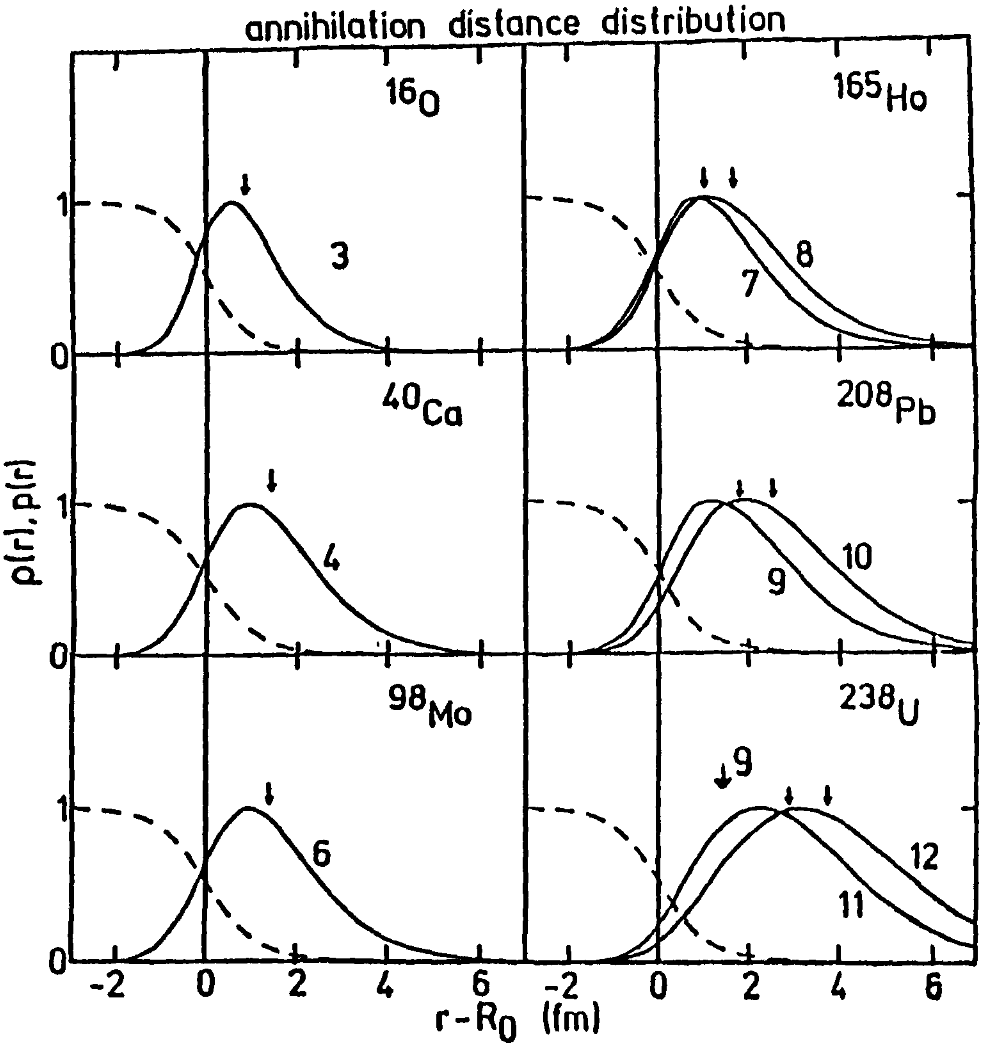

Fig.2.1.3 Distribution P(r) of the annihilation site in various targets for the Coulomb state (solid curve) specified by the principal quantum number n. Nuclear density $\rho(r)$ is shown by the dashed curve. The arrows indicate the mean location of annihilation. For ^{238}U, only the location for n = 9 state is indicated. All the curves are normalised to their maximum.

experiments were carried out at LEAR. In the first experiment (PS 179), negative pion multiplicity and the charged particle multiplicity [Ba 86a] were measured whereas in the second one (PS 186), the residual nuclei were studied [Mo 86, Mo 86a]. The mechanism of $\bar{p}$ annihilation on nuclei can be handled in the intranuclear cascade (INC) model [Ca 83, Cu 85, Cu 87, Ja 88]. The dynamics of the INC model [Cu 89a] can be described as follows:

(i) $\bar{p}$ annihilates on a single nucleon at the surface of the nucleus generating a few pions, with the same properties as those in free space

(ii) some of the primordial pions produced, penetrate into the nucleus, some of them leave the nucleus without interacting and some are scattered or absorbed

(iii)after the first ejection process has taken place the nucleus still contains some excitation energy which is dissipated either by evaporating few nucleons or by fission at a comparatively slower rate.

2.1.8 Energy transfer to the nucleus

During the process of annihilation the energy, of the order of 2 GeV or so, which is released, is not completely used to excite the nucleus [Ar 88]. Some of the pions escape through the nucleus without interaction while the rest (a fraction) of them are absorbed. This reduces the energy transfer to the nucleons substantially. The amount of energy transferred from pionic system to baryonic system is about 500 MeV for annihilation at rest and about 800 MeV for annihilation in flight [Cu 88] in the LEAR energy regime. The amount of energy transferred, E^* (MeV), to the nucleus (calculated within the framework of INC model) as a function of time 't' (fm/c) is displayed in Fig. 2.1.4 for different systems [Cu 87a]. The energy so acquired is dissipated in two time scales. Firstly, the energy is removed by the ejection of fast nucleons during which the exitation energy is concentrated close to the pion paths. This is shown schematically in Fig.2.1.5. After the fast ejection process is over, the remaining energy is distributed evenly in the nuclear volume and is dissipated by evaporation. For example, [Cu 88] in the case of ^{98}Mo, energy of about 150 MeV at rest (about 250 MeV for annihilation in flight) is acquired after the ejection of fast nucleons. Thus, ^{98}Mo can loose about 15 nucleons on the average but due to large fluctuations, it can even loose upto 30 nucleons. Here it is worth mentioning that some of the debated questions are : [Cu 89b] (i) What is the minimum energy required to trigger the process? (ii) Is the transition from evaporation to multifragmentation rapid ? etc. These problems have been studied in $\bar{p}$-nucleus and nucleus-nucleus collisions. It has been suggested that if the excitation energy is below some specific value, loss of nucleons is due to the evaporation process and if it is large the nucleus loses its cohesion and divides into many pieces of intermediate sizes. This is called multifragmentation process. The expected value of excitation energy is about 3 MeV per nucleon. Thus antiproton offers an excellent tool for multifragmentation as well as a vehicle for depositing large amount of energy without involving large momentum and angular momentum. A comparative study

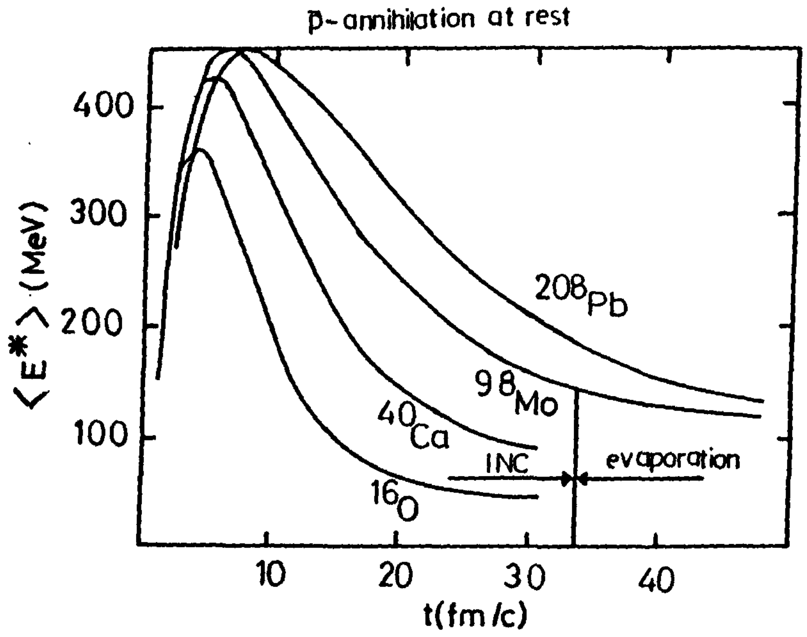

Fig.2.1.4 Variation of the target excitation energy with time, after annihilation of antiproton on a number of nuclei.

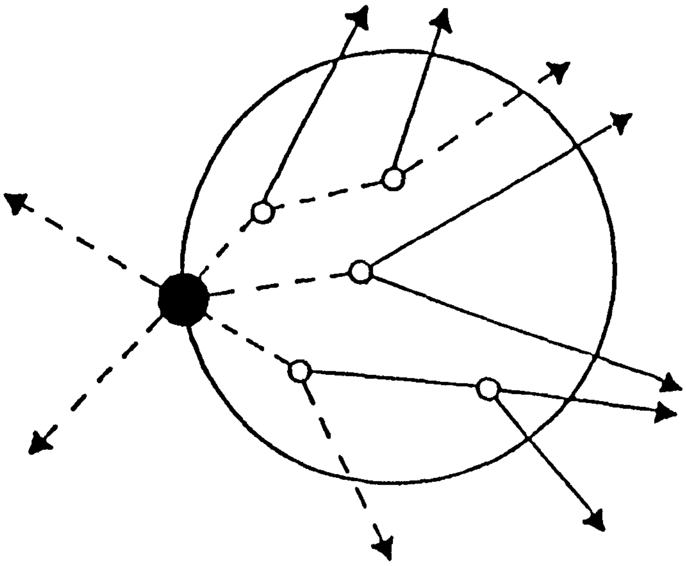

Fig.2.1.5 A schematic representation of the interaction between the annihilation pions (dotted lines) and the nucleus.

of multifragmentation, [Cu 89b] using $\bar{p}$ and heavy ion beams is given in Table 2.1.1.

2.1.9 Unusual annihilation

In the INC model, it has been assumed that $\bar{p}$ annihilation on nuclei is a point like phenomena. However, the process is a little more complicated. The annihilating system may last for some time before decaying into pions. During this time it travels through some distance inside the nucleus and encounters another nucleon. The frequency of this "unusual" event has been estimated to be ≈ 10-20% for annihilation in flight [Cu 89b]. An experiment for the measurement of strange particle production was carried out by Miyano et al. [Mi 84] at 4 GeV/c for $\bar{p}$-p annihilation on heavy nuclei like Tantalum (Ta). The production cross section for lambda (Λ) particles [Cu 89] in $\bar{p}$ - p reaction is about ≈ 0.53 mb at 4 GeV/c. Miyano et al. measured the cross section on Ta target and found an enhancement of the production cross section which is ≈ 193 mb at the same momentum. Dependence of the production cross section on the atomic number and the geometrical cross section of the nuclear target is indicated in reference [Mi 84]. A very simple estimate of lambda (Λ) production cross section on Ta given by Ko and Yuan [Ko 87] is about 60 times larger than the value for $\bar{p}$-p reaction. They [Ko 87] suggested that if the kinetic energy of the pions produced in $\bar{p}$-p annihilation is greater than 900 MeV, then the associated production ($\pi N \longrightarrow \Lambda K$) between the secondary pions and target nucleus leads to the production of lambda particles. The total

Table 2.1.1 Comparison between $\bar{p}$ and heavy ion beams for the study of multifragmentation [Cu 89b].

	$\bar{p}$	heavy ions
critical energy	$\sim$ 1 GeV	$\sim$ 200 MeV/A
momentum transfer	small	large
angular momentum transfer	small	large
definition of the fragmenting system	good	$\sim$ rather bad
mixing of various sources	no	$\sim$ yes

cross section for producing lambda paticles via the associated production is about 29 mb. There are other two step processes like (1) $\bar{p}N \longrightarrow \bar{K}X$, $\bar{K}N \longrightarrow \pi\Lambda$ and (2) $\bar{p}N \longrightarrow \Sigma X$, $\Sigma N \longrightarrow \Lambda N$, which contribute to the production of lambda particles. Combining all the contributions for the lambda production, the cross section is estimated to be ≈ 122 mb which is about 1.6 times smaller than the experimental value and needs more investigation. However, it is also shown in references [Cu 84, De 85] that the $\bar{p}$ annihilation on a cluster of nucleons in nuclei leads to an enhancement of production of strange particles. Derreth et al. [De 85] also showed that the strangeness production depends substantially on the baryon number density of the fire ball.

2.2 General features of antiproton-nucleus scattering

2.2.1 Introduction

During the last decade low and medium energy antiproton interaction with nuclei have been investigated experimentally at BNL [As 84], KEK [Na 84], LEAR [Ga 84]. Experimental data have been obtained for a number of nuclei ranging from ^{4}He to ^{208}Pb in the energy range from 20 - 200 MeV [As 84, Ba 85, Ga 84, Na 84]. The experimental data of antiproton-nucleus scattering is quite different from that of proton-nucleus scattering [Wi 72] at the same energies. In the case of antiproton the differential scattering cross section shows a sharp diffraction pattern [Ga 84] whereas that of proton scattering at the same energy decreases more smoothly. This is illustrated in Fig. 2.2.1. The effective

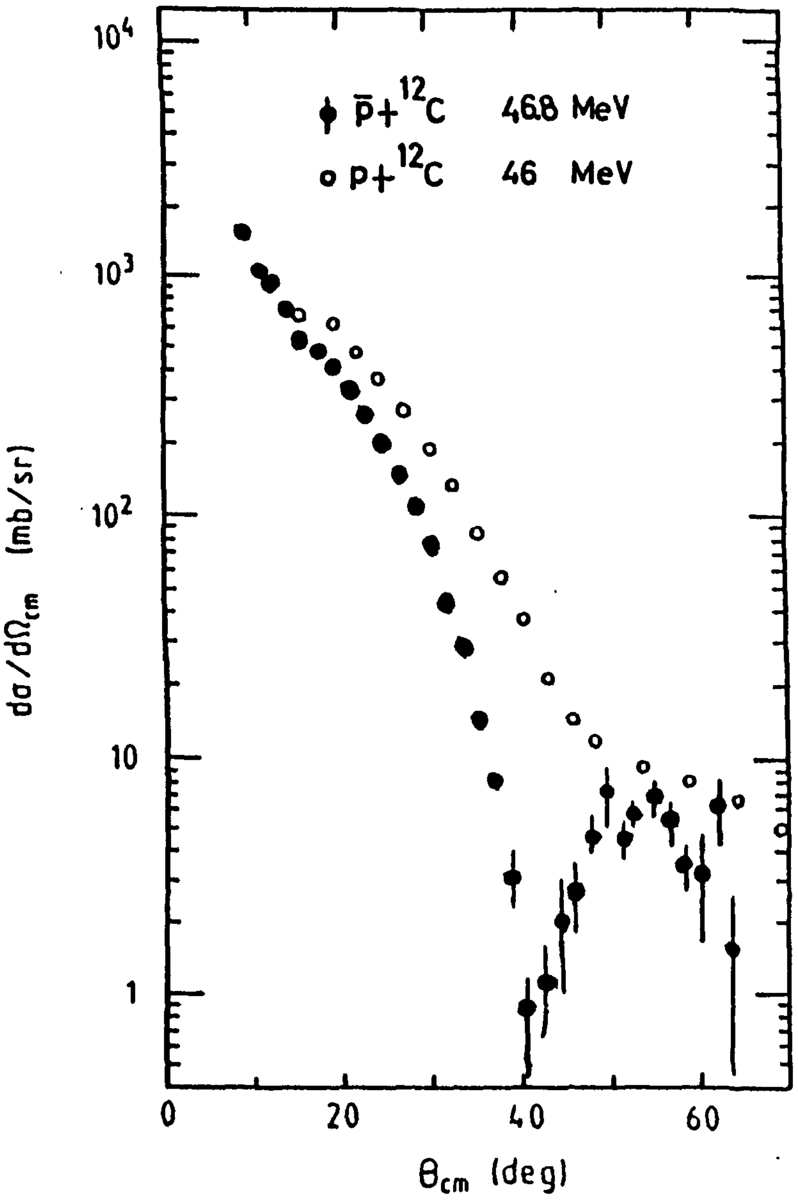

Fig.2.2.1 Differential cross sections of elastic scattering for $\bar{p} + {}^{12}C$ (solid circles) and $p + {}^{12}C$ (open circles).

nuclear radius in the case of antiproton scattering increases by a factor of about 1.5-2 in comparison with the ordinary nuclear radius [Da 85]. Antiproton-nucleus scattering data have been analysed using various techniques namely, (1) Black body diffraction model [Li 85, Za 87], (2) Distorted wave approximation [Am 85], (3) Optical model calculation [He 85, Ja 86, Ku 85], (4) Glauber model calculation [Da 84, Da 85, Da 88] and (5) Coupled channel calculation [In 86] etc. Some of the techniques used to analyse $\bar{p}$-nucleus scattering data are discussed here briefly. The angular distribution of elastic and inelastic scattering of antiproton from ^{12}C , $^{16,18}O$, ^{40}Ca and ^{208}Pb have been measured at about 47 and 180 MeV [Ga 84, Ga 84a]. The important findings of the data are [Ya 87]: (i) the real (V(r)) and the imaginary (W(r)) parts of the potential cannot be determined in the interior region of the nucleus, (ii) however, V(r) in the interior is likely to be attractive and shallow, (iii) near the radius of strong absorption (R) both can be determined and $|V(R)| \le (1/2)|W(R)|$, (iv) in the case of Woods-Saxon potential, the potential parameters approximately satisfy $V_0 \le 60$ MeV, $V_0 \le (1/2)W_0$ and $r_r \approx r_i$ and (v) both R and the reaction cross section decreases with the incident $\bar{p}$ energy indicating that at higher energies $\bar{p}$ can penetrate deep into the nucleus.

We have discussed in the previous section (i.e.,Sec.2.1) that at low incident energies, annihilation is an important process in $\bar{p}$-p interaction. As the antiproton approaches the nucleus, the absorption of $\bar{p}$ results in an oscillatory diffractive pattern. Thus, it is necessary to consider this aspect in all the theoretical models. This highly absorptive nature of the nucleus to the incoming $\bar{p}$ can be considered by assuming the nucleus to be a black sphere.

2.2.2 Black body diffraction model

When $\bar{p}$ impinges a nucleus the probability of the absorption of $\bar{p}$ is more as compared to any other probe. It has been shown that some of the characteristics of $\bar{p}$-nucleus scattering data can be explained in the light of black disc scattering [Li 85, Za 87]. Assuming that the scattering is caused by a black disc with a sharp edge of radius R, the differential scattering cross section in the centre-of-mass frame is given by

$$\sigma_{bd}(\theta) = |f_0(\theta)|^2 = (kR^2)^2 \left[\frac{J_1(x)}{x}\right]^2, \qquad (2.2.1)$$

where $x = 2kR \sin(\theta/2)$.

Here $f_0(\theta)$ is the scattering amplitude corresponding to the black disc scattering, k represents the incident $\bar{p}$ momentum and θ is the scattering angle. The fully absorptive black disc representation of the nucleus for the incident $\bar{p}$ is a rather drastic approximation [Ya 87]. Hence, the effect of the surface diffuseness on $f_0(\theta)$ was studied by some authors [Bl 60, In 65]. According to Inopin and Berezhvoy [In 65], the scattering amplitude can be expressed as

$$f(\theta) = f_0(\theta)\, F(\theta), \qquad (2.2.2)$$

where $F(\theta)$ is the diffuseness function. Assuming the shape of $F(\theta)$ to be Gaussian type ,i.e.,

$$F(\theta) = \exp\left[-\Delta^2 k^2 \sin^2(\theta/2)\right], \qquad (2.2.3)$$

where Δ is known as diffuseness or fuzziness parameter. Thus the scattering cross section can be written as

$$\sigma = |f(\theta)|^2 = |f_0(\theta)|^2 \; |F(\theta)|^2$$

$$= \sigma_{bd}(\theta) \; |F(\theta)|^2 \qquad (2.2.4)$$

which is a two-parameter formula. The best fitted curves (solid lines, ———) obtained [Ya 87] for different systems (viz, $\bar{p}$ + ^{12}C at E_{lab} = 47 and 180 MeV and $\bar{p}$ + ^{40}Ca at E_{lab} = 180 MeV) within the framework of black disc model with $\Delta \neq 0$ are displayed in Figs. 2.2.2(a)-(c). For comparison purpose the dashed curve (-----) corresponding to sharp black disc calculation ($\Delta = 0$) is also shown in Fig. 2.2.2(a). The results show that a diffuseness parameter $\Delta \neq 0$, is required for the best fit of the curve. The parameters of the black disc model are contained in Table 2.2.1. Thus,it is clear that $\Delta \approx 1.1$ fm gives quite good fit to the experimental data [Ga 84, Ga 85]. It reproduces the position of the valleys but not the slope of the angular distributions. From Table 2.2.1 it is seen that the radius parameter r_0 ($r_0 = R/A^{1/3}$) corresponding to R is about 1.5 fm at 180 MeV and about 1.7 fm at 47 MeV and Δ, the width of the diffuseness function is $\approx$ 1.1 fm at both energies. Thus $\Delta \neq 0$, indicates that $\bar{p}$ can penetrate into the nucleus. Though the interior of the nucleus is black but there is a grey surface in and beyond which many interesting physics can take place which should be investigated [Ya 87]. The value of r_0 indicates that the strong absorption radius extends well beyond the size of the target nuclei (which is $\sim 1.2A^{1/3}$ fm).

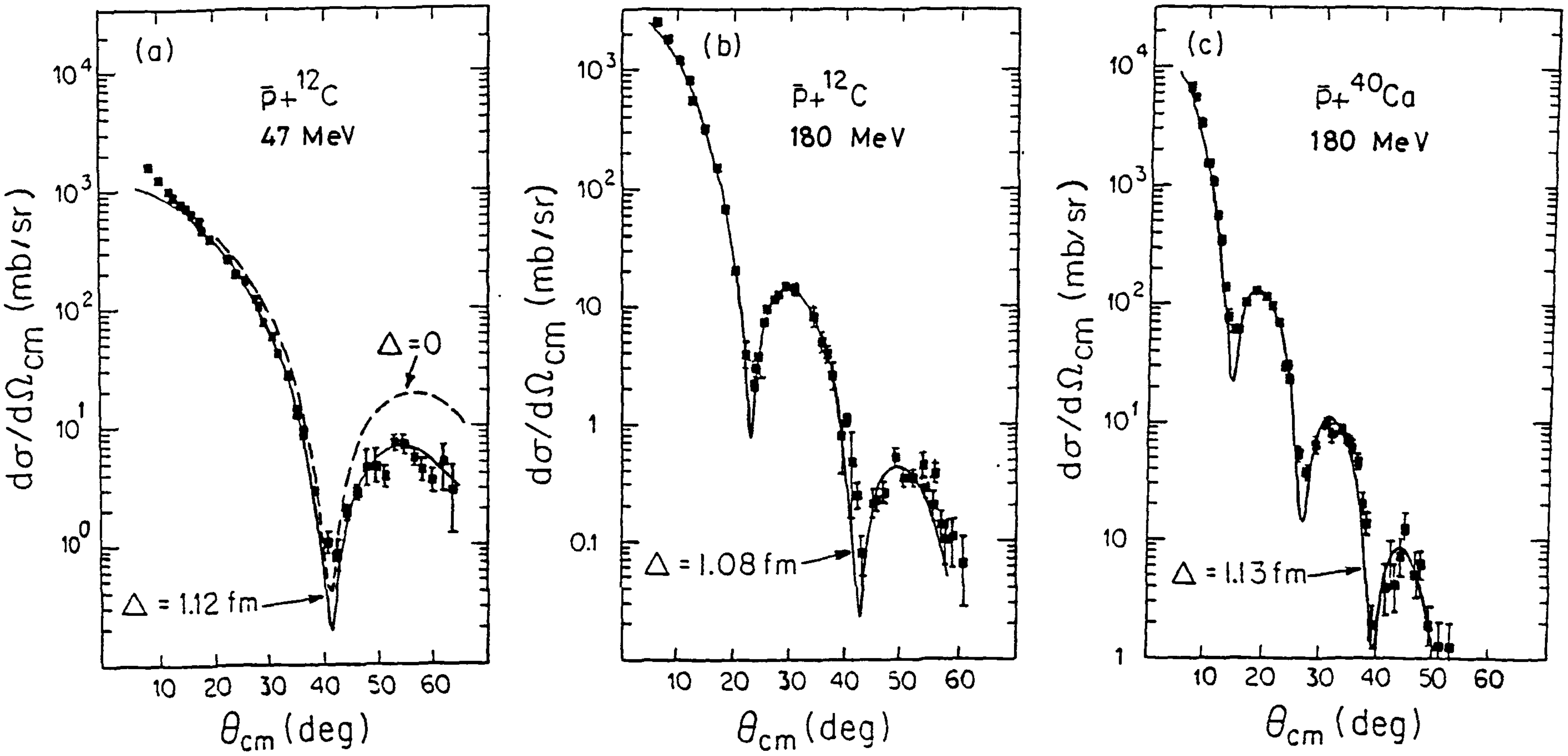

Fig.2.2.2(a)-(c) Angular distributions of $\bar{p}$ - nucleus elastic scattering. Solid curves represent black disc calculation with $\Delta \neq 0$ and the dashed curve in (a) represents black disc calculation with $\Delta = 0$.

Table 2.2.1 A brief summary of the black disc model parameters for different $\bar{p}$-A systems.

Target	E_{lab} (MeV)	R (fm)	r_0 (fm)	Δ (fm)
^{12}C	47	3.91	1.71	1.12
^{40}Ca	47	5.56	1.63	1.09
^{12}C	180	3.47	1.52	1.08
^{16}O	180	3.79	1.50	1.09
^{18}O	180	3.91	1.49	1.17
^{40}Ca	180	5.09	1.49	1.13

2.2.3 Distorted wave approximation

Distorted wave approximation method [Am 85] is found to be quite useful in analysing the direct reaction data of $\bar{p}$-A scattering. In this approach one uses the fact that, $\bar{p}$-A collision is a surface dominated phenomena and the incident wave gets attenuated on the surface. One of the advantages of this approach is that parameters or scales can be varied freely. In this approximation, an analytic form of the distorted wave function $\psi_{k_i}^{(+)}(\bar{r})$ is assumed and is represented by

$$\psi_{k_i}^{(+)}(\bar{r}) = N \exp\left[(i\alpha - \beta)\bar{k}_i.\bar{r}\right] \qquad (2.2.5)$$

with N, the value to yield unit magnitude at the nuclear surface. The parameters α and β correspond to the refraction and attenuation character of the incident wave. The integral form of the elastic scattering amplitude is given by [Di 83]

$$f(\theta) = -\frac{\mu}{2\pi\hbar^2}\int \exp\,(-i\bar{k}_f.\bar{r})\; U_{om}(r)\; \psi_{k_i}^{(+)}(\bar{r})d\bar{r}\;. \qquad (2.2.6)$$

Here Woods-Saxon form of the optical model ($U_{om}(r)$) potential is used. Using Eq.(2.2.5) the scattering amplitude in the analytic distorted wave approximation (ADWA) can be expressed as

$$f^{ADWA}(\theta) = \frac{2\mu N}{\hbar^2}\sum\left[4\pi\;(2l+1)\right]^{1/2} \; Y_{l0}\;(\Omega_{k_iT}) \times$$

$$\int_0^\infty j_l\;(Tr)\; j_l(i\beta k_i r)\; U_{om}(r)\; r^2\, dr, \qquad (2.2.7)$$

where $\bar{T} = \alpha\bar{k}_i - \bar{k}_f$

and $(\Omega_{k_iT}) = \dfrac{\pi-\theta}{2} - \sin^{-1}\left[\dfrac{(\alpha-1)k_i\;\sin((\pi-\theta)/2)}{T}\right].$

If the attenuation parameter ($\beta \ll 1$) and the scattering angles are small, all terms other than $l = 0$ can be neglected. With this approximation Eq. (2.2.7) becomes

$$f^{ADWA}(\theta) = \frac{2\mu N}{\hbar^2} \int_0^\infty j_0\,(Tr)\;U_{om}(r)\;r^2\,dr. \qquad (2.2.8)$$

The total scattering amplitude can be obtained by incorporating Coulomb scattering amplitude [Du 84] which is given by

$$f_C(\theta) = R_\eta\;f_{pt}(\theta)\;F(q) \qquad (2.2.9)$$

R_η being the relativistic correction factor and $f_{pt}(\theta)$ represents the Coulomb amplitude when the target and projectile are considered as point charges. F(q) is the form factor which takes care of the extended charge distribution of the nuclei. The expressions for the terms R_η, and $f_{pt}(\theta)$ are

$$R_\eta = 1 - (1/2)\pi\eta v^2 \sin(\theta/2) \exp(\,2i\sigma_0 + 2i\sigma_{-1/2}), \qquad (2.2.10)$$

where $\eta = (Z_1 Z_2 e^2 \mu)/\hbar^2 k$, $\exp(2i\sigma_l) = \dfrac{\Gamma(l + 1 + i\eta)}{\Gamma(l + 1 - i\eta)}$

and

$$f_{pt}(\theta) = (\eta/2k \sin^2(\theta/2)) \exp\left[-2i\eta\,\ln(\sin(\theta/2)) + 2i\sigma_0 + i\pi\right] \qquad (2.2.11)$$

Assuming the uniform charge distribution for the nucleus within a sphere of radius R_C, the form factor F(q) can be written as

$$F(q) = \frac{3}{(qR_C)^2}\,j_1(qR_C). \qquad (2.2.12)$$

Thus, the full scattering amplitude is

$$f(\theta) = f^{ADWA}(\theta) + f_C(\theta) \qquad (2.2.13)$$

Amos and Di Marzio [Am 85] used these equations to calculate the differential scattering cross sections for the elastic scattering of $\bar{p}$ from ^{12}C and ^{27}Al. A fit to the experimental data (for $\theta \leq 20^o$) obtained for different beam momenta are shown in Fig.2.2.3. This approximate method contains two more parameters in addition to the conventional optical model potential parameters. These (optical model potential parameters used in the calculation) are listed in Table 2.2.2 . The parameters α and β which give the best fit of the data for the above systems [Am 85] are summarised in Table 2.2.3. Their results are comparable to those obtained using optical model calculation and thus, it is suggested that in analysing the reaction data ADWA is more useful for $\bar{p}$ probe than any other intermediate energy probe [Di 83].

2.2.4 Glauber model for antiproton-nucleus scattering at low energy

It has been demonstrated that the experimental data [Ga 84, Ga 84a] for elastic and inelastic scattering of antiproton on ^{12}C, ^{40}Ca, ^{208}Pb targets at 46.8 and 180 MeV energies can be explained using Glauber theory of diffraction scattering [Gl 69]. Glauber model is assumed to be valid in the high energy (E ≥ 1GeV) hadron-nucleus scattering [Gl 59], but since the energy of the $\bar{p}$-A scattering is low, it was expected that Glauber model may not be applicable in such cases. For the validity of Glauber approximation [Da 85] two conditions must be satisfied. These are

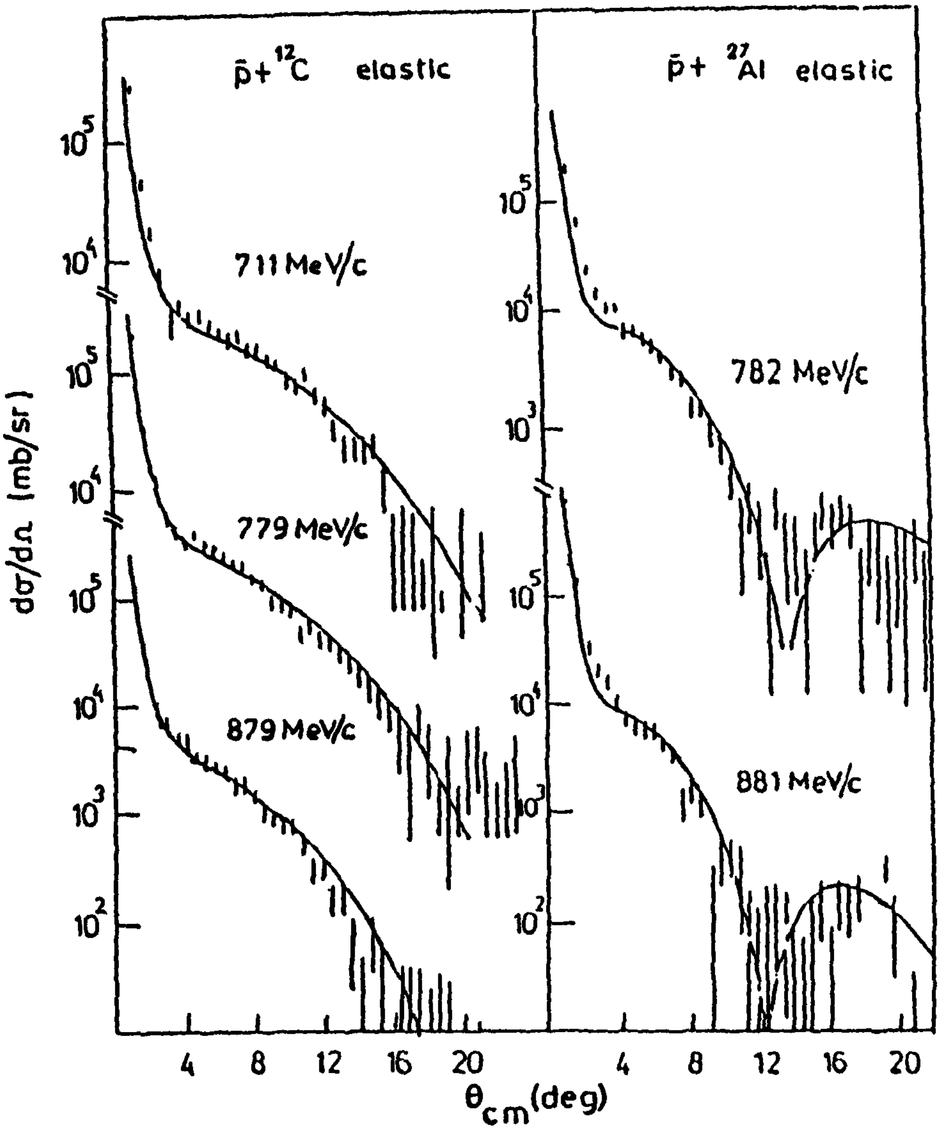

Fig.2.2.3 Differential cross section for $\bar{p}$ + ^{12}C and $\bar{p}$ + ^{27}Al systems at different beam momenta.

Table 2.2.2 Optical model potential parameters used in distorted wave approximation for $\bar{p}$-A systems [Am 85].

Target	V_0 (MeV)	$R_rA^{-1/3}$ (fm)	a_r (fm)	W_0 (MeV)	$R_iA^{-1/3}$ (fm)	a_i (fm)
^{12}C	20	1.3	0.52	95	1.1	0.52
^{27}Al	30	1.3	0.52	115	1.1	0.52

Table 2.2.3 Parameters of distorted wave approximation of $\bar{p}$-A system at various momenta [Am 85].

Beam momentum (MeV/c)	Target	α	β
711	^{12}C	1.22	0.005
779		1.19	0.0
879		1.175	-0.01
782	^{27}Al	1.202	-0.025
881		1.182	-0.035

(1) eikonal approximation and (2) adiabatic approximation. In the former, the deviation of the incident particle from the rectilinear path is small. Thus, it appears that eikonal approximation is valid for small angle collisions which is the case for scattering at high energies. In adiabatic approximation, one assumes that during the flight time of the particle inside the nucleus, the positions of the nucleons of the target nucleus remains fixed (i.e., frozenness of nucleons). This condition is also valid at high energy. However, in the case of antiproton at low energy the validity of eikonal approximation is confirmed by by the fact that, $\bar{p}N$ scattering amplitude has a strongly pronounced peak in the forward direction which shrinks with the decrease in energy [Da 84, Da 85]. For example, the slope of the elastic $\bar{p}$-p forward peak at 46.8 MeV is 35.6 $(GeV/c)^{-2}$ [Da 85] whereas p-p elastic cross section at the same energy is practically isotropic in nature [Ke 59]. Even at high energy the slope of the pp forward peak ≤ 6 $(GeV/c)^{-2}$. Such a narrow forward cone at small energy and its antishrinkage behaviour is favoured by the fact that even at low energy several partial waves [Sh 78] with nonzero orbital momenta contribute to $\bar{p}p$ scattering. Taking into account all the spin and isospin states the total number of partial waves ≥ 20. The interference of the partial waves causes the narrow forward peak in $\bar{p}N$ scattering amplitude [Da 77]. The existence of this forward peak at low energy could be one of the causes for the applicability of Glauber model. In the case of $\bar{p}$-A scattering, Glauber model is found to be valid even at low energy ($\sim$ 50 MeV) whereas this mechanism for proton scattering at the

same energy distinctly differs from the experimental data. The good agreement of the experimental results and theoretical calculations indicate that, contribution due to non adiabatic correction is small for low $\bar{p}$ energy.

For small momentum transfer $\bar{q}$, the elastic scattering amplitude ($F_{el}(q)$) for a nucleus of mass number A, can be written in the Glauber model as (without considering Coulomb effects) [Gl 67]

$$F_{el}(q) = ik \int_0^\infty \Gamma(b)\ J_0(qb)\ b\ db\ , \qquad (2.2.14)$$

where $J_0(qb)$ is the Bessel function, b the impact parameter and $\Gamma(b)$ is a function of input amplitude given by

$$\Gamma(b) = 1 - \exp\ (i\chi_N(b))\ , \qquad (2.2.15)$$

where $$\chi_N(b) = \frac{A}{2\pi k} \int e^{-i\bar{q}.\bar{b}} f_N(q)\ \phi(q)\ d^2q$$

is the nuclear phase. Here k is the incident beam momentum and $\phi(q)$ is the nuclear form factor and is parametrised for $4 \le A \le 16$ as [Ba 68]

$$\phi(q) = \left[1 - \frac{A-4}{6A} R^2q^2 \right] \exp\left(- R^2q^2/4\right) \qquad (2.2.16)$$

R being the nuclear radius. The input amplitude $\bar{p}N$ is of the form

$$f_N(q) = \frac{k\sigma(i + \varepsilon)}{4\pi} \exp\left(-Bq^2/2\right)\ . \qquad (2.2.17)$$

σ, ε and B are the parameters of the input amplitude which are different for $\bar{p}p$ and $\bar{p}n$ amplitude. In $\bar{p}$-A scattering, Coulomb interaction is rather important which is very sensitive even for light nuclei. Coulomb effects can be incorporated by including the

Coulomb phase alongwith the nuclear phase. With this (Coulomb effect) inclusion, the elastic scattering amplitude takes the form [Al 78, Gl 67]

$$\exp\left[i\chi_{scr}\right] F_{el}(q) = F_C(q) + ik \int_0^\infty J_0(qb) \exp\left[i\chi_0(b)\right]\left\{1 - \exp\left[i\left[\chi_N(b) + \chi_1(b)\right]\right]\right\} b\, db, \tag{2.2.18}$$

where

$$F_C(q) = -2\xi (k/q^2) \exp(i\varphi_C)$$

$$\varphi_C = -2\xi \ln(q/2k) + 2\eta$$

$$\eta = \arg \Gamma (1 + i\xi)$$

$$\chi_0(b) = 2\xi \ln kb$$

$$\chi_1(b) = 8\pi\xi \int_b^\infty \rho(r) \left\{ \ln\left[\frac{1 + (1 - b^2/r^2)^{1/2}}{b/r} \right] - \left[1 - b^2/r^2\right]^{1/2} \right\} r^2 dr$$

and the screening phase

$$\chi_{scr} = -2\xi \log\left[2kR_{scr}\right].$$

In the expression for $\chi_1(b)$, $\rho(r)$ is the nuclear charge density. $\xi = -\dfrac{Ze^2 m}{\hbar c k}$, Z is the nuclear charge. Assuming the charge density $\rho(r)$ (normalised to unity) to be equal to the nuclear density it can be parametrised ($4 \le A \le 16$) as

$$\rho(r) = \left[A\left[R\sqrt{\pi}\right]^3\right]^{-1} \left[4 + (2/3)(A - 4)(r/R)^2\right] \exp(-r^2/R^2). \tag{2.2.19}$$

Using Eq.(2.2.18) Dalkarov and Karmanov [Da 84, Da 85, Da 87] obtained reaction and differential elastic cross sections for $\bar{p}$ scattering for a number of nuclei within the framework of Glauber model. For illustration, a typical case namely, $\bar{p}$ + ^{12}C scattering at 46.8 MeV is chosen and is shown in Fig. 2.2.4 by the solid curve (———). For comparison purpose, the results of p + ^{12}C case at the same energy is also shown in the figure by dashed curve (------). Good agreement of the results with experimental data [Ga 84] for antiproton scattering confirms the validity of Glauber model. On the other hand the results of the Glauber model calculation for proton scattering deviates from the experimental data. It has been observed that, for the incoming antiproton the central region of the nucleus is a black sphere with a diffused surface. The effective radius R_{eff} of the black nucleus in the Glauber model is given by the formula

$$R^2_{eff} = 2\left|\int_0^\infty \Gamma(b) b \, db\right| \qquad (2.2.20)$$

For $\bar{p}$ + ^{12}C scattering it has been found that R_{eff} = 3.96 fm (r_0= 1.73 fm) and for p + ^{12}C case R_{eff} = 3.06 fm. The effective radius for antinucleon interaction is larger (by a factor of 1.5 for ^{12}C) than that in the electron scattering [Da 85]. In $\bar{p}$ + ^{12}C case, the results, assuming the nucleus to be a black sphere with sharp surface Δ = 0 and R_{eff} = 3.96 fm, are also shown by the dotted curve (......) in Fig. 2.2.4 . The data obtained by the black sphere model gives a good fit to the experimental data upto the first diffraction minimum and overestimates the data beyond this region which is due to the strong diffraction from the sharp surface.

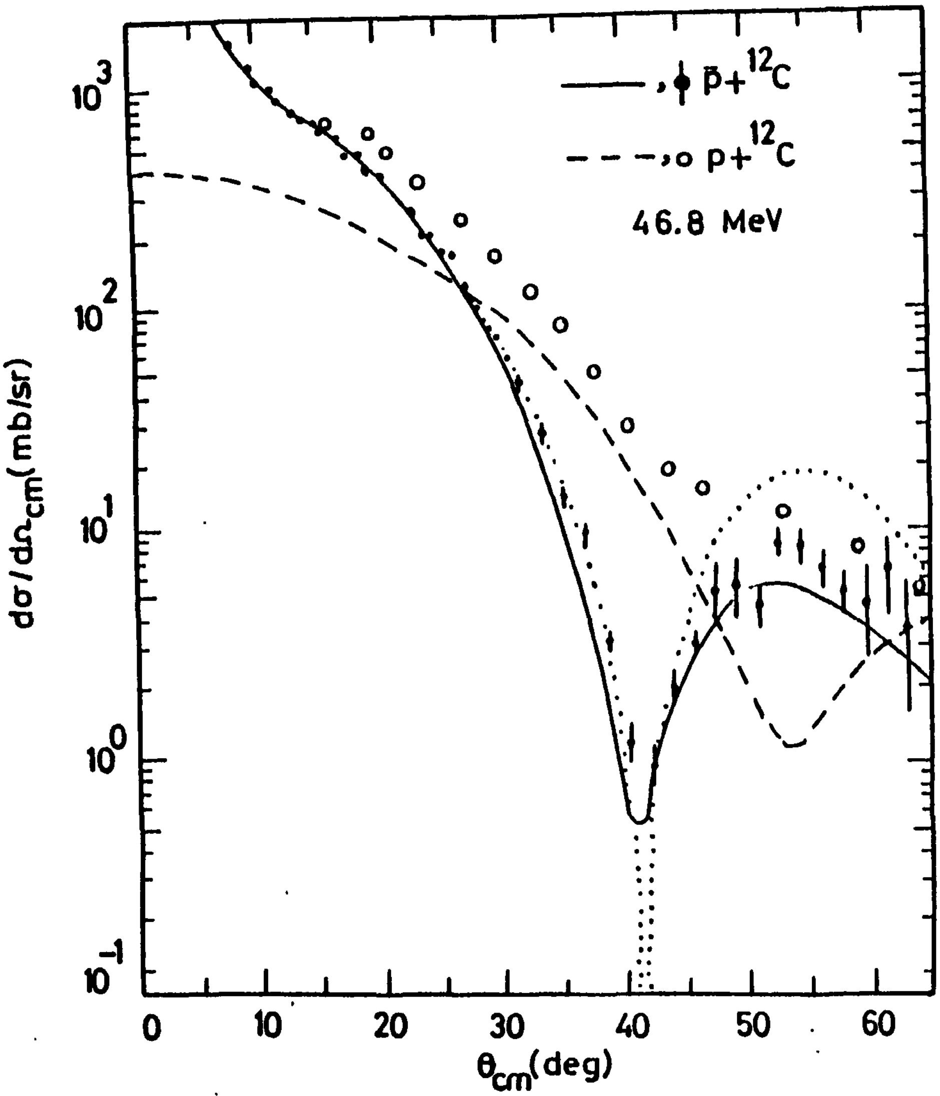

Fig.2.2.4 Differential cross sections of elastic scattering for $\bar{p}$ + ^{12}C and p $+^{12}C$ at 46.8 MeV obtained from Glauber model. Solid curve : $\bar{p}$ + ^{12}C; dashed curve : p + ^{12}C. Dotted curve is the sharp black disc result for $\bar{p}$ + ^{12}C.

The method is also used to determine the parameter ε, the real-to-imaginary ratio of $\bar{p}$N amplitude at diffractive minima. In the Glauber model, ε can be written in the form

$$\varepsilon = \mathrm{Re}\ f_N(0)/\mathrm{Im}\ f_N(0) \tag{2.2.21}$$

Hence, from Glauber model analysis of $\bar{p}$ – A scattering, one can get a check on the ratio, ε, determined in $\bar{N}$N scattering experiments. The optical potential (V(r)) for $\bar{p}$-A scattering can be obtained by using this model. Another important utility of Glauber model is that it can be employed successfully in the study of $\bar{p}$-A inelastic scattering. This has been carried out by Dalkarov and Karmanov [Da 85] and Mahalanabis [Ma 87].

2.2.5 Optical model potential

Experimental $\bar{p}$-A scattering data have been analysed in a number of ways [Le 85]. It has been observed that the angular distribution of differential scattering cross sections of $\bar{p}$-A scattering is very much similar to that of heavy ion scattering whereas in case of p-A scattering the elastic differential scattering cross section decreases smoothly. At the same energy, $\bar{p}$-A scattering shows an oscillatory behaviour (as shown in Fig. 2.2.1). One of the most common approaches for the analysis of heavy ion scattering is the optical model potential approach. The above similarity leads to the use of this approach for the analysis of $\bar{p}$-A scattering data [He 85, In 86, Ja 86, Ku 85].

The standard form of the optical model potential having Woods-Saxon geometry is given by

$$V(r) = -V_0 f(r, R_r, a_r) - iW_0 f(r, R_i, a_i) + U_c(r) + V_{ls}(r), \tag{2.2.22}$$

where $f(r, R, a) = \left[1 + \exp\left(\frac{r - R}{a} \right) \right]^{-1}$,

$$R_r = r_r A_T^{1/3} \text{ and } R_i = r_i A_T^{1/3}.$$

V_0, r_r and a_r are the strength , radius and surface diffusenes parameters of the real part of the optical model potential respectively. W_0, r_i and a_i are the corresponding parameters of the imaginary part of the potential. A_T denotes the target mass number and U_c represents the Coulomb potential. The spin-orbit term in $\bar{p}$-A scattering is neglected, probably, because it does not affect the angular distribution of differential cross section and also due to non-existence of sufficient polarisation data [In 86]. Several other arguments are given in favour of the non-occurence of spin-orbit term [Do 78, Ja 86]. The optical model calculation was performed by using ECIS code of Raynal [Ra 81] on several targets like ^{12}C, ^{16}O, ^{40}Ca and ^{208}Pb at different energies. Optical model analysis fits the experimental data quite satisfactorily. A list of best fitted parameters of optical model potential for different systems is given in Table 2.2.4. Using these parameters the theoretically calculated angular distributions are shown in Figs. 2.2.5(a)-(c) and Figs.2.2.6(a)-(c) for three systems namely, $\bar{p} + {}^{12}C$, $\bar{p} + {}^{40}Ca$ and $\bar{p} + {}^{208}Pb$ at the energies indicated in the respective figures. Potential parameters also show a deep imaginary part and a shallow real part. This is an indication of the highly absorptive nature of $\bar{p}$-A scattering. It is known that phenomenological nuclear le 2.2.4 Best fitted optical potential parameters of $\bar{p}$-A scattering [Ja 86].

get	E_{lab} (MeV)	V_0 (MeV)	r_r (fm)	a_r (fm)	W_0 (MeV)	r_i (fm)	a_i (fm)	σ_R (mb)
	46.8	25	1.22	0.56	61	1.17	0.56	616
	179.7	44	1.05	0.56	184	0.935	0.56	510
a	47.8	9	1.4	0.63	143	1.03	0.63	1243
	179.8	40.5	1.1	0.63	111	1.1	0.63	1035
Pb	48.3	0.0	–	–	22	1.38	0.50	3458
	180.3	60	1.097	0.70	105	1.13	0.70	2710
	178.4	35	1.2	0.52	79	1.20	0.52	581
	178.4	38.5	1.05	0.62	150	0.98	0.62	660

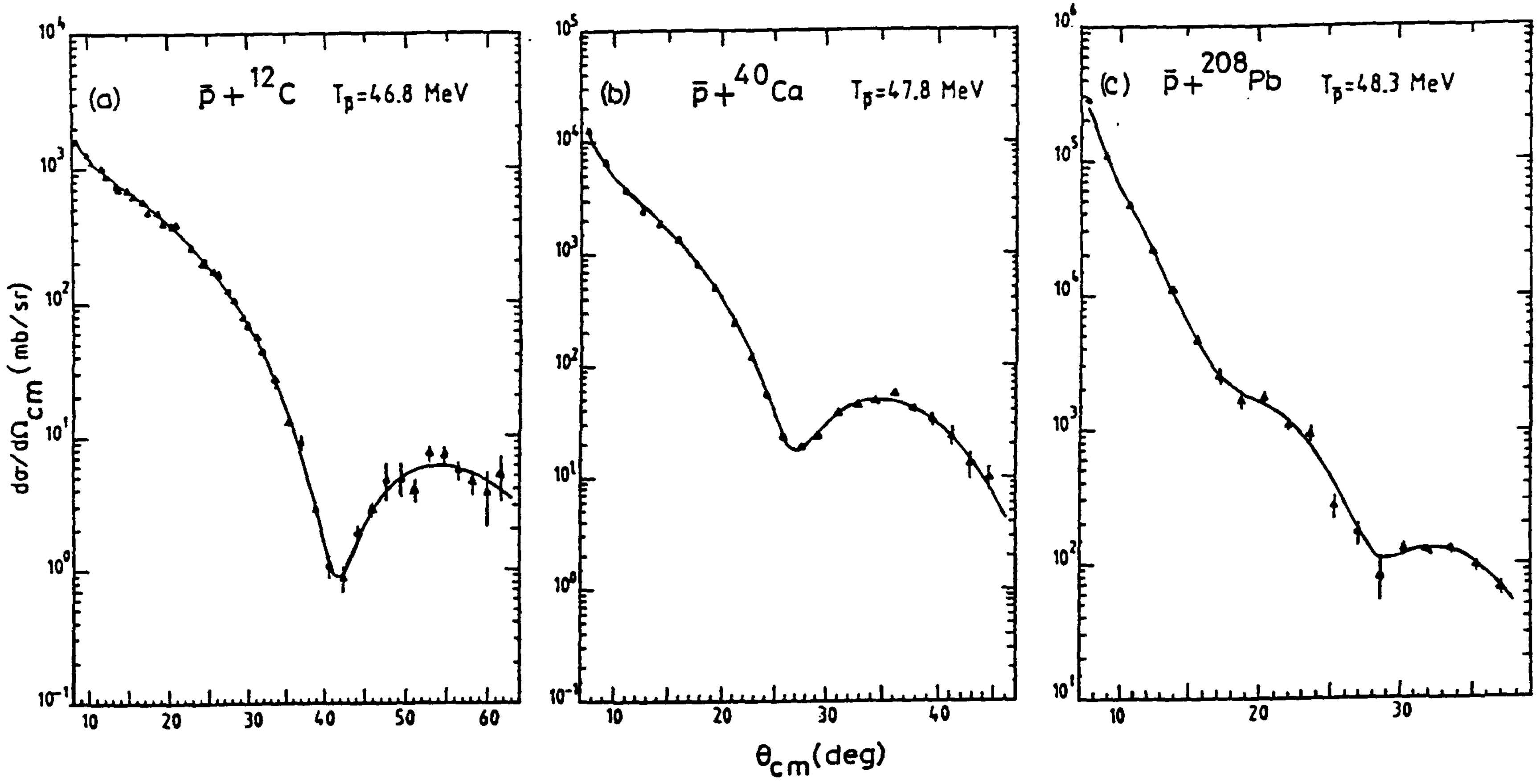

Fig.2.2.5(a)-(c) Angular distributions of differential scattering cross sections for $\bar{p}$-nucleus systems obtained by using optical model potential at low energy.

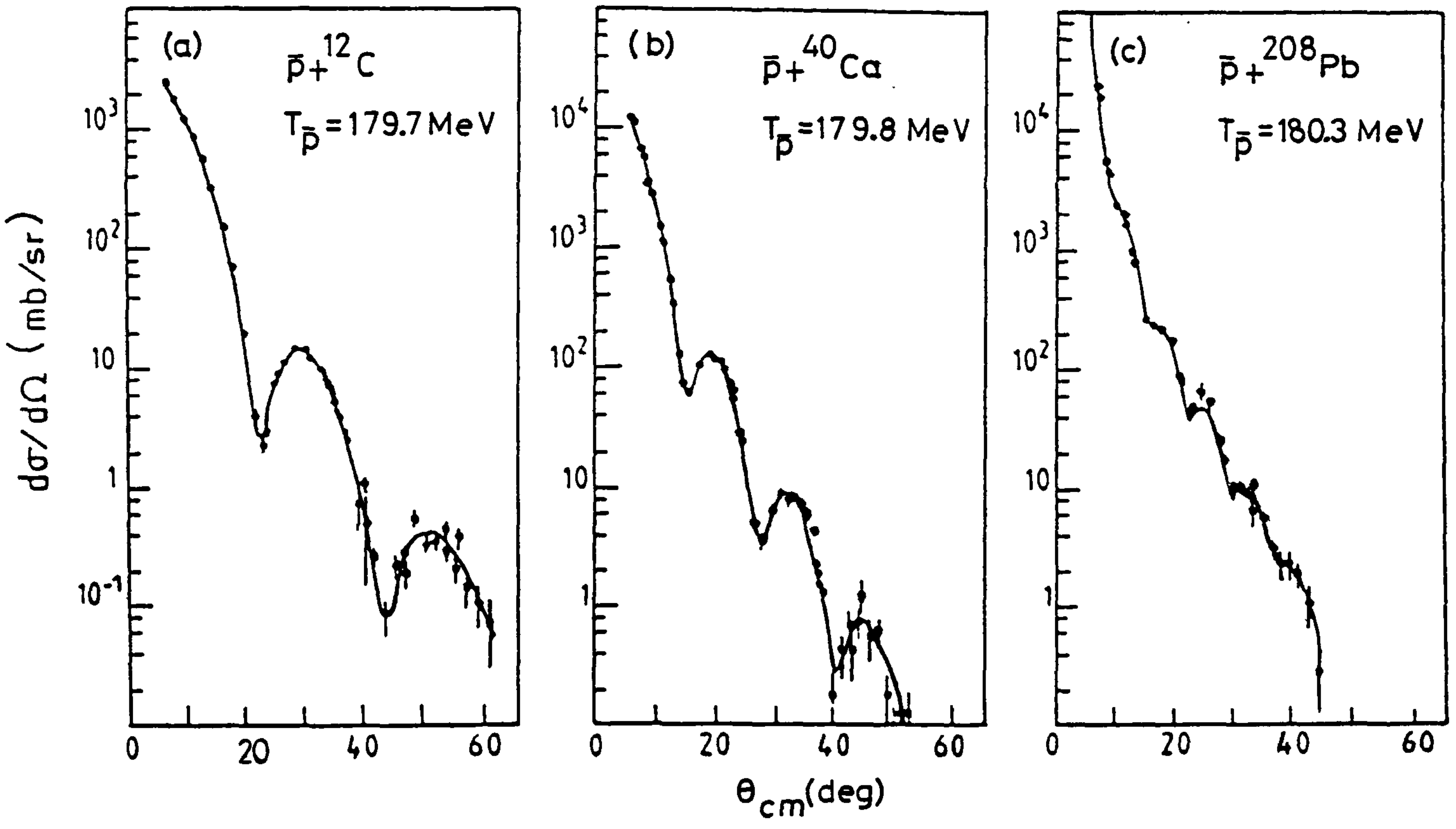

Figs.2.2.6(a)-(c)   Same as Fig.2.2.5(a)-(c) at high energy.

optical potentials are not unique which is true in $\bar{p}$-A case also. Ingemarsson [In 86] gave a large number of potentials which fit a particular $\bar{p}$-A scattering data at a given energy and gives practically the same χ^2 fit. A detailed study of these potentials shows that, near the nuclear surface and the region of strong absorption where $|W(R)| \geq 2|V(R)|$ the optical potentials are well determined. Correlations [He 85, Ja 86] between optical parameters were also investigated and the existence of parameter ambiguity was demonstrated by Kubo et al.[Ku 85]. Janouin et al. [Ja 86] realised that, the parameters at 180 MeV can be determined more correctly than at 46.8 MeV. Diffuseness and radius parameters of the imaginary potential can be determined more precisely than the real part. In order to describe the minima of the angular distribution, a small attraction around the nuclear surface is generally preferred for the real part. However, due to the minor role of the real part, a large degree of freedom exists in the choice of the potential geometry.

An examination of the real part of the potential in the surface region does not exhibit any pockets in the effective potential, which suggests that antinucleon-nuclear bound states may be difficult to observe.

Surface sensitivity of the optical potential and their comparative insensitivity to the inner region can be analysed as Igo ambiguity [Ig 58]. For strongly absorbed particles, all the potentials which behave similarly at the nuclear surface will reproduce the scattering data. In the case of Woods-Saxon potential (for real part)

$$V_0\left[1 + \exp\left(\frac{r - R_r}{a_r}\right)\right]^{-1} \longrightarrow V_0 \exp(R_r/a_r)\exp(-r/a_r), \quad r > R_r$$

$$= \mathrm{Const} \times \exp(-r/a_r) \qquad (2.2.23)$$

i.e., the combinations of the parameters V_0, R_r, a_r are such that $V_0\exp(R_r/a_r)$ = Constant. Such a relation is also satisfied by the imaginary part of the potential. A detailed study of $\bar{p}$-A potential shows that the potentials are uniquely determined near the region of absorption radius R_s which is the distance of closest approach for the Rutherford orbit of angular momentum $L_{1/2}$ such that

$$R_s = \frac{1}{k}\left\{\eta + \left[\eta^2 + L_{1/2}\,(L_{1/2} + 1)\right]^{1/2}\right\}, \qquad (2.2.24)$$

where η and k are the Coulomb parameter and the incident momentum respectively. $L_{1/2}$ is that partial wave for which modulus of the S matrix has the value of $|S_l| = 0.5$. In Table 2.2.5, the values of R_s, $V(R_s)$ and $W(R_s)$ for few $\bar{p}$-A systems are given. Comparing R_s with R, the radius obtained in the black disc diffraction model, shows that $R_s \approx R$. In spite of optical model potential parameter ambiguities the reaction cross section data are well determined and it is observed that like the strong absorption radius, the reaction cross section decreases with the increase in energy. Many attempts have been made to find a single potential which can reproduce the data for different target nuclei [Ja 86]. After several trials, a potential with fixed values of the potential strengths with $r_r = r_i = 1.1$ fm and a smooth dependence of the diffuseness with target mass A_T is achieved which can reproduce the data from ^{12}C to ^{208}Pb at a given energy. Diffuseness

Table 2.2.5 Potentials at the distance of a storng absorption radius $R_s(=r_s A_T^{1/3})$ for various $\bar{p}$-A systems at different energies [Ja 86].

System	$E_{\bar{p}}$ (MeV)	R_s (fm)	r_s (fm)	$V(R_s)$ (MeV)	$W(R_s)$ (MeV)
$\bar{p}+^{12}C$	46.8	3.65	1.59	-4.4	-9
	179.7	3.40	1.48	-6.7	-19
$\bar{p}+^{16}O$	178.4	3.65	1.45	-8.3	-17.7
$\bar{p}+^{18}O$	178.4	3.9	1.49	-5.3	-15.6
$\bar{p}+^{40}Ca$	47.8	5.25	1.55	-2.9	-8.7
	179.8	5.0	1.48	-5.0	-14.9
$\bar{p}+^{208}Pb$	48.6	8.5	1.44	-0.9	-7.7
	180.3	8.25	1.39	-4.5	-10.0

These values are determined with an accuracy of ∓ 0.1 fm for R and ∓2 Mev for $V(R_s)$ and $W(R_s)$.

parameter (a) is allowed to vary with A_T in the following way [Ja 86]:

$$a = 0.6366 + 0.0894(A_T^{1/3} - 40^{1/3}) + 0.118(N - Z)/A_T, \quad A_T \le 70$$

$$= 0.6366 + 0.0894(70^{1/3} - 40^{1/3}) + 0.118(N - Z)/A_T, \quad A_T \ge 70$$

The best fitted parameters are listed in Table 2.2.6. In view of the large uncertanities of the optical potential in the interior region, an approach, which does not start with a predetermined potential form like the Woods-Saxon form, is of interest. One such approach is the Fourier-Bessel expansion method [Fr 78, Gi 80]. This method gives good fit to the data and confirms the fact that the potentials are well determined only at large radii where nuclear density is less than 10% of the central value and at such distances the imaginary potential is about twice that of the real potential.

Table 2.2.6 Best fitted parameters of the potential for which only diffueseness depends on A_T [Ja 86].

Target	E_p (MeV)	V_0 (MeV)	W_0 (MeV)	$r_r = r_i$ (fm)	$a_r = a_i$ (fm)
^{12}C	179.7	40	105	1.1	0.54
^{16}O	178.4	40	105	1.1	0.56
^{18}O	178.4	40	105	1.1	0.58
^{40}Ca	179.8	40	105	1.1	0.64
^{208}Pb	180.3	40	105	1.1	0.72
^{12}C	46.8	18	105	1.1	0.54
^{40}Ca	47.8	18	105	1.1	0.64
^{208}Pb	46.8	18	105	1.1	0.72

Reference

[Al 78] Alkhazov. G.D, Belostotsky. S.L and Vorobyov. A.A, Phys. Reports 42C(1978) 89

[Am 85] Amos. K and Di Marzio. F, Z. Phys. A322(1985) 137

[Ar 88] Armstrong. T. A et al., Z. Phys. A332(1988) 467

[As 84] Ashford. V, Sainio. M.E, Sakitt. M et al., Phys. Rev. C30(1984) 1080

[Au 81] Auerbach. E.H, Dover. C.B, Kahana. S.H, Phys. Rev. Lett. 46(1981) 702

[Ba 64] Barnes. V et al., *Proc. Int. Conf. on High Energy Physics*, Dubna (1964) 731

[Ba 66] Baltay. C et al., Phys. Rev. 145(1966) 1103

[Ba 68] Bassel. R.H and Wilkin. C, Phys. Rev. 174(1974) 1179

[Ba 85] Balestra. F et al., Preprint CERN-EP/85-152, 1985

[Ba 86] Batusov. Y.A et al., Europhys. Lett. 2(1986) 115

[Ba 86a] Bacher. R et al., *International School of Physics with low energy antiprotons, Fundamental symmetries* (Erice, Sicily, Sept. 1986) Ed. by Ph. Bloch, R. Klapisch and P. Pavlopoulos (Plenum, New York)

[Ba 87] Balestra. F, Bossolasco.S et al., Nucl.Phys. A474(1987) 651

[Ba 87a] Batty. C.J, Phys. Lett. 189B(1987) 393

[Bi 69] Bizzarri. R et al., Lett. Nuovo Cim. 2(1969) 431

[Bl 60] Blair. J.S, Farwell. G.W and McDaniels. D.K, Nucl.Phys. 17(1960) 641

[Br 68] Bryan. R.A and Philipps. R, Nucl.Phys. B5(1968) 201

[Br 85] Brückner. W et al., Phys. Lett. **158B**(1985) 180

[Br 86] Brückner. W et al., Phys. Lett. **166B**(1986) 113

[Br 86a] Brückner. W et al., Phys. Lett. **169B**(1986) 302

[Ca 83] Cahay. M, Cugnon. J and Vandermeulen. J, Nucl. Phys. **A393**(1983) 237

[Ce 88] Cerutti. C et al., Nucl. Phys. **A476**(1988) 74

[Co 82] Coté. J, Lacombe. M, Loiseau. B, Moussallam. B and Vinh Mau. R, Phys. Rev. Lett. **48**(1982) 1319

[Cu 84] Cugnon. J and Vandermeulen. J, Phys. Lett. **146B** (1984) 16

[Cu 85] Cugnon. J and Vandermeulen. J, Nucl. Phys. **A445** (1985) 717

[Cu 87] Cugnon. J and Vandermeulen. J, Phys. Rev. C36(1987) 2726

[Cu 87a] Cugnon. J, Jasselette. P and Vandermeulen. J, Nucl. Phys. **A470**(1987) 558

[Cu 88] Cugnon. J, *AIP Conference Proceedings* 176 (New York 1988) Ed.by Gerry.M.Bunce p.379

[Cu 89] Cugnon. J and Vandermeulen. J, Ann. Phys. (Fr) **14** (1989) 49

[Cu 89a] Cugnon. J, Deneye. P and Vandermeulen. J, Nucl. Phys. **A500**(1989) 701

[Cu 89b] Cugnon. J. Nucl. Phys. B(Proc.Suppl.) 8(1989) 255

[Cu 89c] Cugnon. J and Vandermeulen. J, Phys. Rev. **C39**(1989) 181

[Da 77] Dalkarov. O.D and Myhrer.F, Nuovo Cim. **40A**(1977) 152

[Da 84] Dalkarov. O.D and Karmanov. V.A, Phys. Lett. **147B**(1984) 1

[Da 84a] Dalkarov. O.D, Karmanov. V.A, Pis´ma. Zh. Eksp. Teor. Fiz. 39(1984) 288 [JETP Lett. 39(1984) 345]; Zh. Eksp. Teor Fiz. 89(1985) 1122 [Sov. Phys. JETP 62(1985) 645]

[Da 85] Dalkarov. O.D and Karmanov. V.A, Nucl. Phys. **A445**(1985) 579

[Da 87] Dalkarov. O.D, Karmanov. V.A and Trukhov. A.V, Sov. J. Nucl. Phys.**45**(1987) 430

[Da 88] Dalkarov. O.D and Karmanov. V.A, Nucl. Phys. **A478**(1985) 635c

[De 78] Delville. A, Jasselette. P and Vandermeulen. J, Am. J.Phys. **46**(1978) 907

[De 85] Derreth. C, Greiner. W, Elze. H.-Th and Rafelski. J, Phys. Rev. **C31**(1985) 1360

[Di 83] Di Marzio. F and Amos. K, Aust. J. Phys. **36**(1983) 135; Phys. Rev. **C31**(1985) 561; Amos. K and Di Marzio. F, Phys. Rev. **C29**(1984) 1914

[Do 78] Dover. C.B and Richard. J.M, Phys. Rev. **D17**(1978) 1770

[Do 80] Dover. C.B and Richard. J.M, Phys. Rev. **C21**(1980) 1466

[Do 82] Dover. C.B and Richard. J.M, Phys. Rev. **C25**(1982) 1252

[Du 84] Dumbrajs. O, Fröhlich. J, Klein. U and Schlaile. H. G , Phys. Rev. **C29**(1984) 581

[Fr 78] Friedman. E and Batty. C.J, Phys.Rev.**C17**(1978) 34

[Fr 86] Friedman. E and Lichtenstadt. J, Nucl. Phys. **A455**(1986) 573

[Ga 84] Garreta. D et al., Phys. Lett. **135B**(1984) 266; **150B**(1985) 95

[Ga 84a] Garreta. D et al., Preprints CERN EP/84-114, EP/84-93; Phys. Lett. **149B**(1984) 64

[Ga 85] Garreta. D et al., Phys. Lett. **150B**(1985) 95

[Ga 85a] Garreta. D et al., *Contribution to the third LEAR workshop* (Tignes, 1985) 615

[Gh 74] Ghesquière.C, *Proceedings of the Symposium of $\overline{NN}$ Annihilation* (Liblice 1974) Ed. by L. Montanet, CERN 74-18, p.436

[Gi 80] Gils. H.J et al., Phys. Rev. **C21**(1980) 1239

[Gl 59] Glauber. R.G, *Lectures in theoretical physics*, Vol 1, Ed. by W.E. Brittin and L.G. Dunkam (Interscience, New York 1959) pp. 315-414 ; Sitenko. A.G, UKr. Phys. J. **4**(1959) 152

[Gl 67] Glauber. R.J, *High energy physics and nuclear structure* Ed. by G. Alexander (North-Holland, Amsterdam 1967) p. 311; Uspekhi. Fiz. Nauk. **103**(1971) 641

[Gl 69] Glauber. R, "Theory of Collisions of High-Energy Hadrons with Nuclei", *Third. Int. Conf. on High energy physics and nuclear structure* (Columbia Univ., Sept. 1969); Sitenko. A.G, Ukr. Fiz. Zh.**4**(1959) 152

[He 85] Heiselberg. H et al., Nucl. Phys. **A446**(1985) 637

[He 87] Hernández. E and Oset.E, Phys. Lett. **184B**(1987) 1

[Ig 58] Igo. G, Phys.Rev. Lett. **1**(1958) 72 ; Phys.Rev.**115**(1959) 1665

[In 65] Inopin. E.V and Berezhnoy. Yu. A, Nucl. Phys. **63**(1965) 689

[In 86] Ingemarsson. A, Nucl. Phys. **A454**(1986) 475

[Ja 86] Janouin. S et al., Nucl. Phys. **A451**(1986) 541

[Ja 88] Jasselette. P, Cugnon. J and Vandermeulen. J, Nucl. Phys.**A484**(1988) 542

[Ka 84] Kahana. S, *Proceedings of the Workshop "Physics at LEAR "*, Ed. by U. Gastaldi and R. Klapisch (Plenum, New York, 1984) p.495

[Ke 59] Kerman. A.K, McManus. M and Thaler. R.M, Ann. Phys. 8(1959) 551

[Ko 87] Ko. Che Ming and Yuan. Ruixi, Phys. Lett. **192B**(1987) 31

[Ku 85] Kubo. K.-I, Toki. H and Igarashi. M, Nucl. Phys. **A435**(1985) 708

[Le 74] Leon. M and Seki. R, Phys. Lett. **48B**(1974) 173

[Le 85] Lemaire. M.C, *Contribution to the Proc. Int. Symp.on Nucleon and antinucleon scattering* (Bad Honnef, 1985) Lecture Notes in Physics (Springer)243

[Li 85] Lichtenstadt. J and Yavin. A.I et al., Phys. Rev. C32(1985) 1096

[Ma 76] Margolis. B, Meggs. W.J and Weiss. N, Phys. Rev. D13(1976) 2551

[Ma 87] Mahalanabis. J, J. Phys. G: Nucl. Phys. 13(1987) 925

[Mö 75] Möhring. H et al., Nucl. Phys. B85(1975) 227

[Mo 75] Montanet. L, (1975) Private communication (see ref.[Cu 89]

[Mo 86] Moser. E.F et al., Phys.Lett. 179B(1986) 25

[Mo 86a] Moser. E.F, Thesis, TUM, Munchen (1986) Unpublished.

[Mi 84] Miyano. K, Noguchi. Y, Fukawa. M, Kohriki. E, Ochiai. F, Sato. T, Suzuki. A, Takahashi. K, Yoshimura. Y, Fujiwara, Noguchi. S, Yamashita. S and Ono. A, Phys.

Rev. Lett. 53(1984) 1725; Neutral strange particle productions and inelastic cross section in $\bar{p}$ + Ta reaction at 4GeV/c, KEK Preprint 87-160 (February 1988)

[Na 84] Nakamura. K et al., Phys. Rev. Lett. 52(1984) 731

[Na 87] Nazaruk. V.I, Sov. J. Nucl. Phys. 46(1987) 51

[Ng 87] Ngô. C et al., Journal. de. Phys. C2(1987) 157

[Oh 73] Oh. B.Y et al., Nucl. Phys. B51(1973) 57

[Or 73] Orfanidis. S.J and Rittenberg. V, Nucl. Phys. B59(1973) 570

[Ph 87] Phatak. S.C, and Sarma. N, Phys. Rev. C36(1987) 864

[Po 56] Pontecorvo. B.M, Zh. Eksp. Teor. Fiz. 30(1956) 947 [Sov. Phys. JETP. 3(1957) 966]

[Po 86] Povh. B and Walcher. Th, Comm. Nucl. Part. Phys. 16 (1986) 85

[Po 88] Poth. H, Nucl. Phys. A478(1988) 655c

[Ra 80] Rafelski. J, Phys. Lett. 91B(1980)281

[Ra 81] Raynal. J, Phys. Rev. C23(1981) 2572 and references therein

[Ra 84] Rafelski. J, "*Physics at LEAR* " Ed. by U. Gastaldi and R.Klapisch. (Plenum, New York 1984)

[Re 88] Reifenröther. G, Klempt. E and Landua. R, Phys. Lett. 203B(1988) 9

[Ru 66] Rubinstein. H.R and Stern. H, Phys. Lett. 21(1966) 447

[Sh 78] Shapiro. I.S, Phys. Reports 35C(1978) 129

[Sh 87] Shibata. T.- A, Phys. Lett. 189B(1987) 232

[Sh 88] Shibata. T.- A, Nucl. Phys. A478(1988) 623c

[Th 85] Thaler. J, J. Phys. G: Nucl. Phys. 11(1985) 689

[Va 74] Vandermeulen. J, Lett. Nuovo Cim. 11(1974) 243

[Va 78] Vandermeulen. J, Lett. Nuovo Cim. 21(1978) 33

[Va 80] Vandermeulen. J, Lett. Nuovo Cim. 28(1980) 60

[Wi 72] Willmes. H et al., Part. Nuclei. 4(1972) 192

[Ya 87] Yavin. Avivi. I, Can. J. Phys. 65(1987) 647

[Za 87] Zavarzina. V.P and Sergeev. V.A, Sov. J. Nucl. Phys. 46(1987) 261 and references therein (e.g. 1, 2, 4, 6, 7)

CHAPTER 3

SEMICLASSICAL AND CLOSED FORMALISM APPROACHES TO ANTIPROTON-NUCLEUS SCATTERING

3.1 Introduction

The major advances in our understanding of atomic nuclei have taken place as a result of detailed exploration of nuclei using a variety of probes like electrons, nucleons, deuterons and heavy ions. During the last two decades the information generated by heavy ion scattering (HIS) has evolved as a major area of nuclear physics. More recently, scattering and reaction experiments conducted on different nuclei using antiproton ($\bar{p}$) as projectile have initiated a new line of exploration of the nuclei [Ga 84, In 86, Ja 86, Kr 84, Ku 85, Ma 84] which is of much interest due to several reasons. These can provide a better idea of the interaction of antiprotons with the nuclear matter, antiproton-nucleus ($\bar{p}$-A) potentials, additional reaction channels due to annilhilation of antiproton etc. The experiments and theoretical calculations carried out so far provide interesting similarities between antiproton-nucleus scattering and heavy ion - nucleus scattering. Both of these are predominantly surface dominated phenomena and in general, the inner regions of the interaction potentials are not uniquely determined. In both cases nuclei appear as highly absorptive spheres and the differential scattering cross sections show characteristic diffraction patterns. Physical origin of the surface dominance in these cases, however, appears to be different. The heavy ion scattering, in general, is dominated by a high Coulomb barrier. As a result, the interacting nuclei get slowed down in the barrier region and hence, most of the reaction process at low energy takes place around the barrier region which makes the surface region of the potential comparatively well determined. Most of the partial waves below the grazing partial wave get completely absorbed and hence, are not helpful in uniquely determining the potential in the interior region. On the other hand, the surface dominance of antiproton-nucleus scattering has a different origin. In this case there is no Coulomb barrier and for some partial waves there may be a very low barrier due to centrifugal term. The surface dominance of antiproton-nucleus scattering is due to the large number of additional channels that open up due to annihilation process generated by proton-antiproton collisions. The scattering wave gets strongly attenuated in the surface region due to these additional channels and hence, only limited information regarding the surface region of the interaction is possible. In the case of HIS, very important approaches have been developed for the analysis of the scattering data. In view of the comparatively smooth behaviour of the heavy ion potential and very small de Broglie wavelength involved, semiclassical methods [Br 72, Br 74, Fo 59, Fr 75, Ko 75, Ma 75, Mc 70] of collision theory have been widely used in HIS and the data have been analysed in terms of phenomenon like rainbow and glory scattering. On the other hand based on the fact that, HIS is a highly absorptive process leading to a smooth variation of the magnitude and the phase of the partial wave S matrix, diffraction models using the parametrised form of S matrix have been developed in HIS [Fr 78]. These models can explain very successfully the diffraction patterns like

Fraunhofer and Fresnel diffraction which are common in HIS. In view of the several similarities between antiproton-nucleus scattering and HIS, we have investigated the applicability of semiclassical methods and closed formalism [Fr 78] for the analysis of $\bar{p}$-A scattering data. A brief description of semiclassical approach and the scattering phase shift is given in Sec.3.2. Section 3.3 deals with the comparative study of effective potentials and reflection functions in the heavy ion-nucleus and antiproton-nucleus collisions. Antiproton-nucleus scattering data are analysed using WKB technique which is described in Sec. 3.4. In Sec. 3.5, the closed formalism approach incorporating the parametrised form of S matrix is discussed. Section 3.6 discusses typical numerical results obtained by WkB technique and the parametric S matrix approach.

3.2.1 Semiclassical approach

Semiclassical methods are useful when the de Broglie wavelength of relative motion is small as compared to some characteristic dimension of the system. In such cases, the problem can be treated semiclassically, i.e., the classical concepts can be applied to a good degree of accuracy. If two nuclei having mass numbers A_P and A_T collide the corresponding wave number (k) of relative motion is $k = (\mu v/\hbar)$, where $\mu = A_PA_T/(A_P+A_T)$ is the reduced mass and $v = (2E_{lab}/A_P)^{1/2}$ is the asymptotic relative velocity. Three dimensionless variables [Sa 78] which are frequently used to compare the values of k are:

(1) Sommerfeld parameter $\eta = ka_c$, compares the de Broglie wavelength with the Coulomb length parameter a_c ($a_c = Z_PZ_Te^2/2E$).

E denotes the asymptotic kinetic energy of relative motion

$$E = (1/2)\mu v^2 = E_{lab}\, A_T/(A_P + A_T). \qquad (3.2.1)$$

Here Z_P and Z_T are the proton numbers of projectile and target nuclei respectively.

(2) kR_s compares the wavelength with the strong absorption radius R_s ($R_s \approx r_s(A_P^{1/3} + A_T^{1/3})$, r_s = 1.5 fm).

(3) ka compares the wavelength with the surface diffuseness parameter a (typically a ≈ 0.5 fm).

Due to larger mass, size and electric charge of heavy ions as compared to conventional light projectiles, a typical heavy ion collision (HIC) may evince three basic features (i) short wavelength, (ii) strong Coulomb interaction and (iii) strong absorption. These characteristic features help to distinguish them from the reactions of light nuclei at medium energies. This wavelength remains small even if one takes Coulomb repulsion into account [Sa 78]. In Table 3.2.1 some values of the parameters are listed for a number of pairs of nuclei at the laboratory energy E_{lab} (= $8A_P$ MeV) of the projectile. From the table it is clear that when both the particles (i.e., projectile and target) are light, $\eta \approx 1$ and in other cases, $\eta \gg 1$. kR_s is large and $ka \gg 1$, for all pairs of nuclei. These characteristic features of heavy ion systems show that classical and semiclassical descriptions are useful in the analysis of HIS data. In the case of Rutherford orbit, the impact parameter (b) and the distance of closest approach (d) are given by :

$$b = a_c \cot(\theta/2) \qquad (3.2.2)$$

and

$$d = a_c + \left[a_c^2 + b^2\right]^{1/2} \qquad (3.2.3)$$

Table 3.2.1 Values of various parameters for few heavy ion systems [Br85].

Target	Projectile	R_s (fm)	η	kR_s	ka
^{16}O	α	6.2	0.9	12.0	1.0
	^{12}C	7.2	2.7	30.0	2.1
^{40}Ca	α	7.5	2.2	17.0	1.1
	^{12}C	8.6	6.7	49.0	2.8
	^{40}Ca	10.3	22.5	127.0	6.1
^{58}Ni	α	8.2	3.1	19.0	1.1
	^{12}C	9.2	9.4	56.0	3.0
	^{40}Ca	10.9	31.5	158.0	7.2
^{208}Pb	α	11.3	9.2	27.0	1.2
	^{12}C	12.3	27.7	86.0	3.5
	^{40}Ca	14.0	92.2	289.0	10.3

where θ is the scattering angle in the centre-of-mass system and the interaction radius R is $R = r_0\ (A_P^{1/3} + A_T^{1/3}) \approx R_1 + R_2$. Semiclassically, the orbital angular momentum l is associated with the impact parameter b through the relation

$$\left[l(l+1)\right]^{1/2} \approx l + (1/2) = \lambda = kb. \tag{3.2.4}$$

For the grazing collision, d $\simeq$ R and is related to the Rutherford grazing angle θ_R through the relation

$$R = (\eta/k)\left[\ 1 + 1/\sin\ (\theta_R/2)\ \right] \tag{3.2.5}$$

and the corresponding impact parameter for grazing trajectory is

$$B = (\eta/k)\ \cot(\theta_R/2). \tag{3.2.6}$$

The grazing angular momentum is

$$\Lambda = l_g + 1/2 = kB = \eta\ \cot(\theta_R/2)$$

$$= kR\ \left[1 - 2\eta/(kR)\right]^{1/2}. \tag{3.2.7}$$

In general, $\eta \gg 1$ for HIC and hence, large value of η implies the applicability of semiclassical methods. Thus, under certain conditions heavy ion systems behave, to a large extent, like classical bodies moving in a definite trajectory. The first two properties (i) and (ii) suggest that, the HIC can be described to a great extent by classical mechanics and this has led to the development of semiclassical theories in recent years. Superposition and interference from different classical trajectories gives quantal effect. The third property of HIC ,i.e., the strong absorption character introduces complications in semiclassical theories. Weak absorption can be treated in a perturbative way but the strong absorption leads to wave mechanical effect, i.e., the wave propagates into the classically forbidden region. Blair first used semiclassical theories to analyse the elastic [Bl 54] and inelastic [Bl 59] scattering data of α-particles and later it was applied extensively [Br 72, Br 74, Fr 63, Fr 78, Ko 75, Ma 75, Mc 70] to HIS.

3.2.2 Semiclassical formulation of nuclear phase shift

One of the techniques of semiclassical analysis of the problem is to use WKB approximation where WKB radial wave function and the approximate phase shifts are obtained. For a spherically symmetric potential V(r) the radial Schrodinger equation is

$$\frac{d^2U_l(r)}{dr^2} + k^2(r)U_l(r) = 0 \tag{3.2.8}$$

where the local wave number k(r) is defined as follows:

$$k^2(r) = \frac{2\mu}{\hbar^2}\left[E - V_{eff}(r)\right] \tag{3.2.9}$$

and the corresponding momentum is $p(r)= \hbar k(r)$.

The effective potential which is denoted by $V_{eff}(r)$ can be expressed as

$$V_{eff}(r) = V(r) + \frac{\hbar^2}{2\mu r^2}\, l(l+1) \tag{3.2.10}$$

In the HIS, it is seen that if the incident energy of the projectile is such that it is above the Coulomb barrier, the real part of the effective potential will give one classical turning point. This is also true for energies below the potential pocket of the effective potential. If the energies lie in between the potential pocket and potential barrier height real effective potential will give three turning points. However, in most cases the two interior turning points lie in the absorptive region and hence, the scattering will be dominated by the region outer to the outermost turning point. Here we consider the case of the potential such that $k(r)$ has only one zero, for $r > 0$ ($k(r_o)=0$, corresponds to classical turning point). In the case of HIS, in the high energy region (energies above the Coulomb barrier) as well as the low energy region (energies below the potential pocket of the effective potential) this holds good. Thus, the semiclassical theory described here is obtained for the potential having one turning point only. We consider the case of $V(r)$ such that

$$k^2(r) > 0 \text{ , when } E > V_{eff}(r)$$

$$\text{and} \quad k^2(r) < 0 \text{ , when } E < V_{eff}(r).$$

At the classical turning point r_o, $k(r_o)=0$, i.e., $V_{eff}(r_o) = E$ and the region $r > r_o$ is allowed classically ($E > V_{eff}(r)$) and $r < r_o$ is classically forbidden ($E < V_{eff}(r)$). Assuming the solution of the Schrödinger equation (3.2.8) to be of the form [Jo 75]

$$U_l(r) = A \exp(iS(r)/\hbar), \qquad (3.2.11)$$

where $S(r)$ satisfies inhomogeneous non-linear differential equation

$$i\hbar S''(r) - (S'(r))^2 + 2\mu(E - V_{eff}(r)) = 0. \qquad (3.2.12)$$

Here, $S'(r)$ and $S''(r)$ stand for $dS(r)/dr$ and $dS'(r)/dr$ respectively. In the classical limit $\hbar \longrightarrow 0$, Eq.(3.2.12) reduces to the form

$$(S'(r))^2 = 2\mu(E - V_{eff}(r)).$$

This condition can also be obtained (without making $\hbar \longrightarrow 0$), if

$$|\hbar S''(r)| \ll |(S'(r))^2|.$$

Now, assuming $S(r)$ as a power series in $\hbar$,

$$S(r) = S_0(r) + \hbar S_1(r) + \hbar^2 S_2(r) + \ldots\ldots\ldots \qquad (3.2.13)$$

and substituting $S(r)$ into Eq. (3.2.12) one gets

$$(S_0'(r))^2 = 2\mu\ (E - V_{eff}(r)) = \hbar^2\ k^2(r)$$

$$iS_0''(r) - 2S_0'(r)\ S_1'(r) = 0, \text{ etc.}$$

Integrating these equatuions one obtains

$$S_0(r) = \pm\hbar \int^r k(r)\ dr \tag{3.2.14}$$

and

$$S_1(r) = \frac{i}{2} \ln k(r), \quad E \quad V_{eff}(r)\ . \tag{3.2.15}$$

This gives the solution of the form

$$U_l(r) = A\ [k(r)]^{-1/2} \exp\left[\pm\ i\int^r k(r')dr'\right], \qquad E \quad V_{eff}(r) \tag{3.2.16}$$

and

$$U_l(r) = B\ [\gamma(r)]^{-1/2} \exp\left[\pm \int^r \gamma(r')dr'\right], \qquad E \quad V_{eff}(r) \tag{3.2.17}$$

Here $k(r) = i\gamma(r)$, $\gamma^2(r) = (2\mu/\hbar^2)(V_{eff}(r) - E)$. Substituting these solutions in the Schrodinger equation one obtains the following conditions:

$$\frac{|dk(r)/dr|}{|k^2(r)|} \ll 1 \tag{3.2.18}$$

and $$\frac{|d^2k(r)/dr^2|}{|k^3(r)|} \ll 1 \tag{3.2.19}$$

for the validity of the approximations made. Alternatively, one can write Eq.(3.2.18) as

$$\lambda\!\!\!^{-}(r)\ |dp(r)/dr| \ll |p(r)|,$$

where $\lambda\!\!\!^{-}(r) = 1/k(r)$.

These conditions are not valid near the classical turning point and hence, near the turning point one should examine the problem critically. Thus, we consider only that solution described in equations (3.2.16) and (3.2.17) which gives the appropriate solution for the scattering case. Assuming there is only one turning point (r_o), and $k^2(r) < 0$ for all $r < r_o$ the solution of the Schrodinger equation is

$$U_l(r) \simeq 1/2 \sqrt{1/\gamma(r)}\, \exp\left(-\int_r^{r_o} \gamma(r')\,dr'\right), \qquad r < r_o \qquad (3.2.20)$$

and

$$U_l(r) \simeq \sqrt{1/k(r)}\, \cos\left(-\int_r^{r_o} k(r')\,dr' - \pi/4\right), \quad r > r_o \qquad (3.2.21)$$

The solutions give $U_l(r) = 0$ at the origin and also a linear combination of $\exp(+ik(r))$ and $\exp(-ik(r))$ at infinity. The exact solution $U_l(r)$ has the behaviour r^{l+1} near the origin which cannot be completely reproduced in Eq.(3.2.20). Near the origin the centrifugal term dominates and $U_l(r)$ in Eq.(3.2.20) can be written in the form

$$U_l(r) \underset{r \to 0}{\simeq} \text{const} \times r^{1/2} \times \exp\left[\left[l(l+1)\right]^{1/2} \ln r\right] \qquad (3.2.22)$$

Langer noticed that, it is possible to get the desired r^{l+1} behaviour within the WKB formulation by replacing $l(l+1)$ by $(l+1/2)^2$ in the centrifugal term. This approximation is valid for large l and is known as Langer correction [La 34, La 37]. In HIS lower partial waves are fully absorbed and hence, $(l+1/2)^2$ can be used in place of $l(l+1)$ and the wave number $k(r)$ is also modified by taking Langer correction into account. The asymptotic behaviour of the solution $U_l(r)$ as $r \longrightarrow \infty$ determines the scattering phase shift. We get

$$U_l(r) \underset{r\to\infty}{\simeq} \frac{1}{k} \sin\left[(r - r_o)k + \int_{r_o}^{r} dr' \left\{F(r') - k\right\} + \pi/4 \right], \tag{3.2.23}$$

where $F(r) = \left[k^2 - Q(r) - (l + 1/2)^2/r^2 \right]^{1/2}$.

$Q(r) = \dfrac{2\mu}{\hbar^2} V(r)$ and k is the asymptotic wave number which is given by

$$k(\infty) = k = \left(2\mu E/\hbar^2\right)^{1/2} \tag{3.2.24}$$

This approximate method developed above is the well known WKB approximation. Comparing Eq. (3.2.23) with the asymptotic form of the radial wave function [Jo 75]

$$U_l(r) \xrightarrow[r\to\infty]{} A_l \sin(kr - l\pi/2 + \delta_l)$$

one can write WKB phase shift as

$$\delta_l^{WKB} = \frac{\pi}{2} (l + 1/2) - kr_o + \int_{r_o}^{\infty} \left[F(r') - k\right] dr'. \tag{3.2.25}$$

It is interesting to evaluate the WKB phase shift for Coulomb potential. For the Coulomb potential $v_c(r)$, the semiclassical form for a radial scattering wave function with the Langer correction contains the integral $\int_{r_c}^{r} k_c(r')dr'$ which can be evaluated exactly to give [Br 85]

$$\int_{r_c}^{r} k_c(r')dr' = rk_c(r) - \eta \ln(rk_c(r) + rk - \eta) + (1/2)\eta \ln(\eta^2+\lambda^2)$$
$$+ \lambda \sin^{-1}\left[\frac{\eta kr + \lambda^2}{kr(\eta^2+\lambda^2)^{1/2}} \right] - \pi\lambda/2, \tag{3.2.26}$$

where $k(r) = k_c(r) = k\left[1 - 2a_c/r - b^2/r^2 \right]^{1/2}$,

$k = 2\mu E/\hbar^2$, $kb = \lambda = l+1/2$

and $\eta = ka_c$ with $a_c = Z_p Z_T e^2 \mu / \hbar^2 k$.

Here r_c is the Coulomb turning point ($k_c(r_c) = 0$) which is given by

$$r_c = a_c + \left(a_c^2 + b^2 \right)^{1/2}. \tag{3.2.27}$$

From Eq. (3.2.26), for large r, the Coulomb phase shift is

$$\sigma_l^{WKB} = \frac{1}{2} \eta \ln (\eta^2 + \lambda^2) - \eta + \lambda \tan^{-1} (\eta/\lambda) \tag{3.2.28}$$

The exact expression for the Coulomb phase shift is $\sigma_l = \arg \Gamma (l+1+i\eta)$ which is asymptotically equal to σ_l^{WKB} in Eq. (3.2.28) if either $\eta \gg 1$ or $\lambda^2 \gg \eta$. In the presence of the nuclear potential $v_n(r)$ the total phase shift δ_l can be expressed as the sum of Coulomb and nuclear phase shifts

$$\delta_l = \sigma_l + \delta_N(l)$$

In the WKB approximation, one can write

$$\int_{r_o}^{r} k(r)dr = \int_{r_c}^{r} k_c(r)dr + \left[\int_{r_o}^{r} k(r)dr - \int_{r_c}^{r} k_c(r)dr \right], \tag{3.2.29}$$

where $V(r) = v_n(r) + v_c(r)$.

The first integral corresponds to the Coulomb phase shift which is given by Eq.(3.2.26) and the term within the square bracket is equal to the nuclear phase shift. Thus the nuclear phase shift within the framework of WKB approximation is

$$\delta_N(l) \simeq \int_{r_o}^{R} k(r)dr - \int_{r_c}^{R} k_c(r)dr, \tag{3.2.30}$$

where

$$k(r) = \left[\frac{2\mu}{\hbar^2} \left(E - v_n(r) - v_c(r) - \frac{\hbar^2}{2\mu} \frac{\lambda^2}{r^2} \right) \right]^{1/2}$$

and

$$k_c(r) = \left[\frac{2\mu}{\hbar^2} \left(E - v_c(r) - \frac{\hbar^2}{2\mu} \frac{\lambda^2}{r^2} \right) \right]^{1/2}.$$

The upper limit R is chosen to be outside the range of the nuclear interaction so that $V(r) = V_C(r)$, $r \geq R$. Thus Eq.(3.2.30) is the semiclassical formula for nuclear phase shift which is used to get the closed form expression for $\delta_N(l)$.

3.3 Comparison of antiproton-nucleus and nucleus-nucleus scattering

Before proceeding to analyse $\bar{p}$-A scattering data using semiclassical methods we give a comparative study between the antiproton-nucleus and nucleus-nucleus scattering. Phenomenologically it is found that elastic scattering in both cases can be described using the standard Woods-Saxon form for the phenomenological nuclear optical model(OM) potential. Thus, the total optical model potential for the antiproton-nucleus or the nucleus-nucleus problem can be written as:

$$\begin{aligned} V(r) &= -V_0 f(r,\ a_r,\ R_r) - i\ W_0 f\ (r,\ a_i,\ R_i) + U_C(r) \\ &= U_N(r) + U_C(r), \end{aligned} \qquad (3.3.1)$$

where $f(r,\ a,\ R) = \left[1 + \exp\left(\dfrac{r - R}{a}\right)\right]^{-1}$.

V_0 and W_0 in Eq.3.3.1 represent the depth parameters of the real and imaginary parts of the potential and are positive numbers. a_r and a_i are their respective surface diffuseness parameters. R_r and R_i are obtained from their radius parameters r_r and r_i respectively. Here $U_C(r)$ is the Coulomb potential due to a point charge and a uniformly charged sphere of radius R_C and is given by

$$U_C(r) = (Z_P Z_T e^2/2R_C)(3 - (r^2/R_C^2)), \qquad r \leq R_C \qquad (3.3.2)$$

$$= Z_P Z_T e^2/r \ . \qquad\qquad r \geq R_c$$

In the case of HIS, the parameters R_r, R_i and R_c are given by

$$R_r = r_r \ (A_P^{1/3} + A_T^{1/3})$$

$$R_i = r_i \ (A_P^{1/3} + A_T^{1/3})$$

and $R_c = r'_c \ (A_P^{1/3} + A_T^{1/3})$.

In the antiproton-nucleus scattering case

$$R_r = r_r \ A_T^{1/3}$$

$$R_i = r_i \ A_T^{1/3}$$

and $R_c = r'_c \ A_T^{1/3}$.

The quantities r_r, r_i and r'_c are the radius parameters. Here Z_P and Z_T denote the atomic numbers of projectile and target nuclei respectively and A_P, A_T are the respective mass numbers. The effective potential corresponding to the l^{th} partial wave in the radial Schrodinger equation is

$$V_{eff}(r) = V(r) + (\hbar^2/2\mu) \left[l(l + 1)/r^2 \right], \qquad (3.3.3)$$

where $\mu = A_P A_T/(A_P + A_T)$ denotes the reduced mass. Here we have considered a typical case of heavy ion scattering and compared it with antiproton-nucleus scattering. The typical cases of heavy ion and antiproton scattering considered are $^{18}O + {}^{58}Ni$ at $E_{lab} = 60$ MeV and $\bar{p} + {}^{12}C$, $\bar{p} + {}^{40}Ca$ and $\bar{p} + {}^{208}Pb$ at $E_{lab} = 46.8$ MeV. All the systems are analysed using phenomenological optical model potential. The optical model (OM) potential parameters used by us and the other relevant parameters are listed in Table 3.3.1.

In Figs. 3.3.1a – 3.3.1d, the effective potentials are plotted for various partial waves for different systems namely, $^{18}O + {}^{58}Ni$, $\bar{p} + {}^{12}C$, $\bar{p} + {}^{40}Ca$ and $\bar{p} + {}^{208}Pb$ at the energies as indicated in the corresponding figures. From the comparison of effective potentials of $^{18}O + {}^{58}Ni$ and $\bar{p}$-A systems for different

Table 3.3.1 Potential parameters for $^{18}O + {}^{58}Ni$ and $\bar{p}$ - nucleus systems . E is the centre of mass energy.

System	$\bar{p} + {}^{12}C$	$\bar{p} + {}^{40}Ca$	$\bar{p} + {}^{208}Pb$	$^{18}O + {}^{58}Ni$
E_{lab}(MeV)	46.9	46.8	46.8	60.0
E(MeV)	43.2	45.66	46.6	45.79
$k(fm^{-1})$	1.38	1.46	1.49	5.49
η	-0.138	-0.46	-1.89	19.32
V_0(MeV)	40.0	40.0	20.0	90.1
r_r(fm)	1.03	1.10	1.10	1.22
a_r(fm)	0.562	0.60	0.65	0.50
W_0(MeV)	74.1	100.0	140.0	42.9
r_i(fm)	1.07	1.10	1.10	1.22
a_i(fm)	0.625	0.60	0.65	0.50
r'_c(fm)	1.3	1.3	1.3	1.25
Reference	[Ku 85]	[He 85]	[He 85]	[Vi 76]

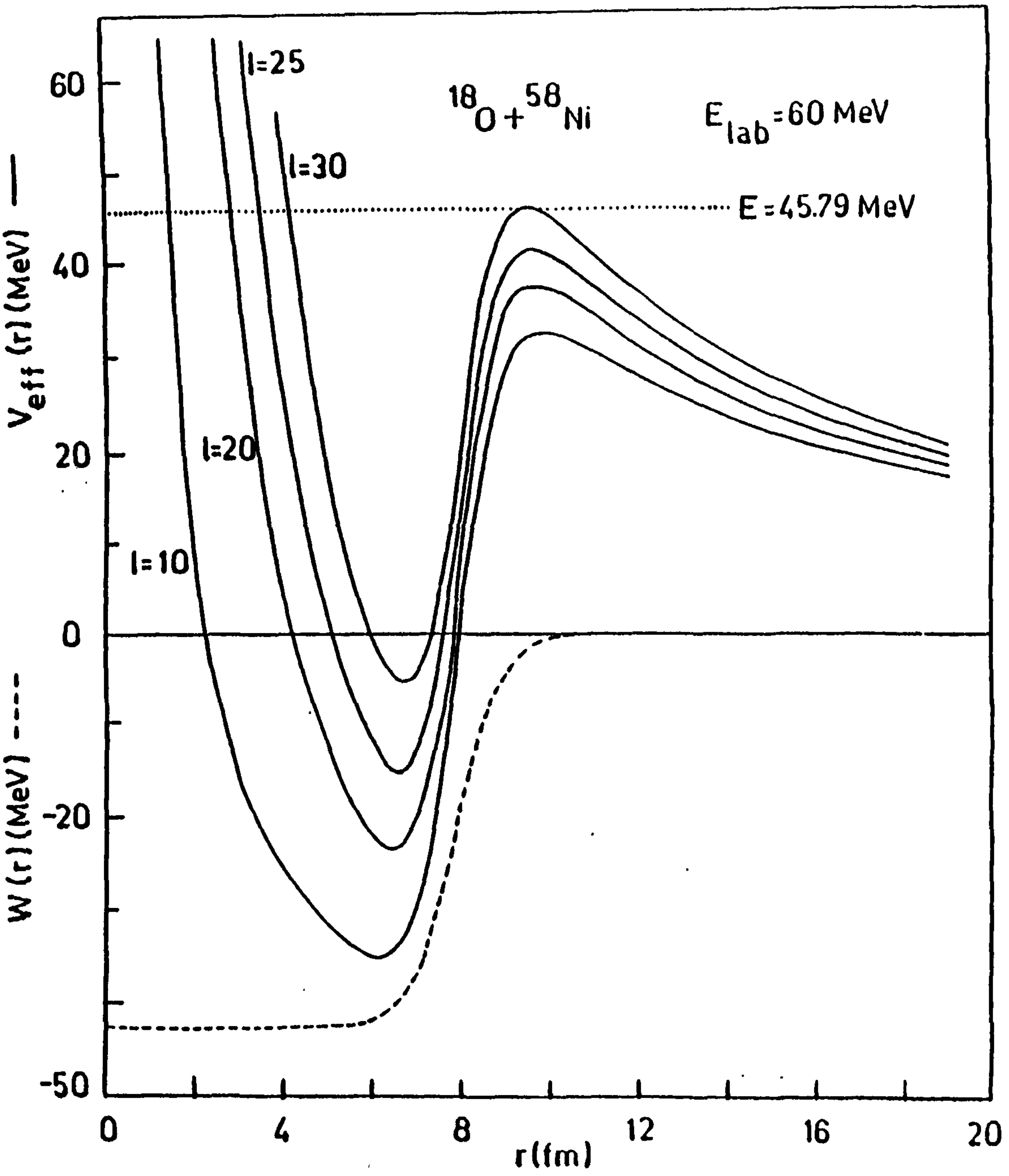

Fig.3.3.1a Plot of effective potential as a function of r for several values of l for ^{18}O + ^{58}Ni at E_{lab} = 60 MeV. Potential parameters are given in Table 3.3.1.

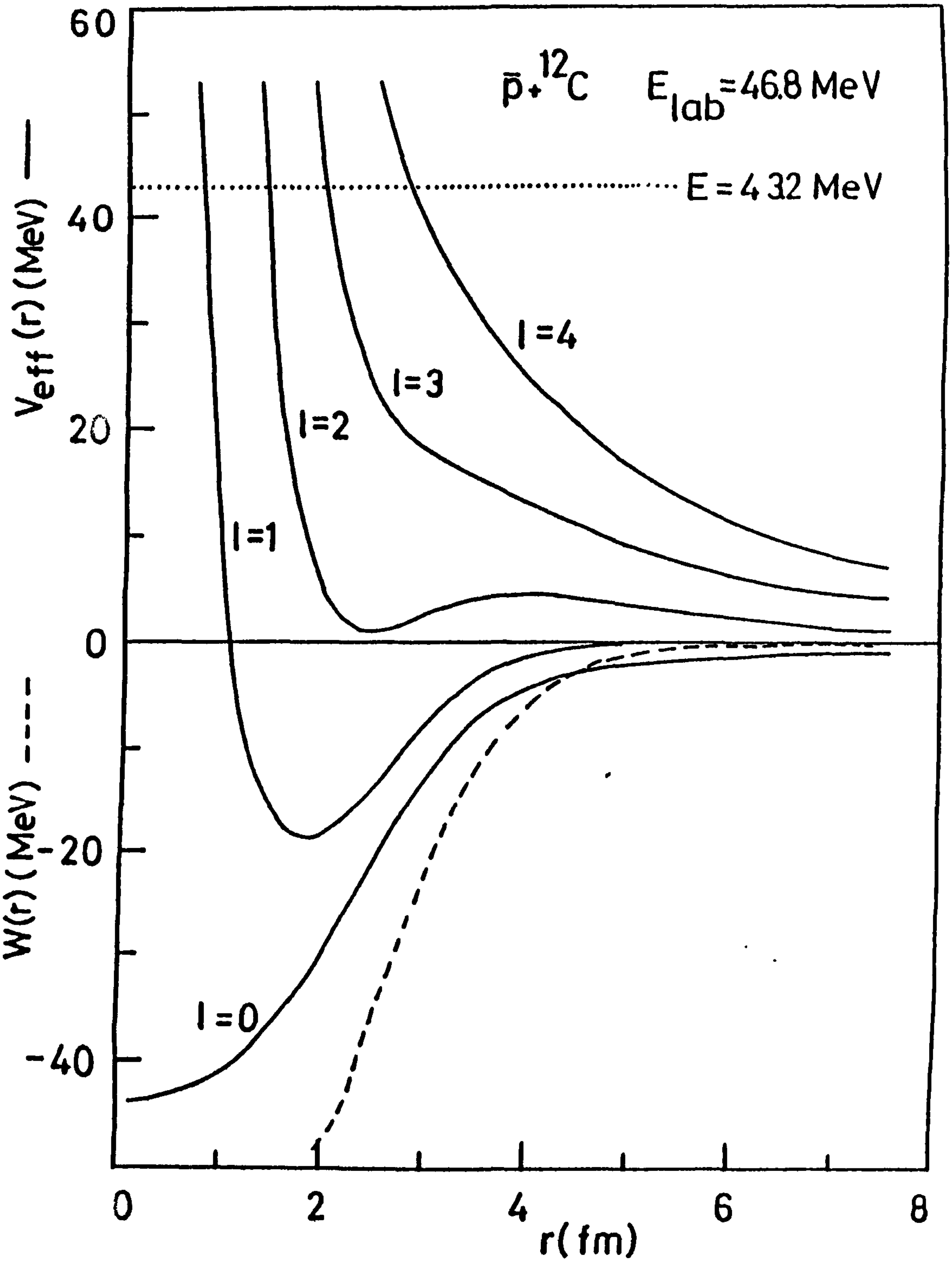

Fig.3.3.1b Same as Fig. 3.3.1a for $\bar{p}$ +^{12}C at E_{lab} = 46.8 MeV.

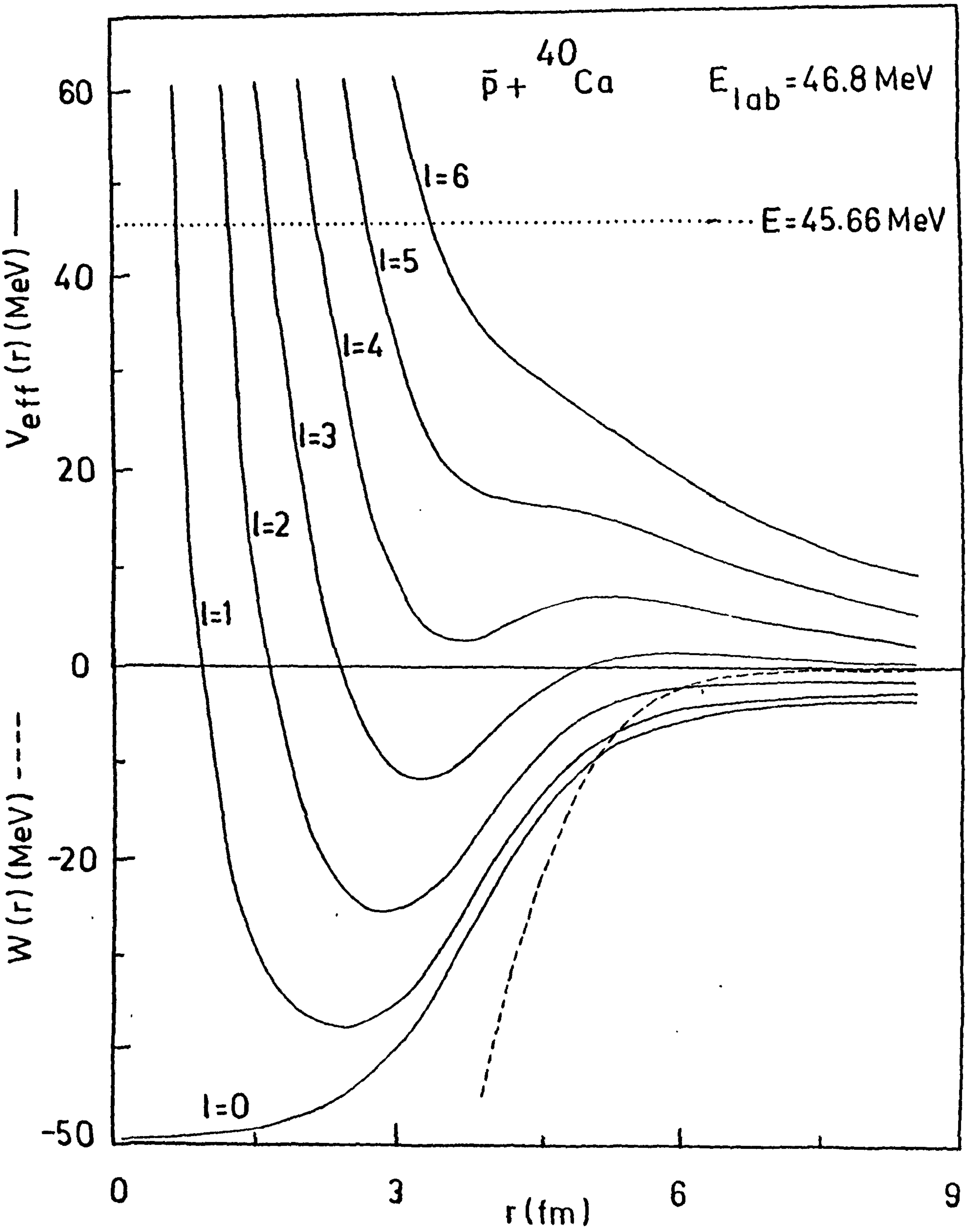

Fig.3.3.1c Same as Fig.3.3.1a for $\bar{p}$ + ^{40}Ca at E_{lab} = 46.8 MeV.

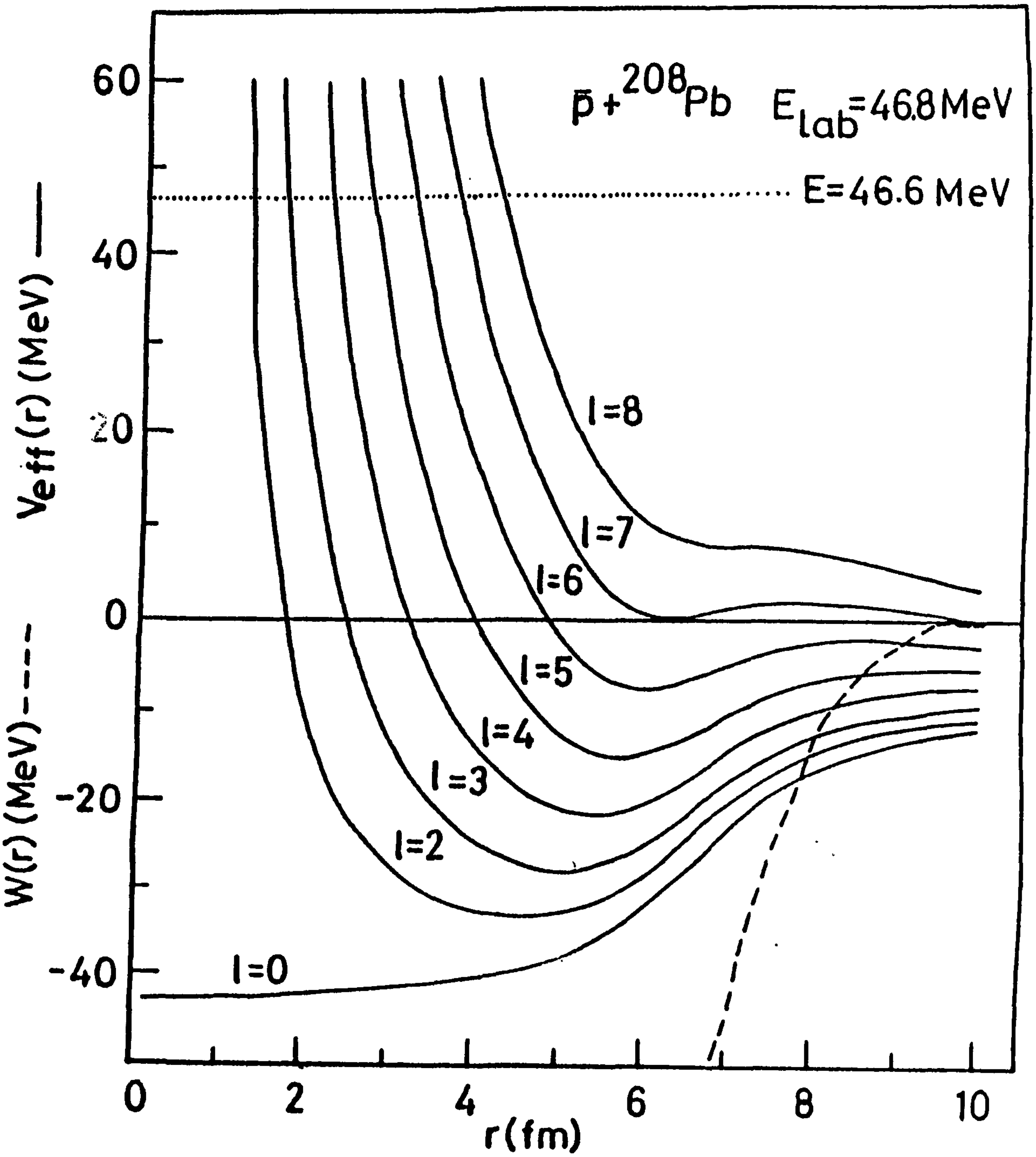

Fig.3.3.1d Same as Fig.3.3.1a for $\bar{p}$ +^{208}Pb at E_{lab} = 46.8 MeV.

partial waves it is clear that, both processes are governed by strongly absorptive imaginary part of the potential but the surface regions are not similar. In the heavy ion system for a number of partial waves it is easy to identify the interior region, barrier region and outer region. In the antiproton-nucleus system the barrier near the surface is practically absent for almost all partial waves and even when they are present, they are quite broad and shallow. The nature of the effective potential in the heavy ion scattering suggests, in general, a three-turning point WKB approach. On the other hand, in the antiproton-nucleus scattering there will be, in general, only one turning point corresponding to the interior part of the centrifugal term in the potential. However, the comparatively very smooth potential in the surface region suggests that one-turning point WKB approach may be appropriate for the analysis of the scattering cross sections. One can verify the validity of WKB approximation in both these cases by verifying the conditions of validity of the WKB approximation [Me 70] namely,

$$\lambda(r)\,|dp(r)/dr| \ll |p(r)| \qquad (3.3.4)$$

where $\lambda(r) = 2\pi/k(r)$ and $p(r) = \hbar k(r)$ are the wavelength and momentum at position r. k(r) is considered as the effective wave number. Table 3.3.2 illustrates the validity of the WKB approximation for r in the surface region for two cases only. It is clear that the ratio $\lambda(r)|dp(r)/dr|/|p(r)| \approx 10^{-2}$ is quite satisfactory for the validity of the WKB approximation. This indicates that it is quite appropriate to use WKB approximation. The condition for the validity of WKB approximation is obtained by

Table 3.3.2 Verification of WKB approximation for various values of l.

System	l	r (fm)	$\lambda(r)$ (fm)	$\lambda(r)\left\|\frac{dp(r)}{dr}\right\|$ $(\times 10^{23})$ (MeV-s/fm)	$\|p(r)\|$ $(\times 10^{21})$ (MeV-s/fm)	$\left[\lambda(r)\left\|\frac{dp(r)}{dr}\right\| / \|p(r)\|\right]$ $(\times 10^{2})$
$^{18}O + ^{58}Ni$	25	9.4	3.51	29.45	1.18	24.96
(E_{lab}= 60 MeV)	20	9.7	2.68	23.74	1.54	15.35
$\bar{p} + ^{40}Ca$	4	5.2	4.69	2.58	0.88	2.93
(E_{lab}= 46.8 MeV)	3	5.8	4.38	3.21	0.94	3.40

neglecting $k'(r)$ (i.e., $dk(r)/dr$) when compared to $k^2(r)$ in the leading order ($n = 0$) WKB approximation which results in the standard formula for phase shift that is generally used. In the antiproton-nucleus and nucleus-nucleus scatterings that we have considered, the condition $k^2(r) \gg k'(r)$, is valid in the region of interest. The effect of incorporating higher order WKB approximation has been studied by Chan et al. [Ch 81] which shows that the leading order WKB approximation is adequate for the simple parametric description of the scattering data. Another remarkable similarity between HIS and $\bar{p}$-A scattering is their reflection functions defined as the magnitude ($|S_l|$) of the partial wave S matrix. The reflection functions ($|S_l|$ vs. l) are plotted for different systems. We have compared the reflection functions corresponding to the systems $^{18}O + {}^{58}Ni$ at $E_{lab} = 60$ MeV and $\bar{p} + {}^{40}Ca$ at $E_{lab} = 46.8$ MeV which is graphically illustrated in Fig.3.3.2a. We have also displayed the variation of reflection functions with l for the systems, like $\bar{p} + {}^{12}C$ and $\bar{p} + {}^{208}Pb$ at $E_{lab} = 46.8$ MeV in Figs.3.3.2b and 3.3.2c respectively. Both processes being surface dominated phenomena, the reflection function rises quite rapidly near the grazing angular momentum. Based on these observations we have formulated in the next section analytical expressions for the nuclear phase shift using one-turning point WKB approximation and the mathematical techniques given for HIS [Sh 82].

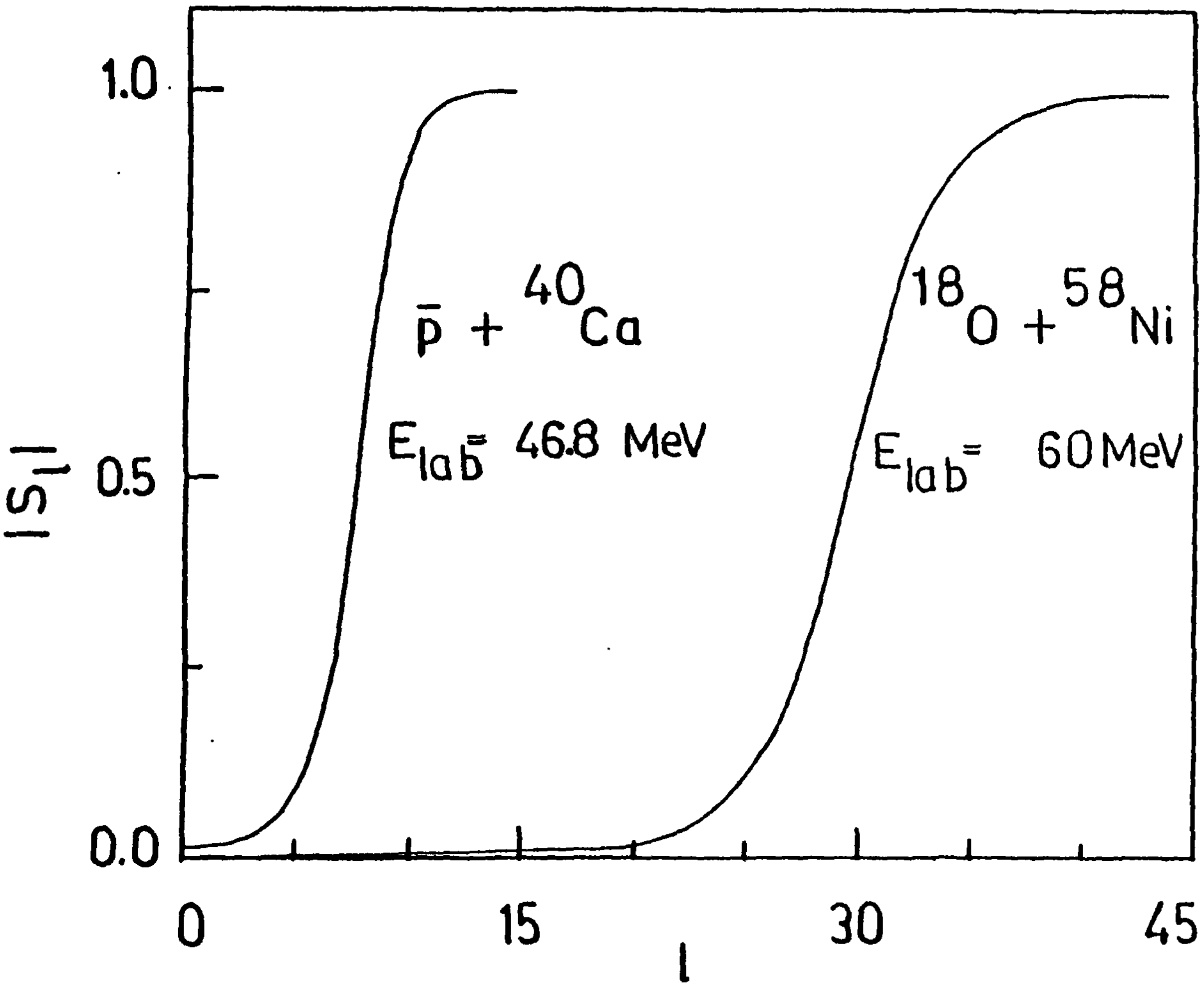

Fig.3.3.2a Comparison of reflection functions obtained from OM calculation for ${}^{18}O$ + ${}^{58}Ni$ at E_{lab} = 60 MeV and $\bar{p}$ + ${}^{40}Ca$ at E_{lab}= 46.8 MeV. Potential parameters are given in Table 3.3.1.

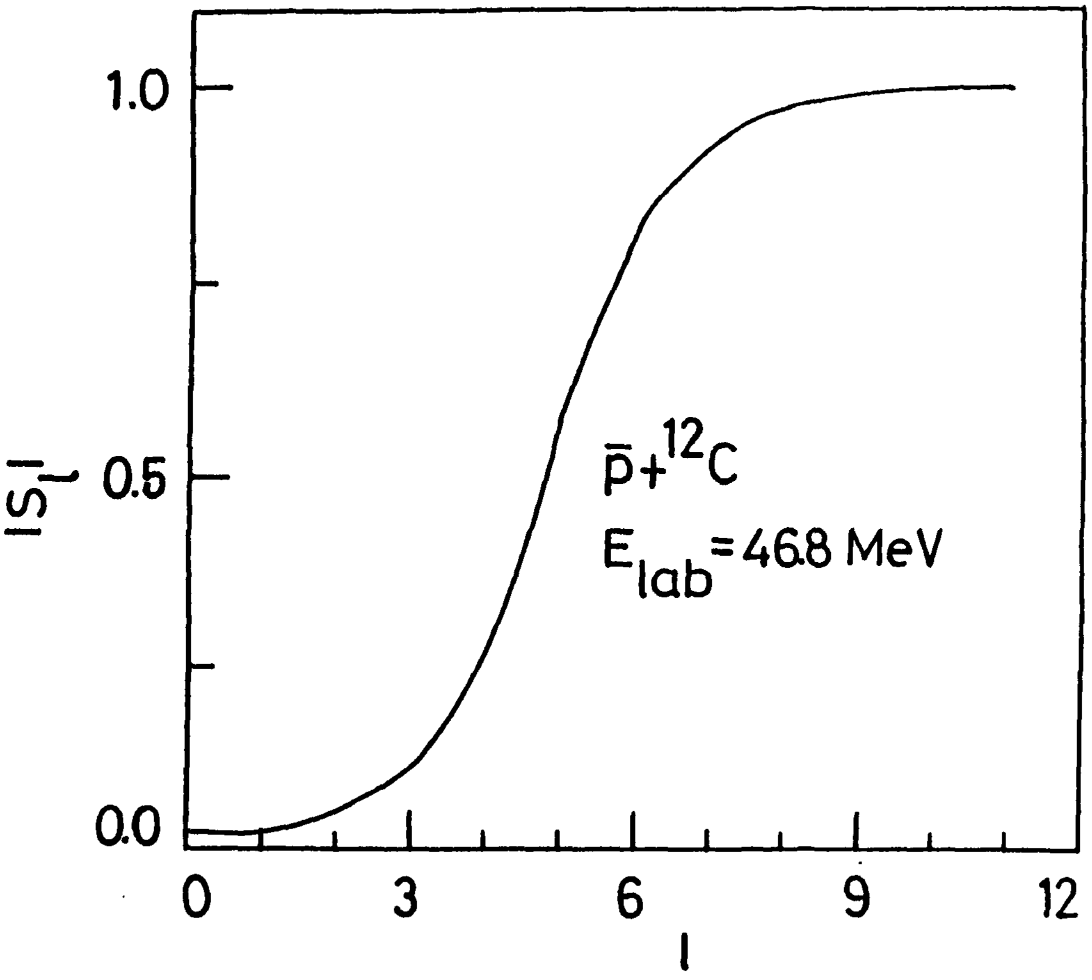

Fig.3.3.2b Plot of reflection function obtained from OM calculation for $\bar{p}$ + ^{12}C at E_{lab} = 46.8 MeV. Potential parameters are given in Table 3.3.1.

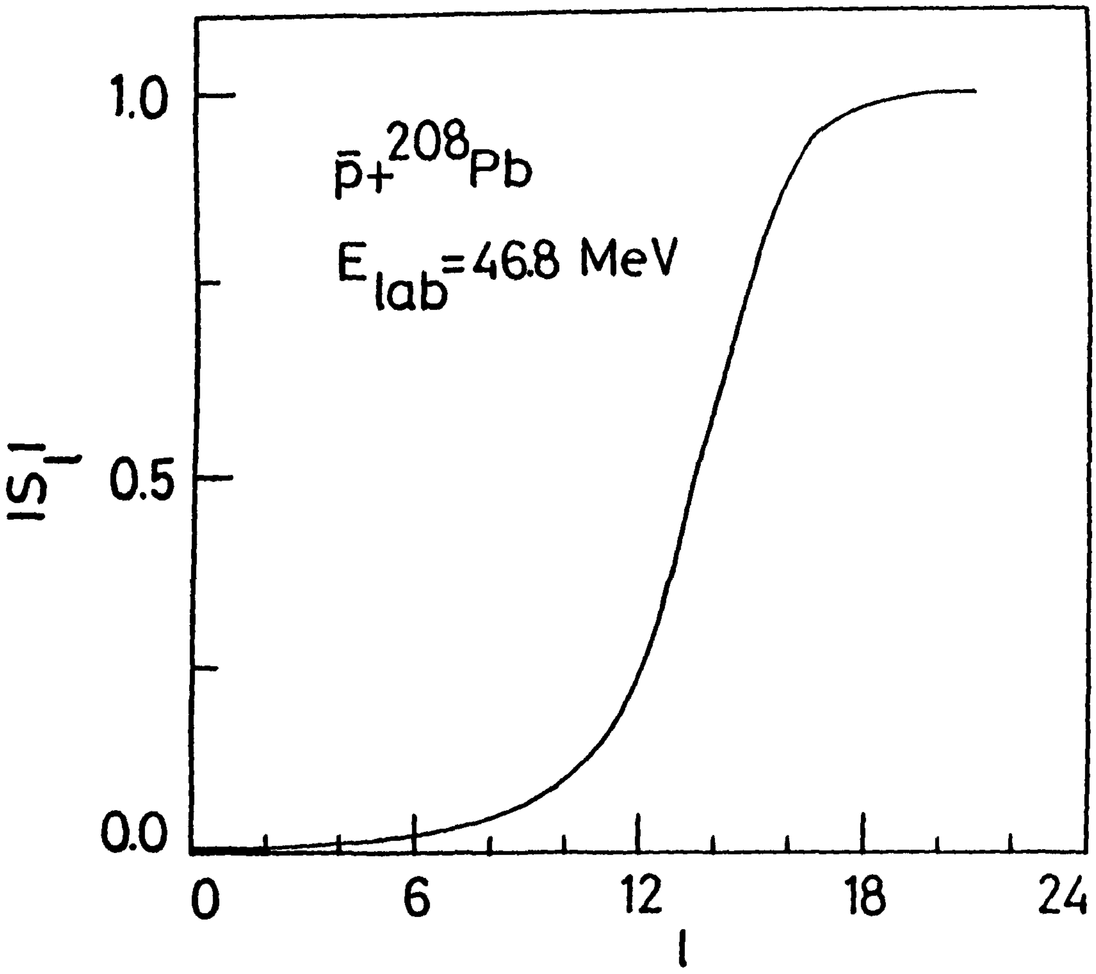

Fig.3.3.2c Same as Fig. 3.3.2b for $\bar{p}$ + ^{208}Pb at E_{lab} = 46.8 MeV. Potential parameters are listed in Table 3.3.1.

3.4 Approximate closed form expression for nuclear phase shift

In the case of heavy ion scattering semiclassical WKB method can be applied quite successfully in calculating the scattering amplitude. As we have seen in the case of $\bar{p}$-A scattering, the semiclassical WKB approximation is valid near the surface region and moreover, the real part of effective potential has in general, only one turning point. The nuclear phase shift in $\bar{p}$-A scattering can be obtained using one-turning point WKB approximation. This turning point becomes complex when complex effective potential (including the imaginary part) is used. Thus one-turning point WKB formula for nuclear phase shift (which is symbolised here as $\delta_N(\lambda)$ for convenience) is given by:

$$\delta_N(\lambda) = \lim_{R\to\infty} \left\{ \int_{r_1}^{R} \left[k^2 - V_N(r) - V_c(r) - V_\lambda(r)\right]^{1/2} dr - \int_{r_c}^{R} \left[k^2 - V_c(r) - V_\lambda(r)\right]^{1/2} dr \right\}, \qquad (3.4.1)$$

where $V_N(r) = (2\mu/\hbar^2)U_N(r)$, $V_c(r) = (2\mu/\hbar^2)U_c(r)$,

$k^2 = 2\mu E/\hbar^2$, $V_\lambda(r) = \lambda^2/r^2$ and $\lambda = l + (1/2)$.

Here E is the centre-of-mass energy. $U_N(r)$ and $U_c(r)$ are defined in Eq.(3.3.1) and Eq.(3.3.2). In Eq.(3.4.1), r_1 is the complex turning point and r_c is the Coulomb turning point which is obtained when the nuclear potential is switched off. r_c can be obtained by equating the second integrand to zero and the expression for r_c is given by

$$r_c = \left[\eta + (\eta^2 + \lambda^2)^{1/2} \right]/k , \qquad r_c \geq R_c \qquad (3.4.2)$$

$$= \left[(-x + y) / (2\eta k/R_c^3)\right]^{1/2}, \qquad r_c \le R_c$$

where $\eta = -Z_T e^2 \mu/\hbar^2 k$

$$x = \left\{ k^2 R_c - 3\eta K \right\}/R_c$$

and

$$y = \left[x^2 + 4\lambda^2 \eta k/R_c^3 \right]^{1/2}.$$

Now $\delta_N(\lambda)$ can be written in the form

$$\delta_N(\lambda) = \lim_{R \to \infty} \left\{ \int_{r_1}^{r_c} \left[k^2 - V_N(r) - V_c(r) - V_\lambda(r)\right]^{1/2} dr + \int_{r_c}^{R} \left[k^2 - V_N(r) - V_c(r) - V_\lambda(r)\right]^{1/2} dr - \int_{r_c}^{R} \left[k^2 - V_c(r) - V_\lambda(r)\right]^{1/2} dr \right\}.$$

In the region $r > r_c$, $\left[k^2 - V_N(r) - V_c(r) - V_\lambda(r) \right]^{1/2}$ can be expanded in powers of $V_N(r)$ and hence we get

$$\delta_N(\lambda) = \lim_{R \to \infty} \left\{ \int_{r_1}^{r_c} \left[k^2 - V_N(r) - V_c(r) - V_\lambda(r)\right]^{1/2} dr + \int_{r_c}^{R} \left[k^2 - V_c(r) - V_\lambda(r)\right]^{1/2} dr \right.$$

$$\left. -(1/2) \int_{r_c}^{R} V_N(r) \left[k^2 - V_c(r) - V_\lambda(r)\right]^{-1/2} dr - \int_{r_c}^{R} \left[k^2 - V_c(r) - V_\lambda(r)\right]^{1/2} dr \right\}$$

$$= -(1/2) \int_{r_c}^{\infty} V_N(r) \left[k^2 - V_c(r) - V_\lambda(r)\right]^{-1/2} dr$$

$$+ \int_{r_1}^{r_c} \left[k^2 - V_c(r) - V_\lambda(r) - V_N(r)\right]^{1/2} dr$$

$$= \delta_N^{(1)}(\lambda) + \delta_N^{(2)}(\lambda) \,. \qquad (3.4.2)$$

Thus $\delta_N^{(1)}(\lambda)$ and $\delta_N^{(2)}(\lambda)$ give the contributions to $\delta_N(\lambda)$ in the region r_c to ∞ and r_1 to r_c respectively. The first integral can be evaluated as follows. In the region $r \quad R_r, R_1$, $U_N(r)$ can be approximated as

$$U_N(r) = V_0 \sum_{n=0}^{\infty} \left[- \exp\left(\frac{R_r - r}{a_r}\right)\right]^{n+1}$$

$$+ iW_0 \sum_{n=0}^{\infty} \left[- \exp\left(\frac{R_1 - r}{a_1}\right)\right]^{n+1} .$$

$$r \quad R_r, R_1$$

Thus the integral corresponding to $\delta_N^{(1)}(\lambda)$ reduces to

$$\delta_N^{(1)}(\lambda) = (-2\mu/\hbar^2) \frac{1}{2} \left\{ V_0 \sum_{n=0}^{\infty} \int_{r_c}^{\infty} \left[- \exp\left(\frac{R_r - r}{a_r}\right)\right]^{n+1} \times (r/k)\left(r^2 - 2\eta r/k - \lambda^2/k^2\right)^{-1/2} dr \right.$$

$$\left. + iW_0 \sum_{n=0}^{\infty} \int_{r_c}^{\infty} \left[- \exp\left(\frac{R_1 - r}{a_1}\right)\right]^{n+1} \times (r/k)\left[r^2 - 2\eta r/k - \lambda^2/k^2\right]^{-1/2} dr \right\}.$$

Thus the integral corresponding to Re $\delta_N(\lambda)$ is

$$\mathrm{Re}\delta_N^{(1)}(\lambda) = (-2\mu V_0/\hbar^2)\ \frac{1}{2k}\left[\sum_{n=0}^{\infty}\int_{r_c}^{\infty}\left(-\exp\left(\frac{R_r - r}{a_r}\right)\right)^{n+1} \times \right.$$
$$\left. r\left(r^2 - 2\eta r/k - \lambda^2/k^2\right)^{-1/2} dr\right. .$$

Using the table of integral transforms [Er 53, Er 54] and other relevant formulae [Sh 82], the expression for Re $\delta_N^{(1)}(\lambda)$ becomes

$$\mathrm{Re}\ \delta_N^{(1)}(\lambda) = -(2\mu V_0/\hbar^2)\ \frac{1}{2k^2}\left\{\sum_{n=0}^{\infty}\left[-\exp\left(\frac{-\eta + kR_r}{ka_r}\right)\right]^{n+1} \times \right.$$

$$\left[\eta\ K_0\left(\frac{n+1}{ka_r}\left(\lambda^2+\eta^2\right)^{1/2}\right) + \left(\lambda^2+\eta^2\right)^{1/2} \times\right.$$

$$\left.\left. K_1\left(\frac{n+1}{ka_r}\ \left(\lambda^2+\eta^2\right)^{1/2}\right)\right]\right\}, \qquad (3.4.4)$$

where K_i is the K-type modified Bessel function [Ab 64]. A similar expression for $\mathrm{Im}\delta_N^{(1)}(\lambda)$ can be written by replacing the parameters of the real potential with the corresponding parameters of the imaginary potential. If one apporoximates the complex turning point r_1 by $r_1^{(1)}$ (the first iteration value of r_1) given by

$$r_1^{(1)} = r_c - f(r_c)/f'(r_c) \quad , \qquad (3.4.5)$$

where $f(r) = r^2 - \dfrac{2\eta}{k}\, r - \dfrac{\lambda^2}{k^2} - \dfrac{r^2}{k^2}\, V_N(r)$ and $f'(r_c)$ it's derivative at $r = r_c$, one can get a reasonable expression to

$\delta_N^{(2)}(\lambda)$ given by

$$\delta_N^{(2)}(\lambda) = \frac{1}{2} r_c^3 \frac{\left[-V_N(r_c)\right]^{3/2}}{\left[k^2r^2+ \lambda^2 - \varepsilon\right]} , \qquad (3.4.6)$$

where $\varepsilon = r_c\left[\frac{d}{dr} (r^2V_N(r))\Big|_{r=r_c}\right]$.

It may be pointed out that in this approach it is not essential to calculate the exact turning point. However, if one computes the exact turning point, the expression for $\delta_N^{(2)}(\lambda)$ in the linear approximation becomes

$$\delta_N^{(2)}(\lambda) = \frac{1}{2} (r_c - r_1) \left[-V_N(r_c)\right]^{1/2} \qquad (3.4.7)$$

The exact turning point is calculated by carrying out Newton-Raphson method of iteration [Sc 66] till the saturation is reached. We have found that 4 to 5 iterations are adequate to get the exact turning point. For real potential, the turning point separates the classically allowed region from the forbidden region. Generalisation of this to complex potentials has been used in the study of HIS [Br 85]. In Figs. 3.4.1a and 3.4.1b, we have plotted the real and imaginary parts of the complex turning points r_1 and $r_1^{(1)}$ for a number of partial waves for $\bar{p}$ + ^{12}C at E_{lab} = 46.8 MeV. The corresponding results for $\bar{p}$ + ^{40}Ca at E_{lab} = 46.8 MeV are shown in Figs. 3.4.2a and 3.4.2b. The Figs.3.4.1a and 3.4.2a also include the Coulomb turning point r_c for the respective systems. These figures indicate that for most of the

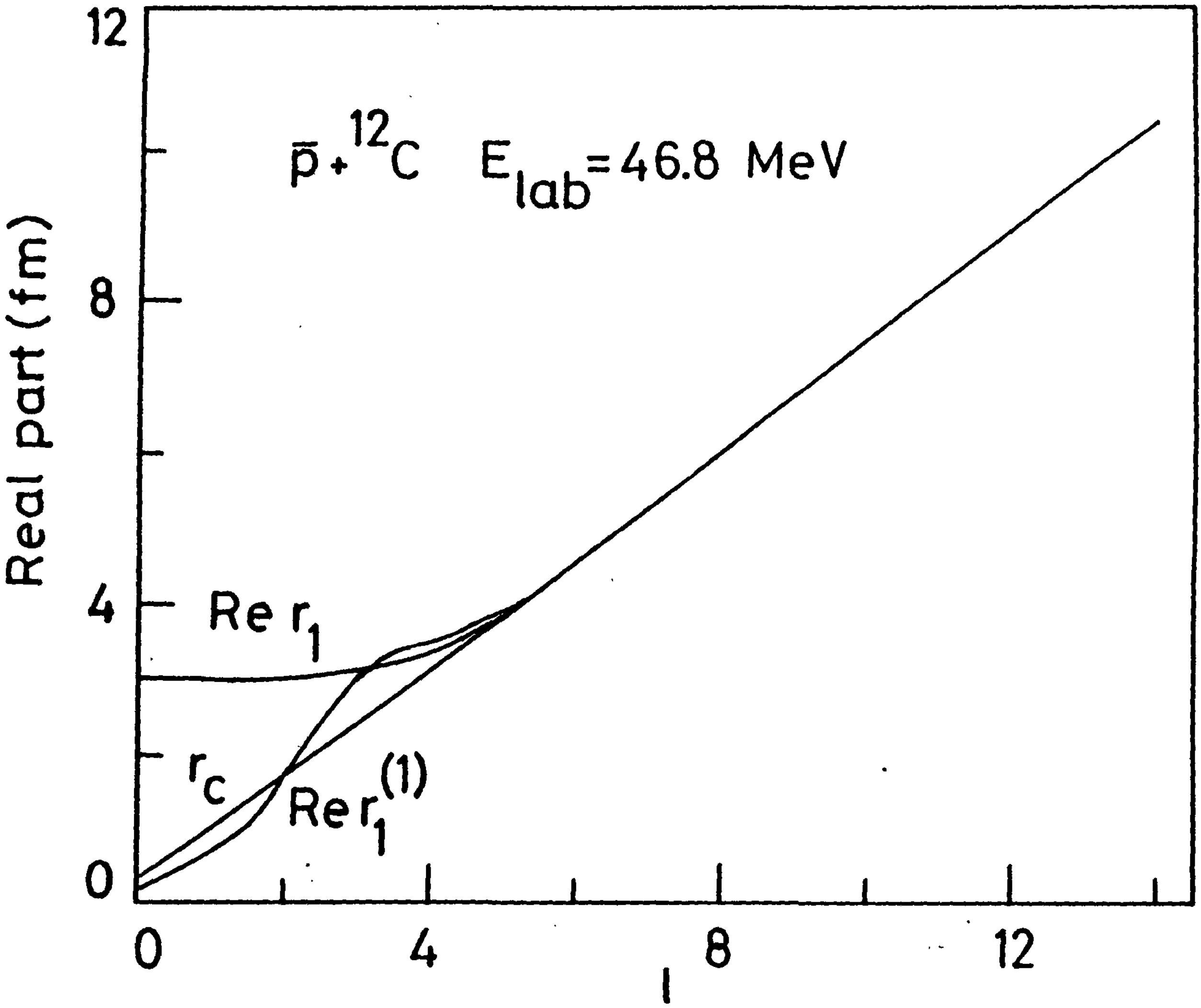

Fig.3.4.1a Variation of the turning points r_l, $r_l^{(1)}$ and r_c as a function of l for $\bar{p}$ + ^{12}C at E_{lab} = 46.8 MeV with the potential parameters given in Table 3.3.1.

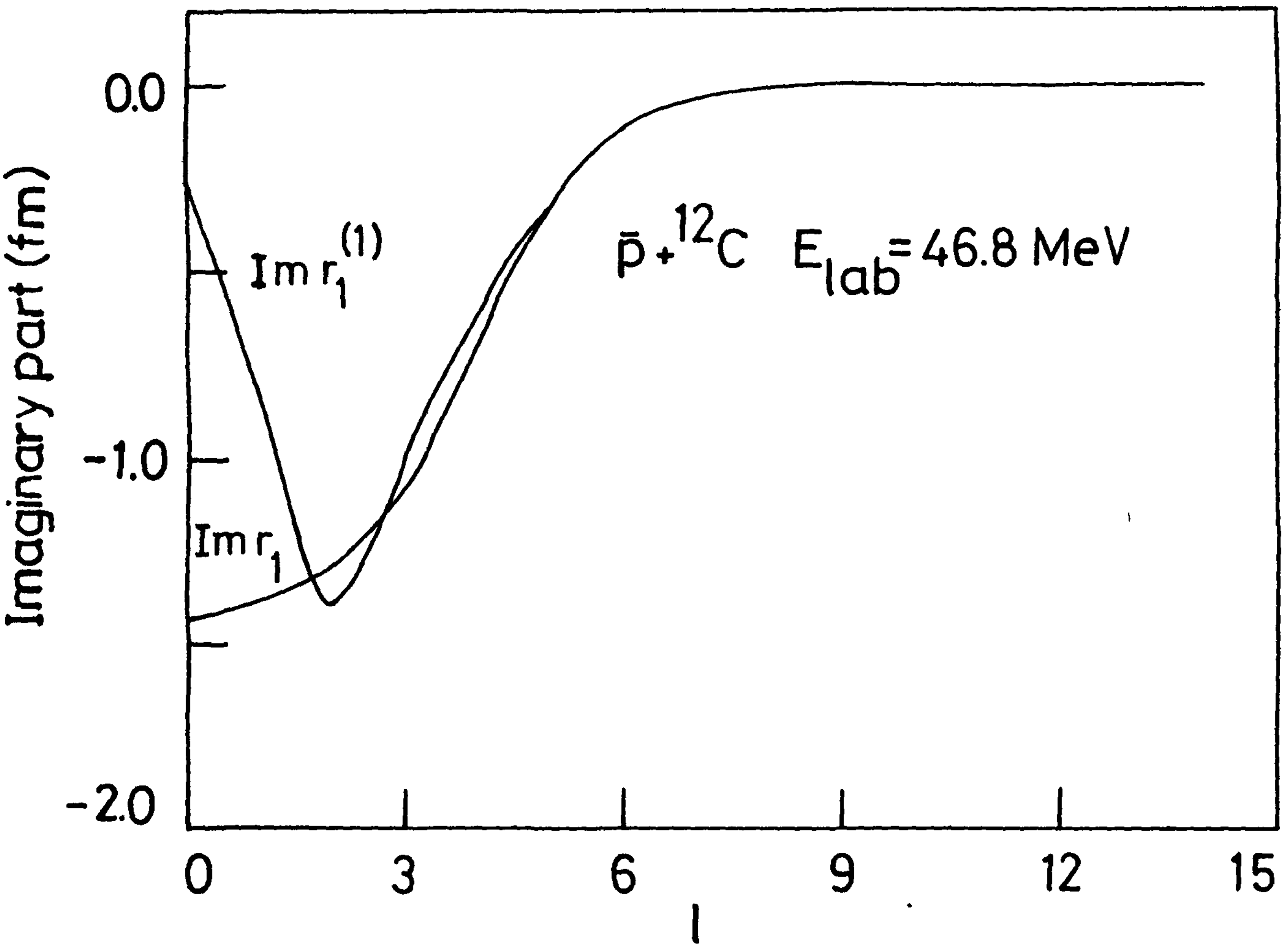

Fig.3.4.1b Variation of the imaginary part of the complex turning points r_1 and $r_1^{(1)}$ as a function of l for $\bar{p}$ + ${}^{12}C$ at $E_{lab}=46.8$ MeV.

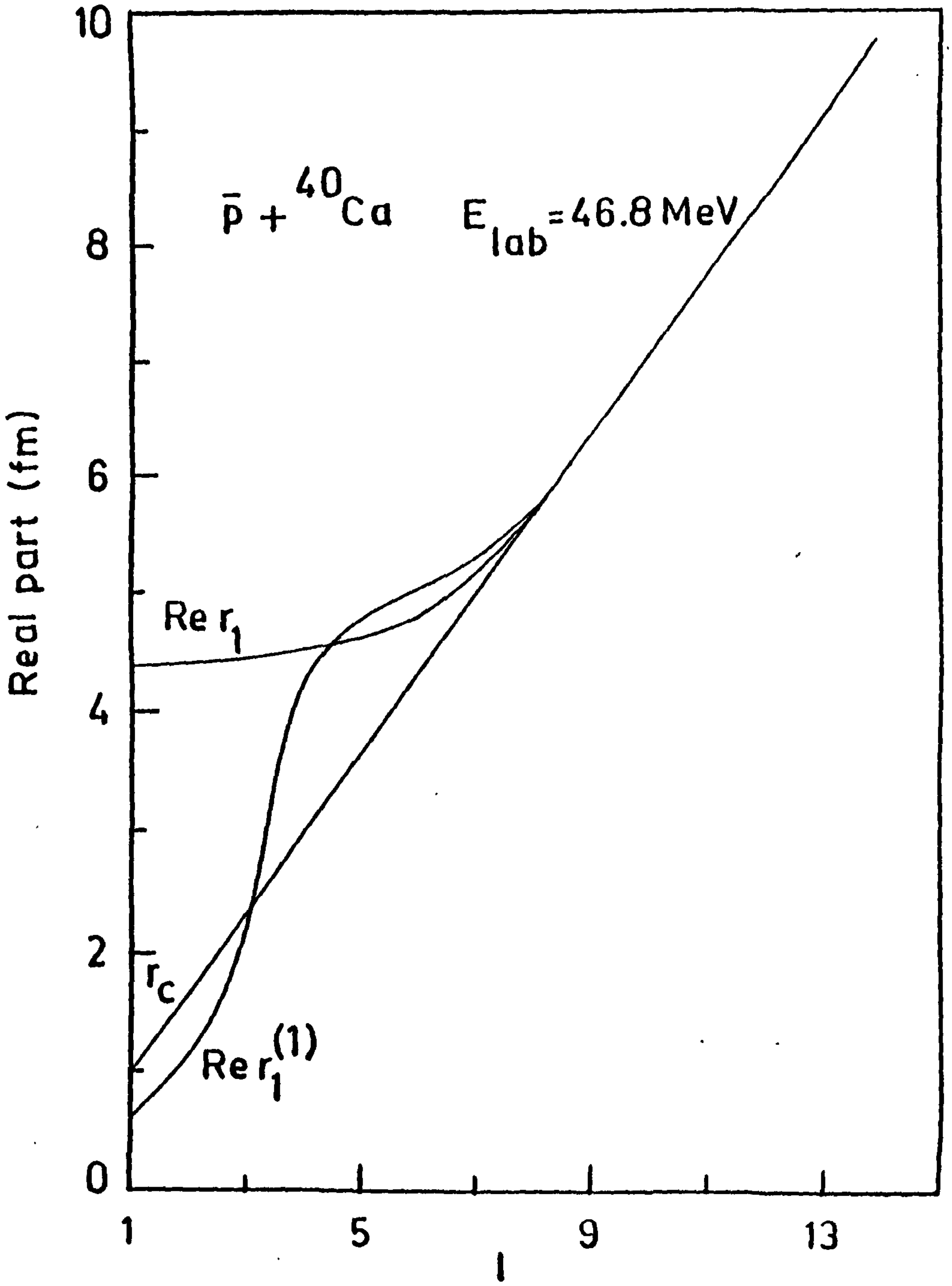

Fig.3.4.2a Same as Fig.3.4.1a for $\bar{p}$ + ^{40}Ca at E_{lab}=46.8 MeV. Potential parameters are given in Table 3.3.1.

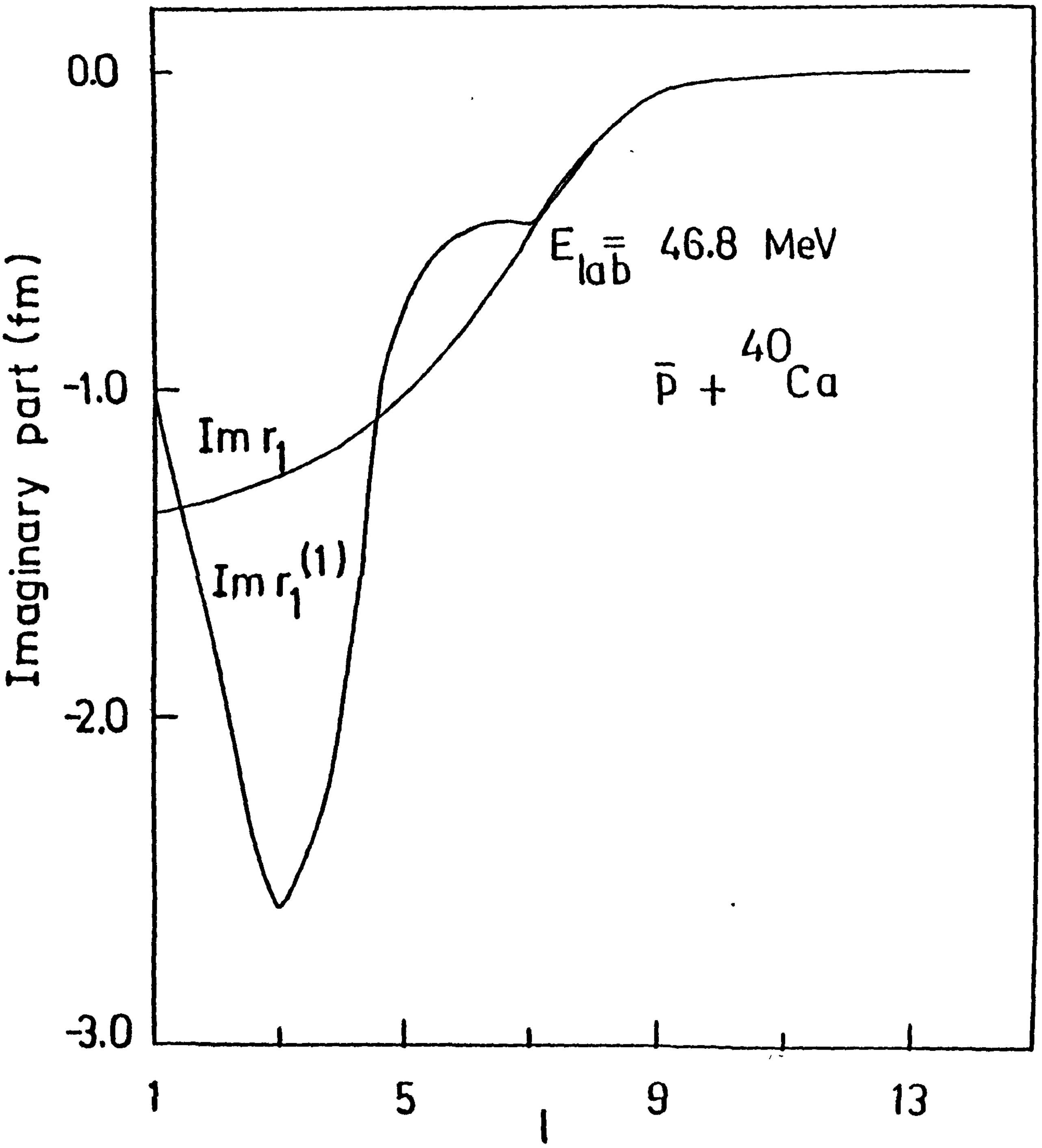

Fig 3.4.2b Same as Fig.3.4.1b for $\bar{p}$ + ^{40}Ca at E_{lab}=46.8 MeV.

partial waves, except for a few, $r_1^{(1)}$ is quite a good approximation to r_1. The turning points obtained in the interior region by first iteration are not close to the exact turning point. But the smaller partial waves are highly absorptive in nature ($|S_l| \approx 0$), as can be seen from the graphs corresponding to reflection functions, and the scattering data are not very sensitive to the potential in the interior region. Hence some error in the calculation of the turning point does not significantly affect the cross sections as far as the partial waves which are more or less fully absorbed are concerned. We use the expressions given above for $\delta_N^{(1)}(\lambda)$ and $\delta_N^{(2)}(\lambda)$ to compute the nuclear phase shift. Since the arguments of the functions K_0 and K_1 appreaing in Eq. (3.4.4) are generally large we can approximate K_0 and K_1 by their asymptotic expansions which are given by Abramowitz and Stegun [Ab 64]:

$$K_0(x) = x^{-1/2}\exp(-x)\sum_{n=0}^{6} a_n (2/x)^n + \varepsilon_1 \quad , \quad |\varepsilon_1| \quad 1.9 \times 10^{-7}$$

$$K_1(x) = x^{-1/2}\exp(-x)\sum_{n=0}^{6} b_n (2/x)^n + \varepsilon_2 \quad , \quad |\varepsilon_2| \quad 2.2 \times 10^{-7}$$

One may note that the formula developed can be readily used to compute the antiproton-nucleus scattering to fit the cross section data by suitably varying the parameters. This approach is similar to the closed formalism develpoed by Frahn and Rehm [Fr 78].

3.5 Parametric S matrix approach to antiproton-nucleus scattering

The closed formalism approach or more conveniently the parameteric S matrix approach has attained great success in the study of HIS. In this approach it is possible to study HIS data without going into the details of optical model potential parameters. In the parametric S matrix approach one parametrises the nuclear S matrix ($S_N(\lambda)$) or the reflection function ($\eta(\lambda) = |S_N(\lambda)|$) and the real part of the phase shift (Re $\delta_N(\lambda)$) simultaneously in terms of several parameters which are adjusted to fit the scattering data. Whatever the method of parametrisation of S matrix may be, it is rather a quite simple and useful tool for the analysis of HIS data. The parameters of parametric S matrix approach are related to the physical quantities like grazing angular momentum on one hand and can be related to the potential parameters on the other hand. The correlation of the parameters of parametric S matrix approach and the conventional optical model potential parameters has also been established [Ga 84a, Sh 92]. The antiproton-nuclues scattering which is of current interest has close similarity with HIS and moreover, semiclassical approach like WKB approximation is found to be valid in the case of antiproton-nucleus scattering also. Thus, many well formulated techniques which are applicable to HIS can be fruitfully adopted in the analysis of antiproton-nucleus scattering data. We have used well known parametrisation schemes of S matrix, to analyse antiproton-nucleus scattering data. Two of the commonly used parametrisation of nuclear S matrix are:

(1) Ericson parametrisation and (2) McIntyre parametrisation. In the Ericson parametrisation nuclear S matrix $S_N(\lambda)$ for l^{th} partial wave is represented as follows [Ma 78]:

$$S_N(\lambda) = \left[1 + \exp \left(\frac{\Lambda - \lambda}{\Delta} \right) \right]^{-1}, \qquad (3.5.1)$$

where Λ (complex) and Δ are the Ericson parameters and $\lambda = l + 1/2$. In this parametrisation there are three real parameters namely, Δ, Re Λ and Im Λ. The expression for $S_N(\lambda)$ in the McIntyre parametrisation [Fr 78, Mc 60, Me 85] is given by

$$S_N(\lambda) = \eta(\lambda) \exp(2i \operatorname{Re} \delta_N(\lambda)), \qquad (3.5.2)$$

where $$\eta(\lambda) = |S_N(\lambda)| = \left[1 + \exp \left(\frac{\Lambda - \lambda}{\Delta} \right) \right]^{-1} \qquad (3.5.3)$$

and $$\operatorname{Re} \delta_N(\lambda) = \delta_o (1 - \eta_p(\lambda)). \qquad (3.5.4)$$

The form of $\eta_p(\lambda)$ is similar to that of $\eta(\lambda)$ with the parameters Λ_p and Δ_p. Λ and Δ are the McIntyre parameters for the reflection function ($|S_N(\lambda)|$) and δ_o, Λ_p and Δ_p are the McIntyre parameters for the phase shift. This parametrisation is widely applied in the analysis of HIS. It may be mentioned that, in the conventional optical model also, the total potential is generally parametrised in terms of 5-7 parameters including the Coulomb radius parameter r_c'. It is to be noted that, in the parametric S matrix approach adopted here, we restrict the parametrisation of $S_N(\lambda)$ to 3 or 5 parameters. In the next section we have demonstrated our results of calculation for $\bar{p}$-nucleus scattering systems within the framework of closed formalism using both Ericson and McIntyre parametrisations.

3.6 Results and discussion

In order to demonstrate the usefulness of WKB technique in analysing $\bar{p}$-A scattering we have studied two typical cases namely, $\bar{p} + {}^{12}C$ and $\bar{p} + {}^{40}Ca$ at $E_{lab} = 46.8$ MeV for which cross sections have been measured and optical model fits have been obtained. In Fig. 3.6.1 we have shown the reflection functions of both the systems obtained by optical model fits and compared them with those obtained by WKB approximation using both the approximate expression for WKB turning point and numerically evaluated turning point. This indicates fairly good agreement with the reflection functions obtained using the optical model calculation for both $\bar{p} + {}^{12}C$ and $\bar{p} + {}^{40}Ca$ systems. The ratio of differential scattering cross section to the Rutherford cross section $(\sigma(\theta)/\sigma_R(\theta))$ for $\bar{p} + {}^{12}C$ and $\bar{p} + {}^{40}Ca$ are shown in Fig. 3.6.2 and Fig.3.6.3 where we have plotted the cross sections obtained by using optical model calculation and the cross sections generated by one-turning point WKB approximation. In Figs.3.6.2 and 3.6.3 the solid curve (——) corresponds to the optical model result and dash-dot-dashed curve (— · —) and dash-cross-dashed (— × —) curves are the results obtained using exact turning point and the first iteration value of r_1 respectively. As the cross sections based on optical model give fairly good fit to the experimental data the optical model prediction can be taken as to represent the experimental data.

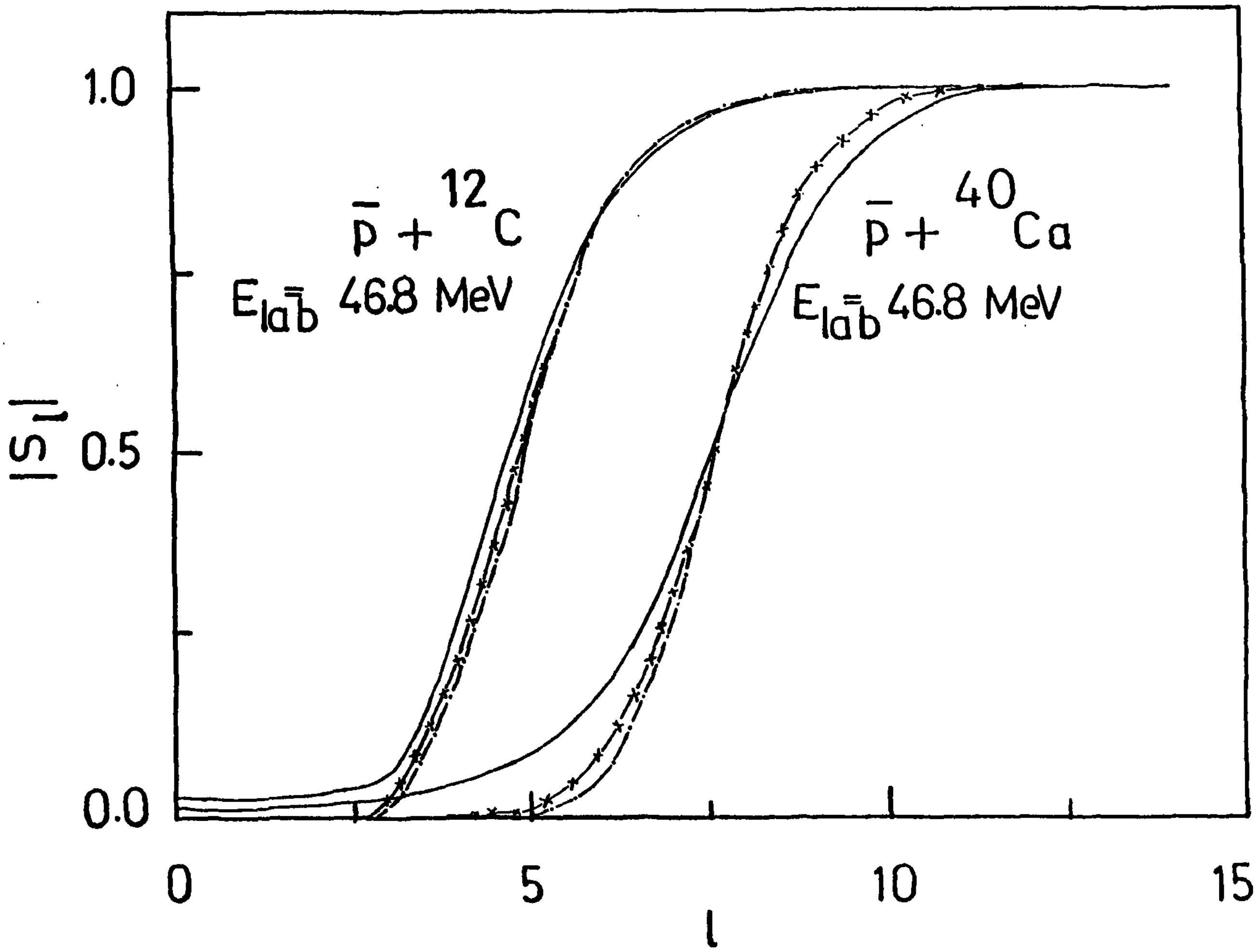

Fig.3.6.1 Reflection functions for $\bar{p}$ + ^{12}C and $\bar{p}$ + ^{40}Ca obtained using the exact OM calculation (——) and those obtained by using $\delta_N(\lambda)=\delta_N^{(1)}(\lambda)+\delta_N^{(2)}(\lambda)$ with $\delta_N^{(2)}(\lambda)= 0.5(r_c-r_1^{(1)})(-V_N(r_c))^{1/2}$ (— x —), and using $\delta_N(\lambda) = \delta_N^{(1)}(\lambda) + \delta_N^{(2)}(\lambda)$ where $\delta_N^{(2)}(\lambda)$ is given by Eq.(3.4.7) (—·—). Potential parameters are given in Table 3.3.1.

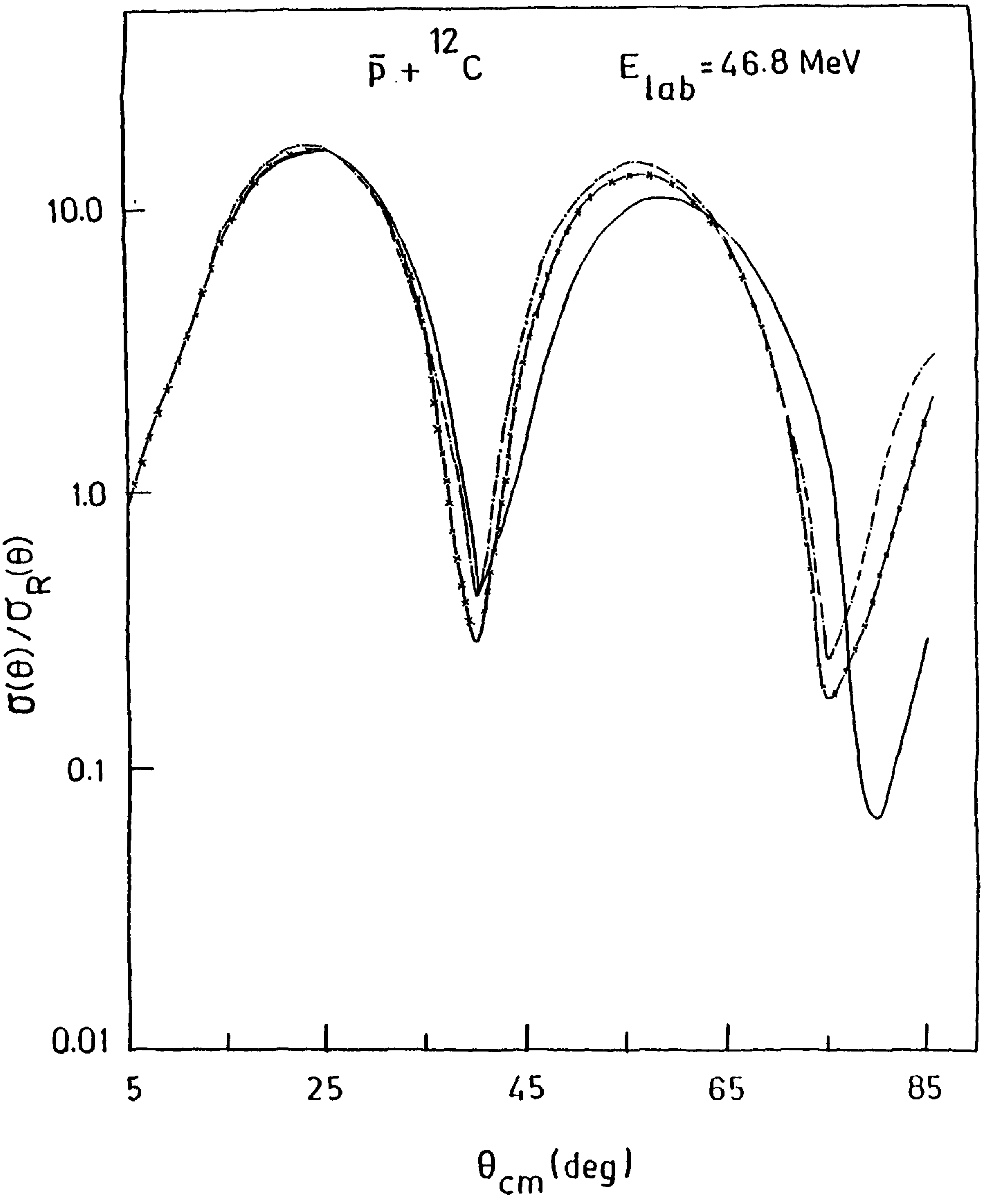

Fig.3.6.2 $\sigma(\theta)/\sigma_R(\theta)$ as a function of angle (in the centre of mass system) for $\bar{p} + {}^{12}C$ at E_{lab}=46.8 MeV obtained by using OM calculation (—) and those obtained by using $\delta_N(\lambda) = \delta_N^{(1)}(\lambda) + \delta_N^{(2)}(\lambda)$ with $\delta_N^{(2)}(\lambda) = 0.5(r_c - r_1^{(1)})(-V_n(r_c))^{1/2}$ (— x —), and using $\delta_N(\lambda) = \delta_N^{(1)}(\lambda) + \delta_N^{(2)}(\lambda)$ where $\delta_N^{(2)}(\lambda)$ is given by Eq.(3.4.7) (—·—).

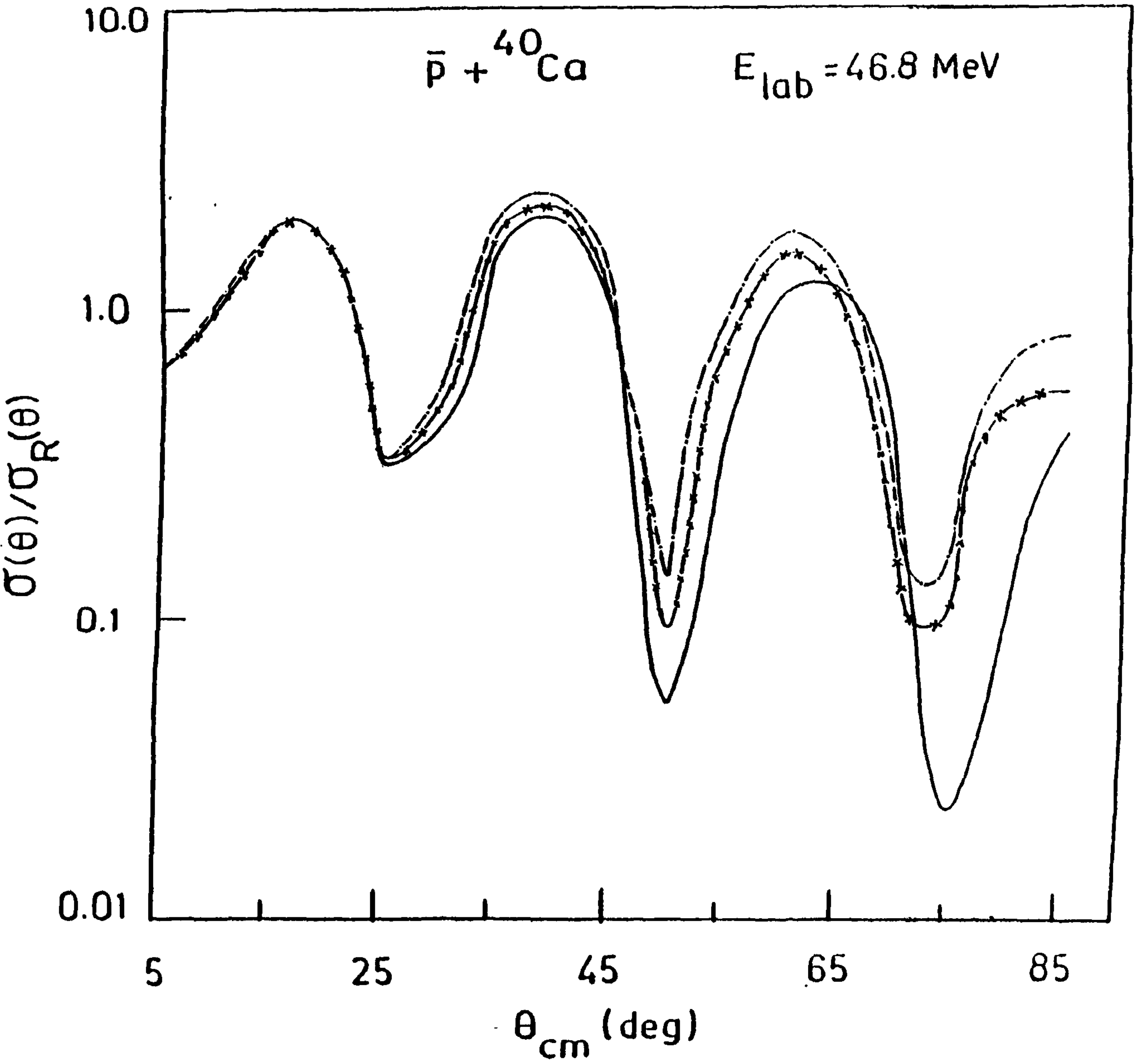

Fig.3.6.3 Same as Fig.3.6.2. for $\bar{p}$ + ^{40}Ca at E_{lab} = 46.8 MeV

Thus, in Fig. 3.6.2 and Fig. 3.6.3 the cross sections generated by the one-turning point WKB approximation have been compared with the optical model predictions. Our result shows that the WKB approach is useful to describe the essential features of cross sections. Thus, the semiclassical WKB approach is fairly suitable for $\bar{p}$-A scattering and hence. can be adopted to analyse the antiproton-nucleus scattering amplitude and scattering cross sections in the same way as one does in HIS. The primary difference, however, is that in $\bar{p}$-A scattering, one-turning point WKB formula is reasonably adequate and the number of partial waves involved is small as compared to that in HIS.

The cross sections for $\bar{p}$ + ^{12}C, $\bar{p}$ + ^{40}Ca and $\bar{p}$ + ^{208}Pb at E_{lab} = 46.8 MeV and $\bar{p}$ + ^{12}C at E_{lab} = 180 MeV have also been analysed within the framework of closed formalism, using both Ericson and McIntyre parametrisations. Typical sets of optical model (OM) potential parameters which are used to describe $\bar{p}$-A cross sections are listed in Table 3.6.1. The parameters of Ericson and McIntyre parametrisations are listed in Table 3.6.2 and Table 3.6.3 respectively which generate the reflection functions and cross sections similar to that obtained using optical model calculation. The parameter Λ in both cases corresponds to the partial wave for which the reflection function is close to 0.5. The parameter Δ is a measure of variation of the reflection function from the region of full absorption ($|S_N(\lambda)|$ = 0) to the case of no absorption ($|S_N(\lambda)|$ = 1). Some typical results for $|S_N(\lambda)|$ and differential cross section ($d\sigma/d\Omega$) obtained using some typical sets of parameters are shown in

Table 3.6.1 Optical model potential parameters for different systems.

System	$\bar{p} + {}^{12}C$	$\bar{p} + {}^{12}C$	$\bar{p} + {}^{40}Ca$	$\bar{p} + {}^{208}Pb$	${}^{18}O + {}^{62}Ni$
E_{lab}(MeV)	180	46.8	46.8	46.8	63
V_0(MeV)	20.0	140.0	40.0	20.0	70.0
r_r(fm)	1.35	0.421	1.1	1.1	1.09
a_r(fm)	0.44	0.743	0.6	0.65	0.766
W_0(MeV)	113.0	120.9	100.0	140.0	9.0
r_i(fm)	1.1	0.928	1.1	1.1	1.351
a_i(fm)	0.5	0.636	0.6	0.65	0.529
r'_c(fm)	1.3	1.3	1.3	1.3	1.25
Ref.	[He 85]	[Ku 85]	[He 85]	[He 85]	[Fr 78]

Table 3.6.2 Ericson parameters for different $\bar{p}$-A systems obtained to fit the elastic scattering data.

System	E_{lab} (MeV)	ReΛ	ImΛ	Δ	Expt.data at (MeV)	Remarks
$\bar{p} + {}^{12}C$	180	8.908	0.263	1.264	179.7[a]	Figs.3.6.4a and 3.6.5a
$\bar{p} + {}^{12}C$	46.8	5.383	0.171	0.761	46.8[a]	Figs.3.6.4b and 3.6.5b
$\bar{p} + {}^{40}Ca$	46.8	8.203	0.422	0.797	47.8[a]	Figs.3.6.4c and 3.6.5c
$\bar{p} + {}^{208}Pb$	46.8	13.820	1.478	1.396	48.3[a]	Figs.3.6.4d and 3.6.5d

a : [Ja 86]

Table 3.6.3 McIntyre parameters for different $\bar{p}$-A systems obtained to fit the elastic scattering data.

System	E_{lab} (MeV)	Λ	Δ	δ_o (radian)	Λ_P	Δ_P	Remarks
$\bar{p} + {}^{12}C$	180	8.902	1.254	2.6	−0.64	1.697	Figs.3.6.4a and 3.6.5a
$\bar{p} + {}^{12}C$	46.8	5.246	0.982	2.25	−12.3	4.5	Figs.3.6.4b and 3.6.5b
$\bar{p} + {}^{40}Ca$	46.8	7.974	0.987	0.75	0.5	1.45	Figs.3.6.4c and 3.6.5c
$\bar{p} + {}^{208}Pb$	46.8	13.980	1.301	−0.735	12.733	1.174	Figs.3.6.4d and 3.6.5d

Figs.3.6.4a - 3.6.4d and Figs. 3.6.5a - 3.6.5d.

In Figs.3.6.4a - 3.6.4d we have compared the reflection function obtained using Ericson (—•—) and McIntyre (— x —) parametrisations together with that obtained by using optical model (——) calculation for the systems $\bar{p}$ + ^{12}C at E_{lab} = 180 MeV and $\bar{p}$ + ^{12}C, $\bar{p}$ + ^{40}Ca and $\bar{p}$ + ^{208}Pb at E_{lab} = 46.8 MeV respectively. In Figs. 3.6.5a-3.6.5d we have illustrated typical cases of differential cross section, for the above mentioned $\bar{p}$-A systems respectively, obtained using closed formalism along with that of the conventional optical model calculation. These indicate that closed formalism provides a simple procedure for the analysis of antiproton-nucleus scattering data. For comparison we have shown the results of closed formalism using McIntyre parametrisation for a typical case of HIS namely, ^{18}O + ^{62}Ni at E_{lab} = 63 MeV obtained by Frahn and Renm [Fr 78]. The reflection functions $|S_N(\lambda)|$ obtained using optical model (——) and closed formalism (.....) calculations are displayed in Fig.3.6.6. The best fitted cross section ($\sigma(\theta)/\sigma_R(\theta)$) curve represented by the solid curve (——) is also shown in Fig. 3.6.7 and the dashed curve (----) in the figure corresponds to δ_0 = 0. The McIntyre parameters which fit the HIS curve best are also listed in Table 3.6.4. The optical model potential parameters for this system used in the calculation [Fr 78] is also contained in Table 3.6.1. A list of parameters of McIntyre type of parametrisation for elastic and inelastic scattering for a number of heavy ion systems is given by Frahn and Rehn [Fr 78]. These analyses show that both these parametrisations of S matrix developed for the analysis of

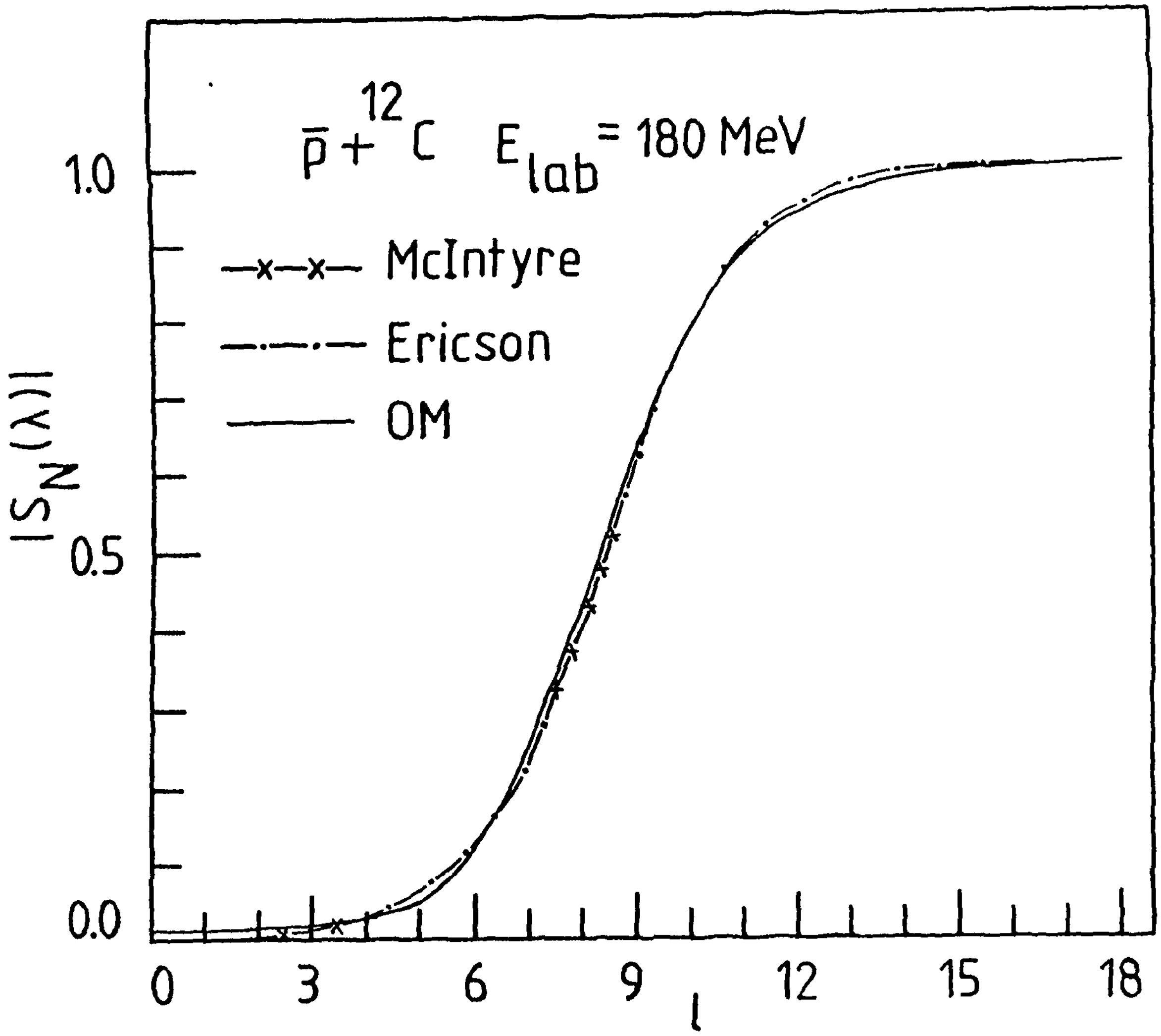

Fig.3.6.4a Plot of reflection function ($|S_N(\lambda)|$) for $\bar{p}$ + ^{12}C at E_{lab} = 180 MeV. The dash-dot-dash (— • —), dash-cross-dash (— x —) and solid (——) curves are the results of the Ericson and McIntyre parametrisations and the OM calculations respectively. OM parameters are contained in Table 3.6.1.

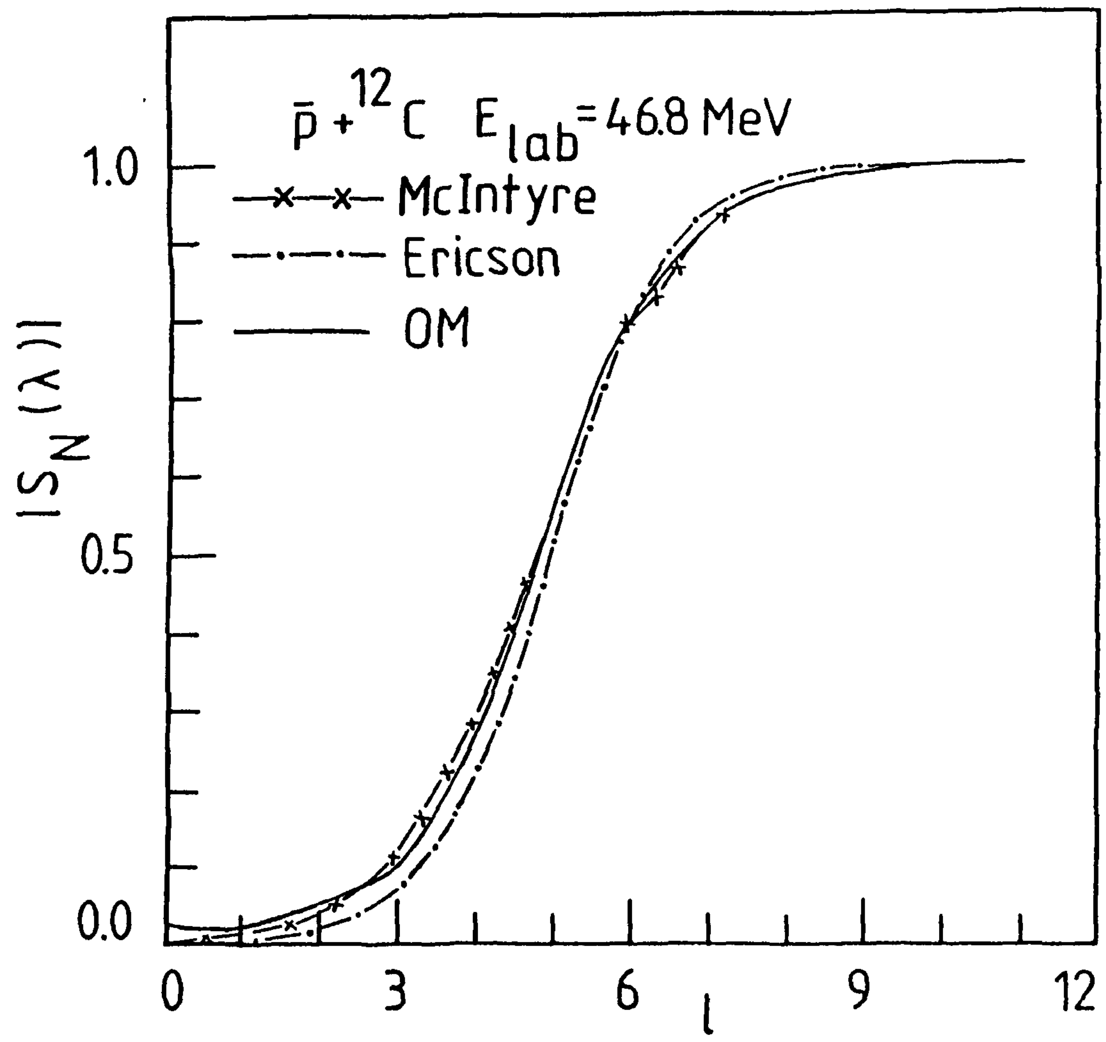

Fig.3.6.4b Same as Fig.3.6.4a for $\bar{p}$ + ^{12}C at E_{lab} = 46.8 MeV. OM potential parameters are contained in Table 3.6.1.

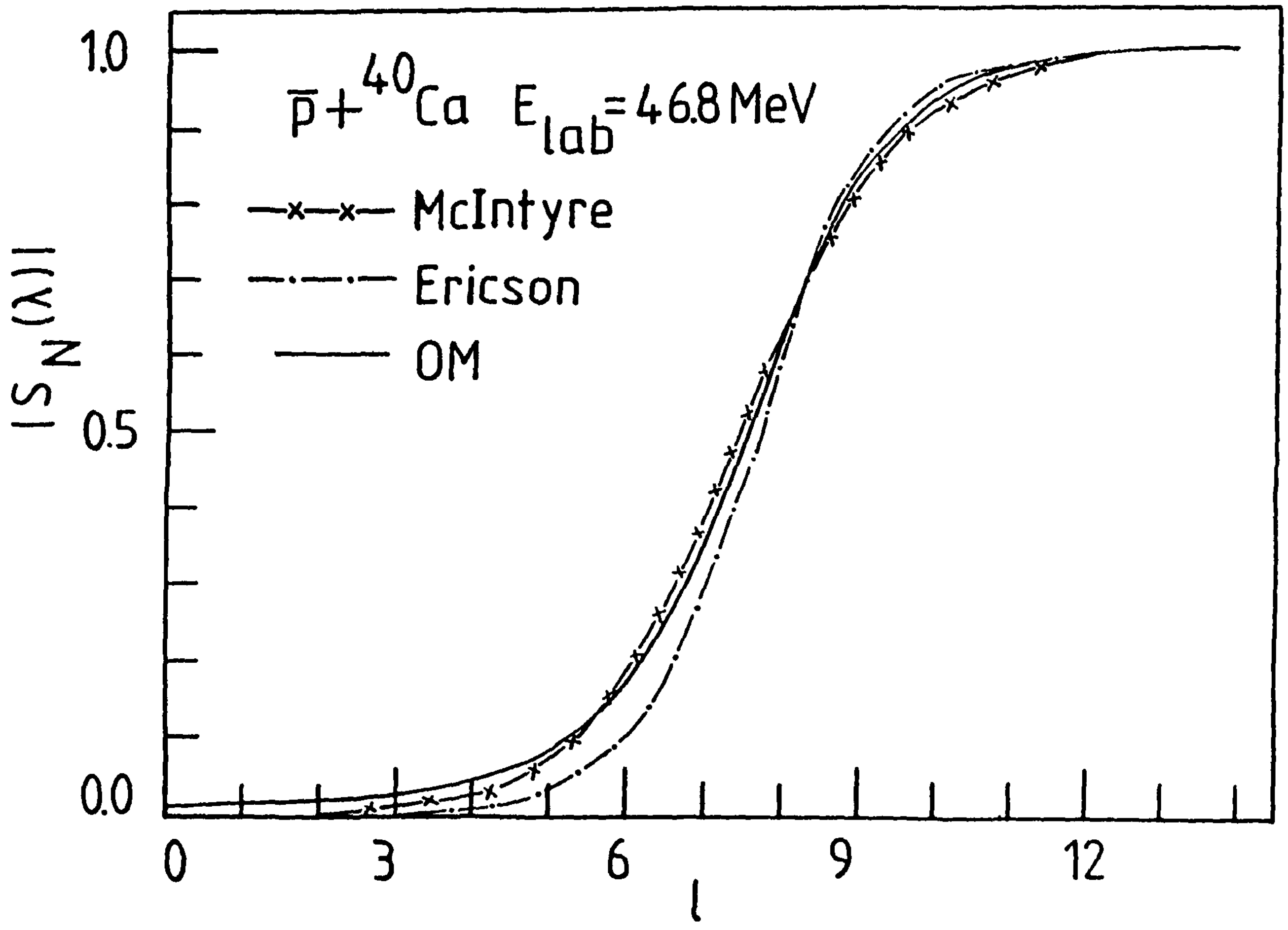

Fig.3.6.4c Same as Fig.3.6.4a for $\bar{p}$ + ^{40}Ca at E_{lab} = 46.8 MeV. OM potential parameters are contained in Table 3.6.1.

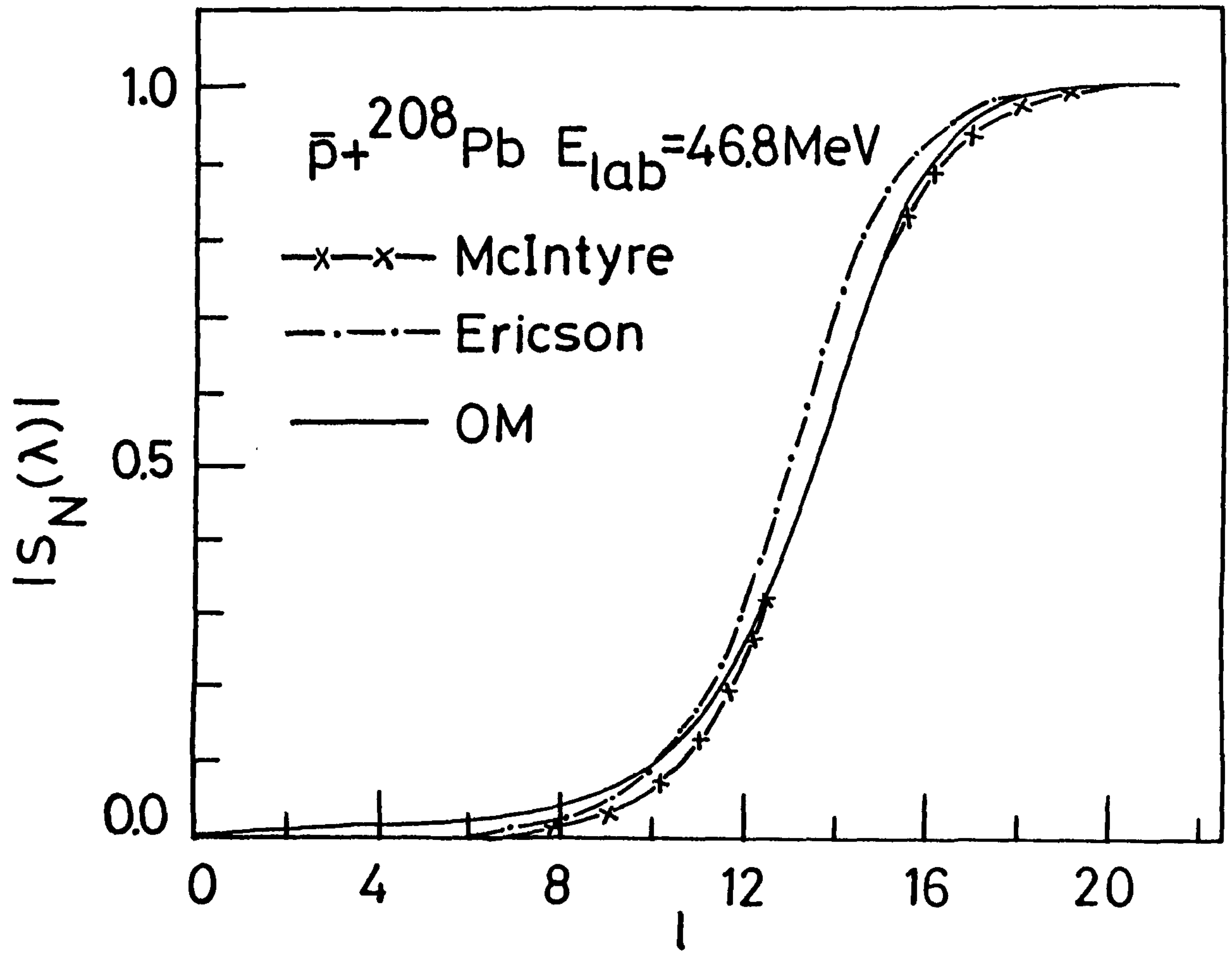

Fig.3.6.4d Same as Fig.3.6.4a for $\bar{p}$ + ^{208}Pb at E_{lab} = 46.8 MeV. OM potential parameters are contained in Table 3.6.1.

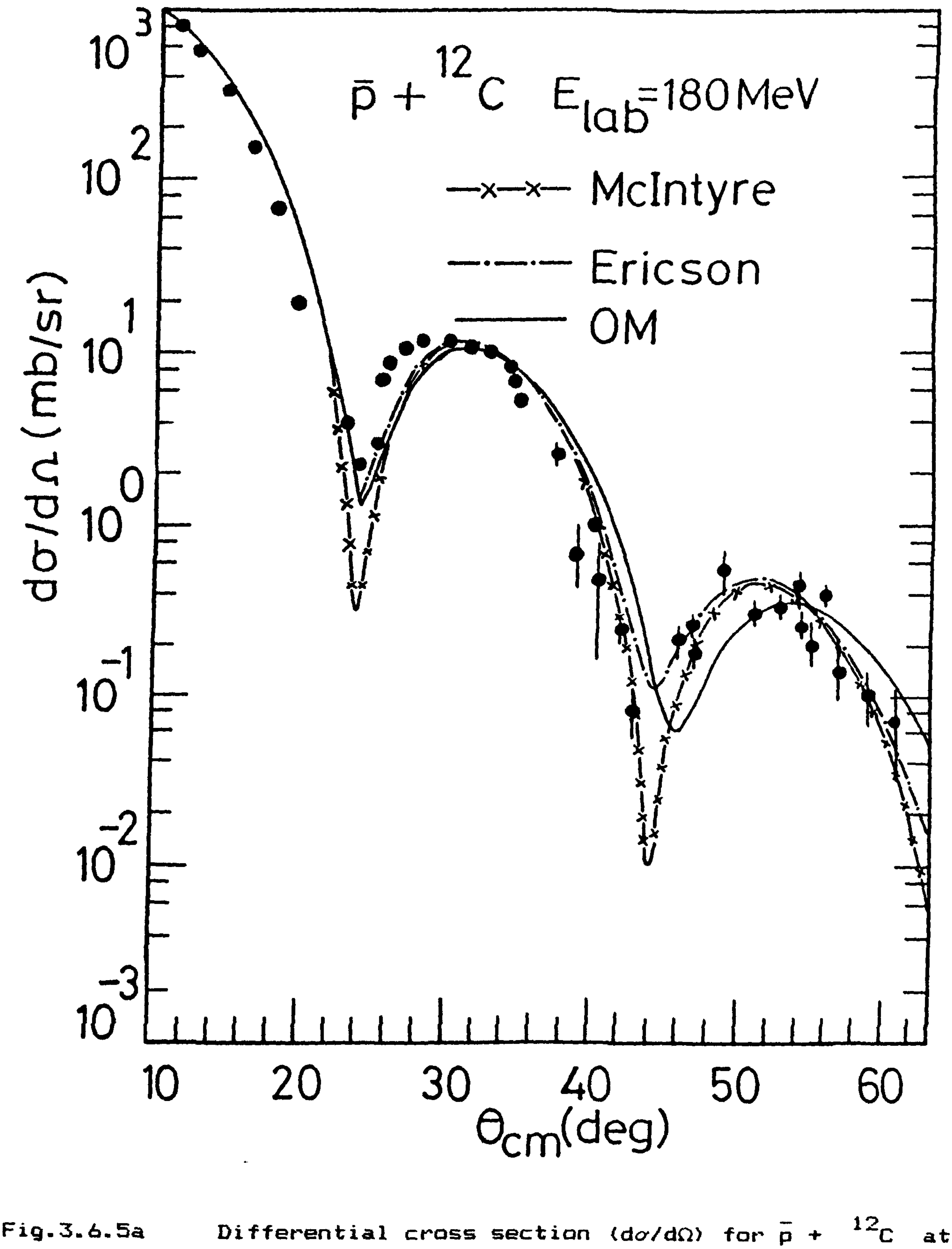

Fig.3.6.5a Differential cross section ($d\sigma/d\Omega$) for $\bar{p}$ + ${}^{12}C$ at E_{lab} = 180.0 MeV. Representations are same as that in Fig.3.6.4a. The experimental data are taken [Ja 86] at the energies as indicated in Table 3.6.2.

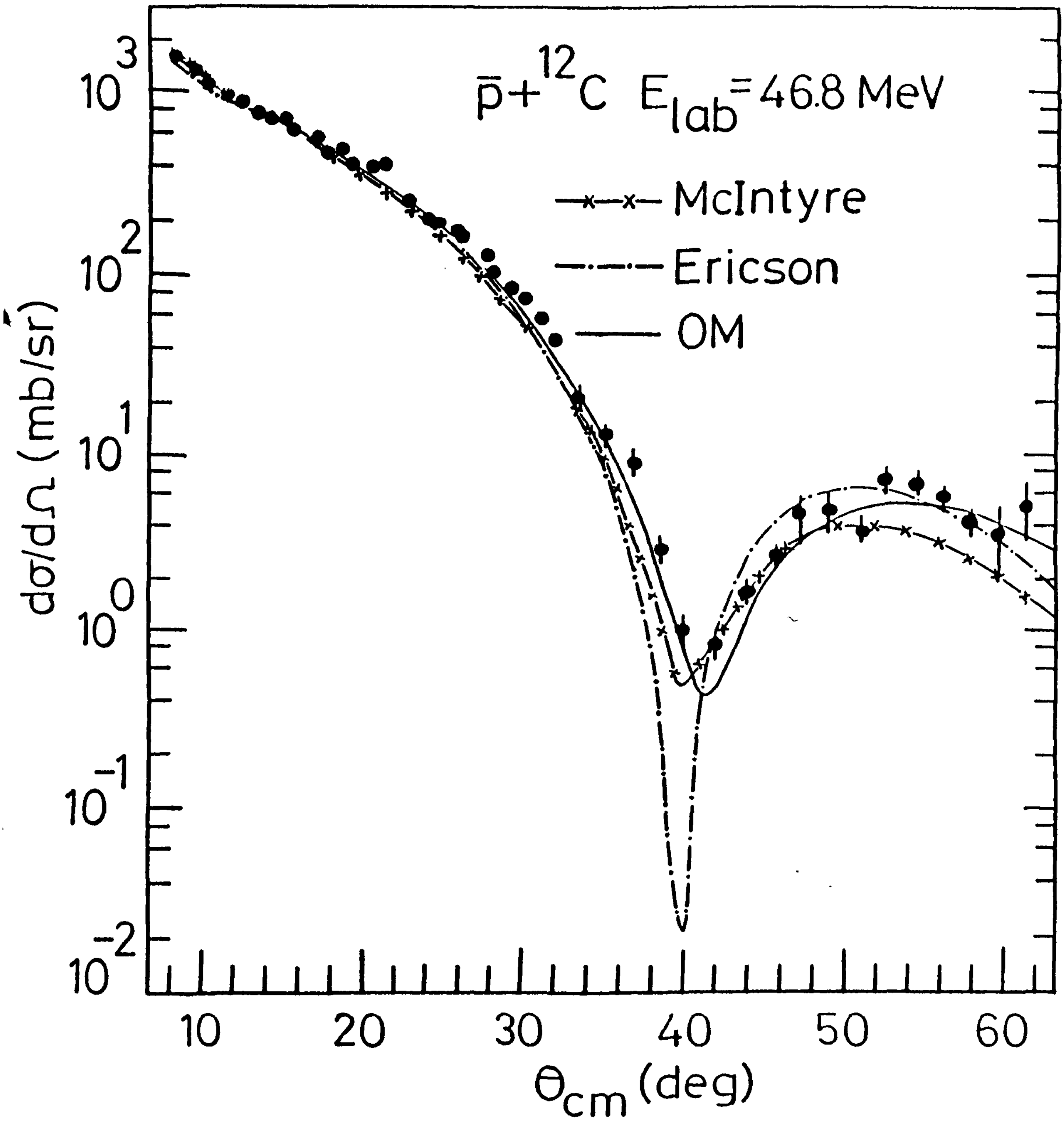

Fig.3.6.5b Same as Fig.3.6.5a for $\bar{p}$ + ^{12}C at E_{lab} = 46.8 MeV.

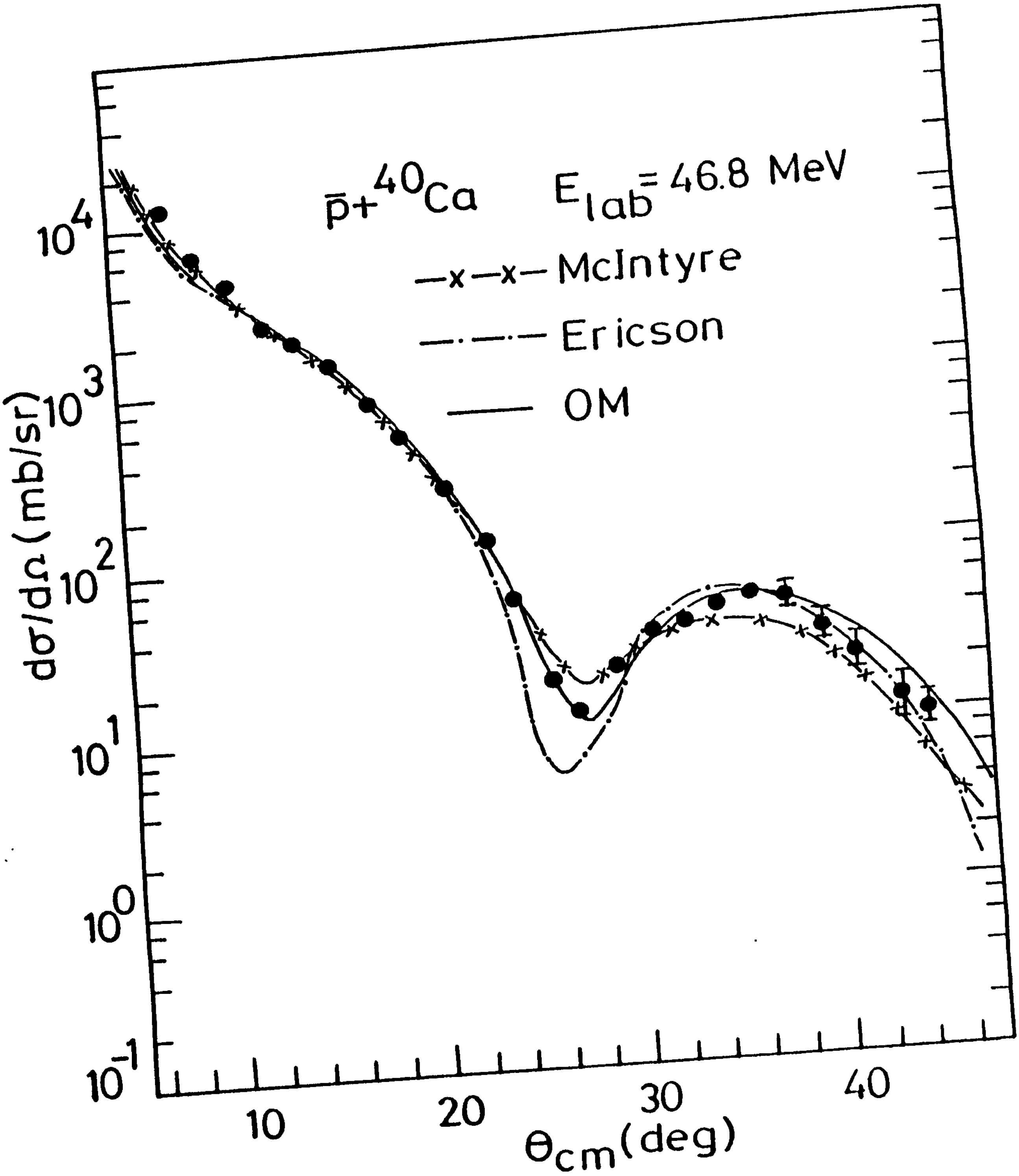

Fig.3.6.5c Same as Fig.3.6.5a for $\bar{p}$ + ^{40}Ca at E_{lab} = 46.8 MeV.

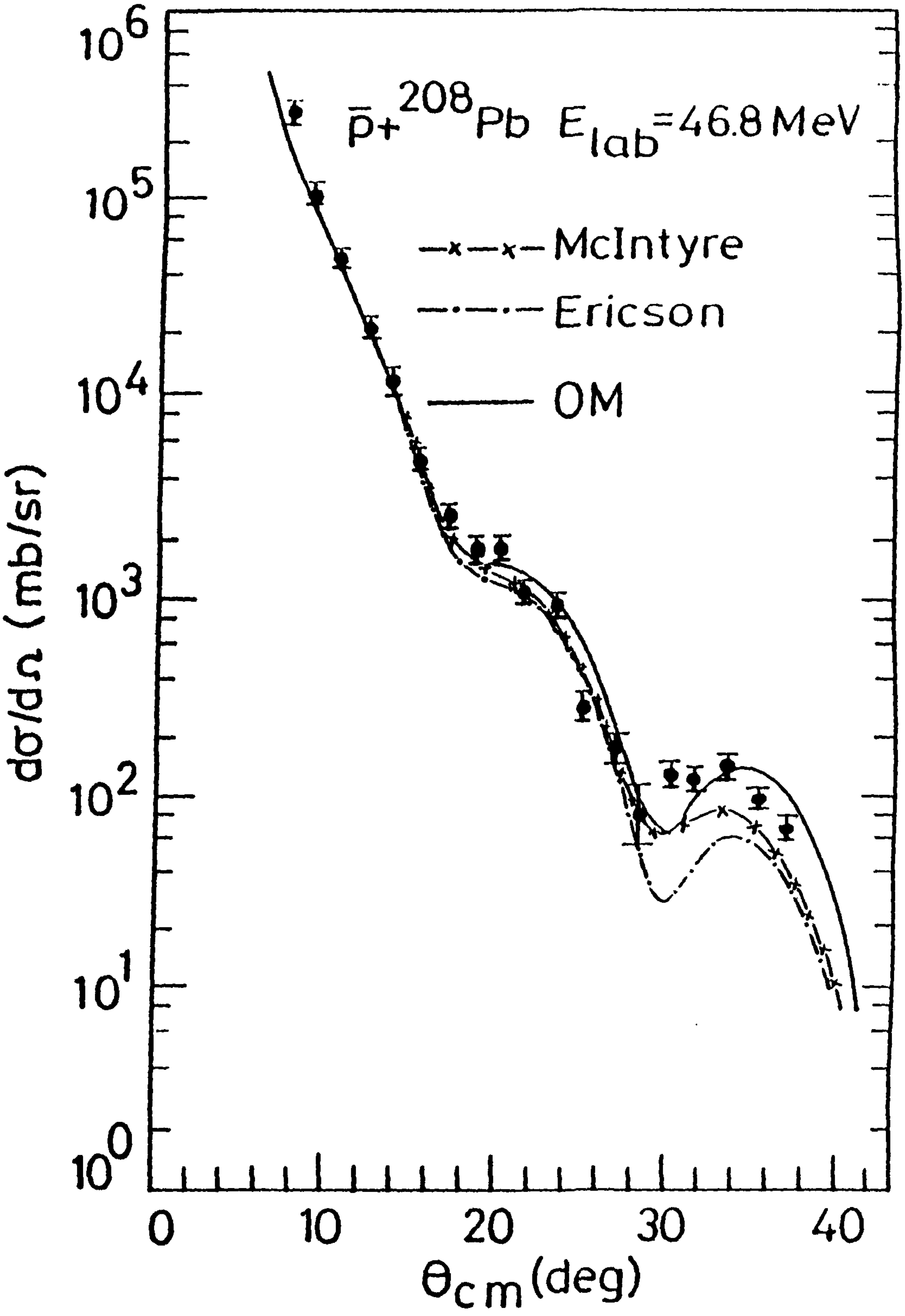

Fig.3.6.5d Same as Fig.3.6.5a for $\bar{p}$ + ^{208}Pb at E_{lab} = 46.8 MeV.

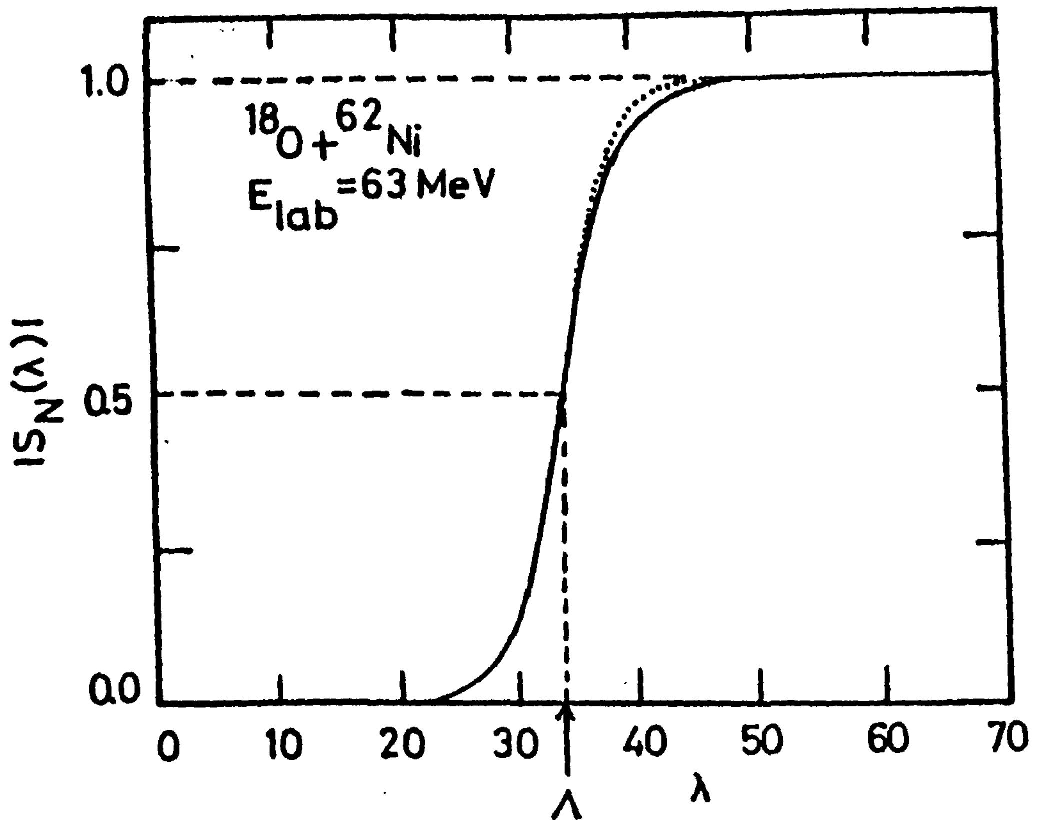

Fig.3.6.6 Variation of the reflection function $|S_N(\lambda)|$ for $^{18}O + ^{62}Ni$ at E_{lab} = 63 MeV. The dotted (.....) and solid (——) curves are the results of McIntyre parametrisation and OM calculation respectively.

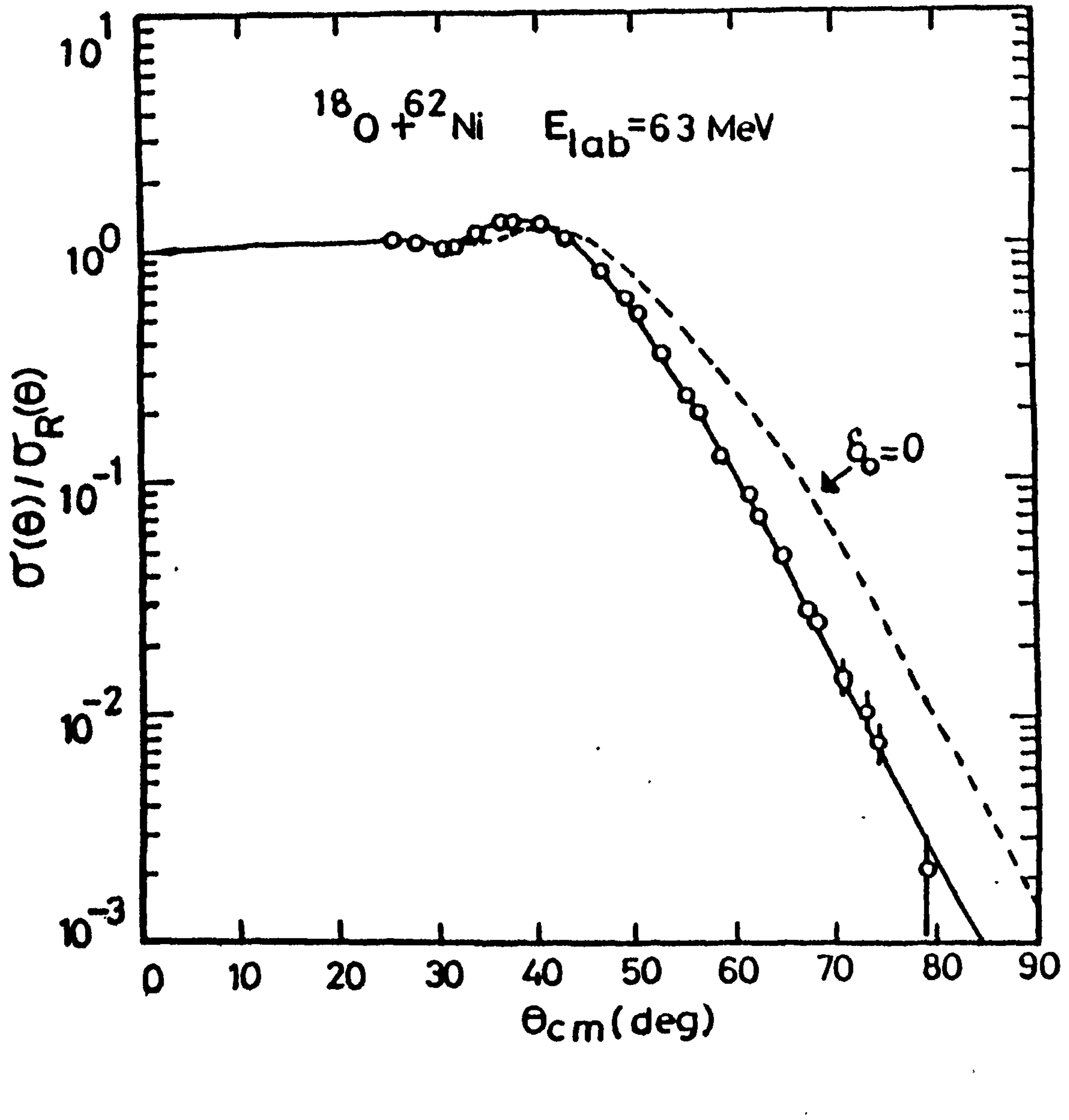

Fig.3.6.7 $\sigma(\theta)/\sigma_R(\theta)$ for $^{18}O + ^{62}Ni$ at E_{lab} = 63 MeV. The solid curve (——) is the result of McIntyre parametrisation and the dashed curve (----) corresponds to the same with δ_0 = 0. The experimental data are given in ref.[Re 75].

Table 3.6.4 McIntyre parameters of closed formalism analysis for $^{18}O + ^{62}Ni$ at E_{lab} = 63 MeV [Fr 78].

Λ	Δ	Λ_P	Δ_P	δ_o(deg)	χ^2	Expt.data
34	2.14±0.07	22.7±3	7.4±0.4	146±50	6	[Re 75]

heavy ion scattering data are equally useful in generating the reflection function for $\bar{p}$-A scattering also. Our results along with that of Frann et al. [Fr 78] establish the fact that, in case of surface dominant nuclear scattering showing semiclassical features, the closed formalism or parametric S matrix approach provides a simple method for the analysis of scattering data. In heavy ion physics, applicability of semiclassical approximations has led to extensive use of WKB techniques and closed formalism techniques for the analysis of scattering data. Our studies on some typical cases of low energy antiproton scattering indicate that these techniques can be expected to be useful in understanding different characteristic phenomena in the antiproton-nucleus scattering case also. However, unlike the case of heavy ion collision the number of experiments using low energy antiproton beams are relatively small due to the difficulties involved in the experimentation in low energy antiproton beams. But we believe as more extensive data become available, the semiclassical techniques and closed formalism methods can be expected to play a significant role in understanding the general properties of antiproton-nucleus scattering.

Reference

[Ab 64] Abramowitz. M and Stegun. I.A, *Handbook of mathematical functions* (New York, Dover 1964) p.374

[Bl 54] Blair. J.S, Phys. Rev. **95**(1954) 1218

[Bl 59] Blair. J.S, Phys. Rev. **115**(1959) 928

[Br 72] Broglia. R.A and Winther. A, Phys. Reports **4C**(1972) 153 and references therein

[Br 74] Broglia. R.A, Landowne. S, Malfliet. R.A, Rostokin. V and Winther. A, Phys. Reports **11C**(1974) 1 and references therein

[Br 85] Brink. D.M, *Semiclassical methods in nucleus-nucleus scattering* (Cambridge Univ. Press, Cambridge 1985)

[Ch 81] Chan. C.K, Subeka. P and Lu. P, Phys. Rev. **C24**(1981) 2035

[De 88] Dey. B, Shastry. C.S and Roy. T.K, Pramāna-J.Phys.**31**(1988) 173

[De 91] Dey. B and Shastry. C.S, Nuovo Cim.**104A**(1991) 139

[Er 53] Erdelyi. A, *Higher transcendental functions* I Bateman manuscript project (New York : McGraw-Hill, 1953) p.26

[Er 54] Erdelyi. A, *Table of integral transforms* I Bateman manuscript project (New York : McGraw-Hill, 1954) p.139

[Fo 59] Ford. K.W and Wheeler. J.A. Ann. Phys. **7**(1959) 259

[Fr 63] Frahn. W.E and Venter. R. H, Ann. Phys. **24**(1963) 243

[Fr 75] Frahn. W.E, *Classical and quantum mechanical aspects of heavy ion collisions*, Ed. by H.L. Harney, P.Braun-Munzinger and C.K.Gelbke, Lecture Notes in

Physics, Vol 33 (Springer-Verlag, Berlin, 1975) p.102

[Fr 78] Frahn. W.E and Rehm. K.E, Phys. Reports **37** (1978) 1

[Ga 84] Garreta. D et al., Phys. Latt. **135B**(1984) 206

[Ga 84a] Gambhir. Y.K and Shastry. C.S, Phys.Rev. **C30**(1984) 1343

[He 85] Heiselberg. H et al., Nucl. Phys. **A446**(1985) 637

[In 86] Ingemarsson. A, Nucl. Phys. **A454**(1986) 475

[Ja 86] Janouin. S et al., Nucl. Phys. **A451**(1986) 541

[Jo 75] Joachain.C.J, *Quantum collision theory* (Amsterdam,North Holland, 1975) p.210

[Ko 75] Koeling. T and Malfliet. R.A, Phys. Reports **22C**(1975) 181

[Kr 84] Kronenfeld. J, Gal. A and Eisenberg. J.M, Nucl. Phys. **A430**(1984) 525

[Ku 85] Kubo. K.-I, Toki. H and Igarashi. M, Nucl. Phys. **A435**(1985) 708

[La 34] Langer. R. E, Bull. Amer. Math. Soc. **40**(1934) 545

[La 37] Langer. R. E, Phys. Rev. **51**(1937) 669

[Ma 75] Malfliet. R. A, *Classical and quantum mechanical aspects of heavy ion collisions* Ed. by H. L. Hanrey, P. Braun-Munzinger and C.K. Gelbke, Lecture Notes in Physics, Vol. 33 (Springer-Verlag, Berlin, 1975) p.86

[Ma 78] Marty. C, *An analysis of heavy ion scattering amplitudes*, Lectures given at SUNY, (Stoney Brook,USA, 1978) Preprint

[Ma 84] MacKellar. A .D, Satchler. G. R and Yong. C. -Y, Z.Phys. **A316**(1984) 35

[Mc 60] McIntyre. J.A, Wong. K.H and Becker. L.C, Phys.Rev. **117**(1960) 1337

[Mc 70] McDowell. M. R. C and Coleman. J.P, *Introduction to the theory of ion-atom collisions* (North-Holland, Amsterdam, 1970) Chap 2

[Me 70] Merzbacher. E, *Quantum mechanics* (New York, Chichester, Brisbane, Toronto, John Wiley 1970) Chap.7

[Me 85] Mermaz. M.C, Z.Phys. A 321 (1985) 613

[No 80] Norenberg. W and Weidenmuler. H.A, *Introduction to the theory of heavy ion collisions* Ed.by J. Ehlers et al., Lecture Notes in Physics Vol. 51 (Springer-Verlag, Berlin, 1980) p. 89

[Re 75] Rehm. K.E et al.,Phys.Rev. C12(1975) 1945

[Sa 78] Satchler. G. R, *Some aspects of heavy ion scattering* Presented to the sixth INS Summer School on Nuclear Physics.(Japan, 1978)

[Sc 66] Scarborough. J.B, *Numerical mathematical analysis*, Sixth edition (Oxford and IBH publishing Co.1966) p.201

[Sh 82] Shastry. C.S, J. Phys.G : 8(1982) 1431

[Vi 76] Videbaek. F, Christensen. P.R, Hansen. O and Ulbak. K, Nucl.Phys. A256(1976) 301

CHAPTER 4

REGION-WISE ABSORPTION, INTERACTION TIME AND ANNIHILATION CROSS SECTION IN ANTIPROTON-NUCLEUS COLLISION

4.1 Introduction

In the last chapter we made a comparative study of antiproton-nucleus($\bar{p}$-A) collision and nucleus-nucleus collison and have shown that some of the approaches for the analysis of heavy ion scattering(HIS) are applicable to antiproton-nucleus scattering also [De 88]. We have also noted that in the case of heavy ions, extensive studies have been made by Shastry and Gambhir [Sh 84] to determine the region-wise absorption of incident flux in different regions of the interaction potential. The absorption or reaction cross section (σ_r) gives gross contribution to reaction from all the partial waves within the entire volume of the interaction potential. In order to test the sensitivity of the different regions of the interaction potential, a technique has been developed by Shastry and Gambhir [Sh 83, Sh 84] which gives the contribution to the reaction cross section for different partial waves from different regions around the scattering centre. The process of absorption in HIS, α-nucleus scattering and light nucleus-light nucleus scattering has been studied in great detail [Sh 83, Sh 84]. In the case of HIS ,it is found that the interior region is not explored even by those partial waves which are strongly absorbed and the absorption is peaked almost symmetrically around the surface region for different partial waves. More recently [Ud 85], in the case of heavy ion collision (HIC), the contribution to σ_r from the region $r < R_F$, where R_F is the fusion radius, is recognised as the fusion cross section σ_F. Thus, in the case of HIC, elastic scattering cross section, reaction cross section and fusion cross section data help us in understanding nucleus-nucleus interaction in some detail. In this chapter we have studied the general pattern of region-wise absorption of antiprotons inside the nucleus using several optical potentials which fit the experimental scattering data and compared the results with the corresponding results of proton-nucleus(p-A) collision and HIC. It is known that, in free space, the critical distance of approach for antiproton annihilation is less than 2 fm [Sh 87]. If one considers the total reaction cross section generated in the region $r < R_2$, where the mean free path Λ is less than 2 fm, as primarily annihilation cross section $\sigma^{\bar{p}A}_{ann}$, one may get an estimate of the contribution of $\sigma^{\bar{p}A}_{ann}$ to σ_r. This provides an alternative method to estimate $\sigma^{\bar{p}A}_{ann}$ and to understand the domain of the nucleus in which $\bar{p}$ annihilation dominates. A recent work [He 87], where $\bar{p}$-A interaction has been analysed, shows that annihilation probability is expected to increase in the nuclear matter. It also gives an estimate of $\sigma^{\bar{p}A}_{ann}$ in $\bar{p}$-A collision for a typical case namely, $\bar{p}$ + ^{12}C at E_{lab}= 175 MeV. Here we have demonstrated a procedure to estimate $\sigma^{\bar{p}A}_{ann}$ using the concepts of region-wise absorption and mean free path.

Another important factor of interest, is the time scale involved in $\bar{p}$-A collision. It has been estimated that $\bar{p}$-p annihilation time $\tau_{\bar{p}p}$ is of the order of 5×10^{-24}s [Go 88]. This should be compared with the maximum time that $\bar{p}$ can be expected to spend within the nucleus before getting into annihilation or other reaction channels. In the case of HIC, the time estimates for fusion have been obtained using classical Coulomb trajectory or Coulomb-nuclear trajectory [Br 83, Sc 86]. These compare favourably well with the corresponding results obtained by using semiclassical or quantal methods [Sa 88]. Since $\bar{p}$-A collision has semiclassical features [De 88], the evaluation of $\bar{p}$-A interaction time $\tau_{\bar{p}A}$ using classical $\bar{p}$-A trajectory is meaningful. We have estimated $\bar{p}$-A interaction time and the results are compared with the corresponding results of HIC and p-A collision. We have also compared the estimated time $\tau_{\bar{p}A}$ with $\tau_{\bar{p}p}$ for several cases. Similarly, $\bar{p}$-p annihilation cross section $\sigma_{ann}^{\bar{p}p}$ in free space [Ra 80] is also compared with the $\bar{p}$-A reaction cross section σ_r. The ratios $\sigma_r/\sigma_{ann}^{\bar{p}p}$, and $\tau_{\bar{p}A}/\tau_{\bar{p}p}$ are examined in order to determine the correlation, if any, between $\bar{p}$-A reaction cross section and interaction time.

In Sec. 4.2, a technique for region-wise absorption analysis of reaction cross section and associated terms which are relevant to the present work is discussed. In Sec. 4.3, region-wise absorption analysis for $\bar{p}$-A and p-A scattering systems is carried out and the results of region-wise absorption of $\bar{p}$ within the nucleus are compared with that of HIC and p-A collision. An estimate of $\bar{p}$-A annihilation cross section $\sigma_{ann}^{\bar{p}A}$ is also indicated using the concepts of region-wise absorption and mean free path. In Sec. 4.4, details of $\bar{p}$-A interaction time and its implication in $\bar{p}$-A reaction cross section inside the nucleus is given. Section 4.5 contains the summary and conclusion.

4.2 Mathematical formulation for the analysis of region-wise absorption

The two experimentally observable physical quantities are the differential scattering cross section $(d\sigma/d\Omega)$ and the reaction or absorption cross section σ_r. The complex potential, or more explicitly, the imaginary part of the optical model potential characterises the absorptive properties of the nuclear medium. The imaginary part of the complex potential is responsible for the loss of flux from the incident beam leading to reaction cross section generated by all non-elastic channels. Since the reaction cross section gives the gross effect of all the partial waves within the region of interaction, it is interesting to find the contribution of each partial wave to reaction cross section from the region r and r+Δ. Before going into the details of absorption process from a small region we first give some useful mathematical details which are relevant to our analysis. The probability current density $(\bar{J})$ associated with the wave has the general form

$$\bar{J} = (\hbar/2i\mu)\left[\psi^{*}(\bar{r})\ \bar{\nabla}\ \psi(\bar{r}) - \psi(\bar{r})\ \bar{\nabla}\ \psi^{*}(\bar{r})\right]$$

$$= \mathrm{Re}\left[(\hbar/i\mu)\ \psi^{*}(\bar{r})\ \bar{\nabla}\ \psi(\bar{r})\right] \qquad (4.2.1)$$

The Schrodinger equation for a complex potential V(r) is

$$\left[-\frac{\hbar^2}{2\mu}\,\bar{\nabla}^2 + V(r)\right]\psi(\bar{r}) = E\,\psi(\bar{r}). \qquad (4.2.2)$$

Multiplying Eq. (4.2.2) by $\psi^*(\bar{r})$ and its(i.e., of Eq. (4.2.2)) complex conjugate by $\psi(\bar{r})$ and substracting one gets

$$-(\hbar^2/2\mu)\bar{\nabla}.\left[\psi^*(\bar{r})\;\bar{\nabla}\,\psi(\bar{r})-\psi(\bar{r})\;\bar{\nabla}\,\psi^*(\bar{r})\right] = \left[\psi(\bar{r})\;V^*(r)\;\psi^*(\bar{r}) - \psi^*(\bar{r})\;V(r)\;\psi(\bar{r})\right]. \qquad (4.2.3)$$

Assuming $V(r)$ to be of the form $V(r) = \mathrm{Re}\,V(r) + i\,\mathrm{Im}\,V(r)$, Eq. (4.2.3) can be simplified to the form

$$\bar{\nabla}.\bar{J} = (2/\hbar)\;\mathrm{Im}\;V(r)\;|\psi(\bar{r})|^2 . \qquad (4.2.4)$$

Now, the reaction cross section σ_r which is of our interest can be defined as the number of particles absorbed per unit incident flux. Mathematically it can be expressed as

$$\sigma_r = -(\mu/\hbar k)\int \bar{J}.\,\hat{n}\;d\bar{s}$$
$$= -(\mu/\hbar k)\int \bar{\nabla}.\bar{J}\;d\bar{r}\,. \qquad (4.2.5)$$

In the above equation, $\hbar k$ represents the incident momentum in the centre-of-mass system and $(\hbar k/\mu)$ gives the magnitude of the incident probability flux. Using Eq. (4.2.4), Eq. (4.2.5) can be written in the form

$$\sigma_r = -\,(2\mu/\hbar^2 k)\int \mathrm{Im}\;V(r)\;|\psi(\bar{r})|^2\;d\bar{r}\,. \qquad (4.2.6)$$

In the S matrix approach, one can express σ_r as

$$\sigma_r = (\pi/k^2)\sum_{l=0}^{\infty}(2l+1)\;(1-\eta_l^2), \qquad (4.2.7)$$

where $\quad \eta_l = |S(\lambda,k)|$.

Equation (4.2.7) indicates that maximum absorption results when $\eta_l = 0$. But it does not throw any light on the region from where maximum absorption takes place. On the other hand, from Eq.

(4.2.6) it is clear that maximum absorption of the incident flux will occur in the region where Im $V(r)|\psi(\bar{r})|^2$ is maximum. Again, a volume absorptive potential may not generate significant absorption in the entire volume because $|\psi(\bar{r})|^2$ may be quite small in some regions. Thus, in order to test the degree of sensitivity of the different regions towards the reaction cross section, it is necessary to find the absorption cross section ($\sigma_r(r_i,\Delta)$, which gives the contribution of the flux absorbed inside a shell of radius r_i and $r_i + \Delta$, for small Δ → 0) arising from a very small region around the scattering centre. Thus, the reaction cross section can be written in the form

$$\sigma_r = \sum_{i=0}^{\infty} \sigma_r(r_i,\Delta), \qquad r_0 = 0,\ r_i = r_0 + \Delta,\ \Delta \to 0 \qquad (4.2.8)$$

where $\sigma_r(r_i,\Delta)$ is given by

$$\sigma_r(r_i,\Delta) = -\,(2\mu/\hbar^2)\int_{r_i}^{r_i+\Delta}\int \psi^*(\bar{r})\ \psi(\bar{r})\ \mathrm{Im}\ V(r)\ r^2dr\ d\Omega \qquad (4.2.9)$$

Thus, $\sigma_r(r_i, \Delta)$ gives the contribution to σ_r in the region $r_i \leq r \leq r_i+\Delta$. It is clear that the imaginary part of the interaction potential as well as the real part of the interaction (which comes through the wave function $\psi(r)$) play an important part in the absorption process rather than the imaginary part of the potential alone. In order to analyse the absorption process from different regions it is necessary to solve the Schrodinger equation.

For a pure Coulomb scattering the radial Schrodinger equation for the l^{th} partial wave is

$$\frac{d^2}{dr^2}\,\phi_c(\lambda,k,r) + \left[k^2 - \frac{\lambda^2 - 1/4}{r^2} - \frac{2\eta k}{r}\right]\phi_c(\lambda,k,r) = 0, \tag{4.2.10}$$

where $k^2 = 2\mu E/\hbar^2$, $\eta = Z_P Z_T e^2\mu/\hbar^2 k$ and $\lambda = l + 1/2$. Z_P, Z_T and μ having their usual meaning and E is the centre-of-mass energy. In the presence of a nuclear potential $V(r)$ $(V(r) = V_R(r) + iW_I(r))$, the corresponding radial Schrodinger equation for the l^{th} partial wave becomes

$$\frac{d^2}{dr^2}\,\phi(\lambda,k,r) + \left[k^2 - \frac{\lambda^2 - 1/4}{r^2} - V_N(r) - \frac{2\eta k}{r}\right]\phi(\lambda,k,r) = 0, \tag{4.2.11}$$

$$\text{where } V_N(r) = 2\mu/\hbar^2\left[V(r) + V_c(r) - Z_P Z_T e^2/r\right]$$

$$= 2\mu/\hbar^2\left[V_R(r) + iW_I(r) + V_c(r)\right] - \frac{2\eta k}{r}.$$

$V_c(r)$ is the Coulomb potential and its general form is given in Chapter 3 (Eq.3.3.2). Here we have assumed that the reduced potential $V_N(r)$ is less singular than r^{-2} at the origin and vanishes faster than r^{-3} at infinity. Thus $V_N(r)$ is such that it satisfies the following conditions [Jo 75]:

$$\text{(i)} \qquad \int_0^\infty r\,|V_N(r)|\,dr < \infty$$

$$\tag{4.2.12}$$

$$\text{(ii)} \qquad \int_0^\infty r^2\,|V_N(r)|\,dr \quad \infty$$

The regular solution $\phi(\lambda,k,r)$ behaves like $r^{\lambda+1/2}$ near the origin. The irregular solution $f(\lambda,\pm k,r)$ also known as Jost solutions behave asymptotically as

$$f(\lambda,\pm k,r) \xrightarrow[r\to\infty]{} \exp(\mp i(kr - \eta \ln 2kr)). \qquad (4.2.13)$$

Asymptotically $\phi(\lambda,k,r)$ is a superposition of incoming and outgoing Coulomb distorted spherical waves. Similar boundary conditions hold good for the Coulomb wave functions $\phi_c(\lambda,k,r)$ and $f_c(\lambda,\pm k,r)$ which can be represented by the Whittacker functions $M_{i\eta,\lambda}$ and $W_{\pm i\eta,\lambda}$ respectively [Ab 64] and are written as

$$\phi_c(\lambda,k,r) = (2ik)^{-\lambda-1/2} M_{i\eta,\lambda}(2ikr)$$

and (4.2.14)

$$f_c(\lambda,\pm k,r) = W_{\pm i\eta,\lambda}(\pm 2ikr).$$

Since the solutions $f(\lambda,+k,r)$ and $f(\lambda,-k,r)$ (except for $k=0$) are linearly independent, the regular solution $\phi(\lambda,k,r)$ in the asymptotic region can be expressed as

$$\phi(\lambda,k,r) = A(k)f(\lambda,k,r) + B(k)f(\lambda,-k,r), \qquad (4.2.15)$$

where $A(k)$ and $B(k)$ are the coefficients which can be evaluated using the Jost function approach [De 65, Sh 83]. To find the coefficients we proceed in the following way. The Wronskian of two solutions $\phi(x)$ and $\psi(x)$ can be defined as

$$W(\phi(x),\ \psi(x)) = \phi(x)\psi'(x) - \phi'(x)\psi(x). \qquad (4.2.16)$$

Using Eq. (4.2.15) one can write

$$W(\phi(\lambda,k,r),\ f(\lambda,k,r)) = \phi(\lambda,k,r)\ f'(\lambda,k,r) - f(\lambda,k,r)\phi'(\lambda,k,r)$$
$$= B(k)\ W(f(\lambda,-k,r),\ f(\lambda,k,r)). \qquad (4.2.17)$$

Similarly,

$$W(\phi(\lambda,k,r),\ f(\lambda,-k,r)) = A(k)\ W(f(\lambda,k,r),\ f(\lambda,-k,r)).$$

(4.2.18)

Using the fact that the Wronskian of two linearly independent solutions $f(\lambda,\pm k,r)$ is independent of r, i.e.,

$$W(f(\lambda,k,r),\ f(\lambda,-k,r)) = f(\lambda,k,r)f'(\lambda,-k,r) - f(\lambda,-k,r)f'(\lambda,k,r)$$
$$= 2ik, \qquad (4.2.19)$$

we obtain from Eqs.(4.2.17) and (4.2.18)

$$B(k) = -\frac{1}{2ik}\, W(\phi(\lambda,k,r),\ f(\lambda,k,r)) \qquad (4.2.20)$$

and

$$A(k) = \frac{1}{2ik}\, W(\phi(\lambda,k,r),\ f(\lambda,-k,r)). \qquad (4.2.21)$$

We now define the Jost functions $F(\lambda,\pm k)$ as follows [De 65, Jo 47]

$$F(\lambda,\pm k) = W(\phi(\lambda,k,r),\ f(\lambda,\pm k,r)) \qquad (4.2.22)$$

In terms of Jost functions (cf. Eq.(4.2.22)), Eq.(4.2.15) can be written as

$$\phi(\lambda,k,r) = \frac{1}{2ik}\left[F(\lambda,-k)\ f(\lambda,k,r) - F(\lambda,k)\ f(\lambda,-k,r)\right]. \qquad (4.2.23)$$

Using similar analogy the regular Coulomb wave function $\phi_c(\lambda,k,r)$ can be expressed in terms of Coulomb Jost functions $F_c(\lambda,\pm k)$ as

$$\phi_c(\lambda,k,r) = \frac{1}{2ik}\left[F_c(\lambda,-k)\ f_c(\lambda,k,r) - F_c(\lambda,k)\ f_c(\lambda,-k,r)\right], \qquad (4.2.24)$$

where

$$F_c(\lambda,\pm k) = (2k)^{-\lambda+1/2}\ \exp\ (\pi\eta/2)\ \exp(\mp\ i\ell\pi/2)\ \frac{\Gamma(2\ell+2)}{\Gamma(\ell+1\mp i\eta)}\ . \qquad (4.2.25)$$

The Coulomb S matrix $S_c(\lambda,k)$ is given by

$$S_c(\lambda,k) = \exp(i\ell\pi)\ \left[F_c(\lambda,k)/F_c(\lambda,-k)\right]$$
$$= \Gamma(\ell+1+i\eta)/\ \Gamma(\ell+1-i\eta) = \exp(2i\sigma_\ell). \qquad (4.2.26)$$

σ_ℓ is known as the Coulomb phase shift and is written as

$$\sigma_\ell = \arg\ \Gamma(\ell+1-i\eta). \qquad (4.2.27)$$

The S matrix $S(\lambda,k)$ is given by

$$S(\lambda,k) = \exp(il\pi)\left[F(\lambda,k)/F(\lambda,-k)\right] \qquad (4.2.28)$$

and the nuclear S matrix $S_N(\lambda,k)$ can be written as $S_N(\lambda,k) = S(\lambda,k)/S_c(\lambda,k)$ and the reflection function is given by

$$\eta_l = |S(\lambda,k)| = |S_N(\lambda,k)|. \qquad (4.2.29)$$

In order to find $(1-\eta_l^2)$, we start with Eq. (4.2.11) and obtain

$$\frac{d}{dr}\left[\phi^* \frac{d\phi}{dr} - \phi \frac{d\phi^*}{dr}\right] = 2i\phi^* \, \mathrm{Im} V_N(r)\phi. \qquad (4.2.30)$$

λ,k,r dependence in ϕ are dropped out for convenience. Integrating it between the limits r_i and $r_i+\Delta$ we get

$$\left[\phi^* \frac{d\phi}{dr} - \phi \frac{d\phi^*}{dr}\right]_{r_i}^{r_i+\Delta} = 2i \int_{r_i}^{r_i+\Delta} \mathrm{Im}\, V_N(r)\,|\phi|^2. \qquad (4.2.31)$$

Using Eq. (4.2.23) it can be shown that, Eq. (4.2.31) can be reduced to the form [Sh 83]

$$1-\eta_l^2 = -4k \int_0^\infty \mathrm{Im}\, V_N(r) \left|\frac{\phi(\lambda,k,r)}{F(\lambda,-k)}\right|^2 dr$$

$$= \sum_{i=0}^{\infty} \chi_r(\lambda,r_i,\Delta), \qquad r_0 = 0,\ r_{i+1} = r_i+\Delta,\ \Delta \quad 0$$

$\chi_r(\lambda,r_i,\Delta)$ is given by the expression

$$\chi_r(\lambda,r_i,\Delta) = -4k\ \mathrm{Im} \left|\frac{\phi'(\lambda,k,r)}{F(\lambda,-k)}\ \frac{\phi^*(\lambda,k,r)}{F^*(\lambda,-k)}\right|_{r_i}^{r_i+\Delta}. \qquad (4.2.32)$$

The superscript prime in $\phi(\lambda,k,r)$ denotes the derivative with respect to r and $\chi_r(\lambda,r_i,\Delta)$ gives the contribution to $(1-\eta_l^2)$ from the region $r_i \le r \le r_i+\Delta$. The function $(1-\eta_l^2)$ is quite useful in determining the relative importance of different regions in generating σ_r which is given by

$$\sigma_r = (\pi/k^2)\sum_{l=0}^{\infty}(2l+1)\ (1-\eta_l^2)$$

$$= (\pi/k^2)\ \sum_{i=0}^{\infty}\ \sum_{l=0}^{\infty}(2l+1)\ \chi_r(\lambda,r_i,\Delta). \qquad (4.2.33)$$

The reaction cross section $\sigma_r(r_i,\Delta)$ generated in the region $r_i \leq r \leq r_i+\Delta$ is

$$\sigma_r(r_i,\Delta) = (\pi/k^2)\sum_{l=0}^{\infty}(2l+1)\ \chi_r(\lambda,r_i,\Delta). \qquad (4.2.34)$$

Further the contribution to σ_r from the region $0 \leq r \leq r_N$ can be expressed as

$$\left[\sigma_r\right]_0^{r_N} = \sum_{i=0}^{N}\ \sigma_r(r_i,\Delta). \qquad (4.2.35)$$

4.3 Analysis of region-wise absorption

Using the above mentioned technique, analysis was carried out to explore different regions of the nuclear medium for absorption of $\bar{p}$ in the case of antiproton-nucleus scattering system. The elastic scattering cross section and the reaction cross section data [Ai 81, As 85, Co 84, Ga 84, Ga 84a, He 85, Ja 86, Na 84, Ni 83] are available for several targets like ^{12}C, ^{16}O, ^{40}Ca, ^{208}Pb etc. at several incident energies. In addition to these experimental data, information regarding annihilation cross section may further facilitate a simple way of estimating annihilation cross section from the technique of region-wise absorption. The experimental information enables us to find the contribution to the reaction cross section from a small region and consequently this provides an alternative and simple method of estimating approximate annihilation cross section. In order to perform the analysis for $\bar{p}$-A and p-A scatterings the nuclear part of the optical model (OM) potential is assumed to be of Woods-Saxon type, i.e.,

$$V(r) = -V_0\left[1 + \exp\left(\frac{r-R_r}{a_r}\right)\right]^{-1} - iW_0\left[1 + \exp\left(\frac{r-R_I}{a_I}\right)\right]^{-1}$$

$$= V_R(r) + iW_I(r). \qquad (4.3.1)$$

The parameters V_0, W_0, r_r, r_I, a_r, a_I and r_c, the Coulomb radius parameter, used in the calculation, are given in Table 4.3.1. $\chi_r(\lambda,r,\Delta)$, $\sigma_r(r,\Delta)$ and $\left[\sigma_r\right]_0^r$ are evaluated numerically using equations (4.2.32), (4.2.34) and (4.2.35) for different systems as indicated in the Table 4.3.1. The symbol $\sigma_r(r,\Delta)$ signifies the contribution to the reaction cross section from the spherical shell of radius r and thickness Δ, whereas $\left[\sigma_r\right]_0^r$ gives the contribution to the total reaction cross section σ_r from the spherical volume of radius r around the scattering centre. The function $\chi_r(\lambda,r,\Delta)$ gives the contribution to $(1-\eta_l^2)$ within the region $(r,r+\Delta)$. The variations of $\chi_r(\lambda,r,\Delta)$ as a function of r for different values of partial waves, l, are depicted in Figs. 4.3.1 - 4.3.3. Figures 4.3.1 and 4.3.2 show the pattern of absorption in the case of $\bar{p}$ + ^{12}C and $\bar{p}$ +^{40}Ca scattering systems at E_{lab} = 46.8 MeV respectively while Fig. 4.3.3 shows the corresponding result for p+^{12}C scattering system at E_{lab} = 46.2 MeV. From the Figs. 4.3.1 and 4.3.2 one finds that even the partial waves, which are more or less fully absorbed, cannot explore the interior region, rather, $\chi_r(\lambda,r,\Delta)$ for all l are confined mostly to the surface region. In contrast to Figs. 4.3.1 and 4.3.2, Fig. 4.3.3 indicates

Table 4.3.1 Optical model potential parameters alongwith the Coulomb radius parameter r_c for various systems.

System	E_{lab} (MeV)	V_0 (W_0) (MeV)	r_r (r_I) (fm)	a_r (a_I) (fm)	r_c (fm)	Remarks
$\bar{p} + {}^{12}C$	46.8 1)	40.0	1.03	0.562	1.3	Fig.4.3.1
		(74.1)	(1.07)	(0.625)		Fig.4.3.4
$\bar{p} + {}^{12}C$	46.9 1)	90.0	0.621	0.705	1.3	Fig.4.3.6
		(108.9)	(0.962)	(0.632)		
$\bar{p} + {}^{40}Ca$	46.8 2)	40.0	1.10	0.60	1.3	Fig.4.3.2
		(100.0)	(1.10)	(0.60)		Fig.4.3.5
$p + {}^{12}C$	46.3 3)	41.5	1.143	0.643	1.2	Fig.4.3.3
		(9.7)	(1.143)	(0.643)		Fig.4.3.4
${}^{18}O + {}^{58}Ni$	60.00 4)	90.10	1.22	0.500	1.25	Fig.4.3.7
		(42.90)	(1.22)	(0.500)		Fig.4.3.8
$\bar{p} + {}^{12}C$	46.8 5)	25.0	1.22	0.560	1.3	Fig.4.4.1
		(61.0)	(1.17)	(0.560)		
$\bar{p} + {}^{40}Ca$	47.9 5)	9.0	1.40	0.630	1.3	Fig.4.4.1
		(143.0)	(1.03)	(0.630)		
$\bar{p} + {}^{208}Pb$	47.9 2)	20.0	1.10	0.650	1.3	Fig.4.4.1
		(140.0)	(1.10)	(0.650)		
$p + {}^{12}C$	46.8 6)	40.07	1.17	0.750	1.3	Fig.4.4.1
		(7.6)	(1.32)	(0.510)		

Table 4.3.1 contd.

System	E_{lab} (MeV)	V_0 (W_0) (MeV)	r_r (r_1) (fm)	a_r (a_1) (fm)	r_c (fm)	Remarks
$p + {}^{40}Ca$	47.9 6)	41.04	1.17	0.750	1.3	Fig.4.4.1
		(7.82)	(1.32)	(0.510)		
$p + {}^{208}Pb$	47.9 6)	49.29	1.17	0.750	1.3	Fig.4.4.1
		(7.84)	(1.32)	(0.658)		
$\bar{p} + {}^{12}C$	179.7 7)	90.00	0.859	0.549	1.3	Fig.4.4.2
		(135.29)	(1.014)	(0.557)		
$\bar{p} + {}^{40}Ca$	179.9 7)	60.00[a]	0.766	0.991	1.3	Fig.4.4.2
		(154.28)	(1.051)	(0.619)		Fig.4.4.3
		80.00[b]	0.67	1.000	1.3	Fig.4.4.3
		(154.88)	(1.05)	(0.620)		
		200.00[c]	0.371	1.018	1.3	Fig.4.4.3
		(162.85)	(1.036)	(0.625)		
$\bar{p}+{}^{208}Pb$	180.3 7)	60.00	1.122	0.587	1.3	Fig.4.4.2
		(64.64)	(1.166)	(0.739)		
${}^{81}Br+{}^{90}Zr$	315.02 9)	35.00	1.35	0.430	1.35	Fig.4.4.2
		(12.13)	(1.35)	(0.430)		

1):[Ku 85], 2):[He 85], 3):[Sa 67], 4):[Vi 76], 5):[Ja 86],

6):[Be 69], 7):[In 86], 8):[Ud 85]

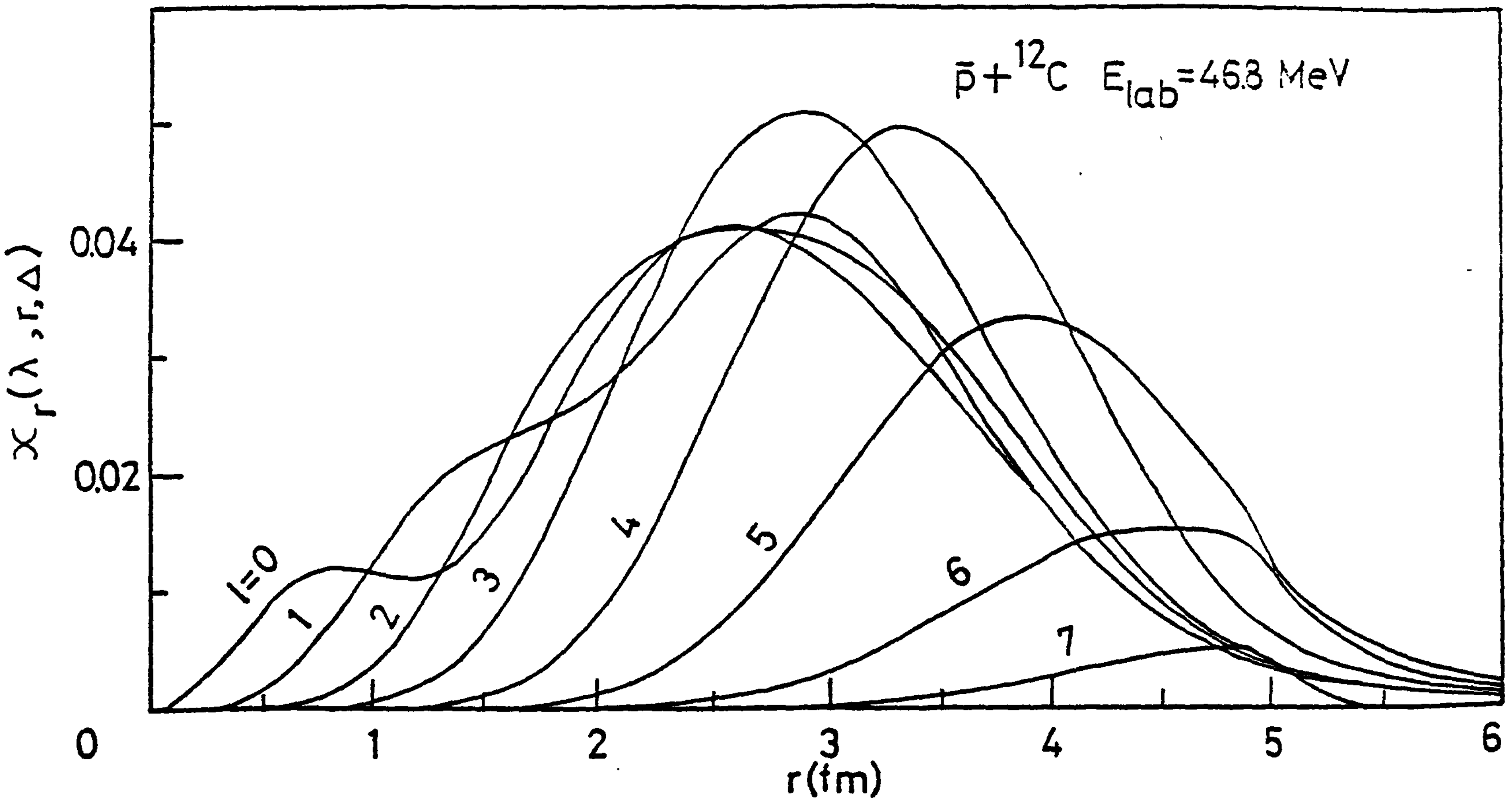

Fig.4.3.1 Radial variation of $\chi_r(\lambda,r,\Delta)$ for different l for $\bar{p}$ + ^{12}C scattering at E_{lab} = 46.8 MeV. The OM parameters used in the calcualtions are given in Table 4.3.1. Δ = 0.1 fm.

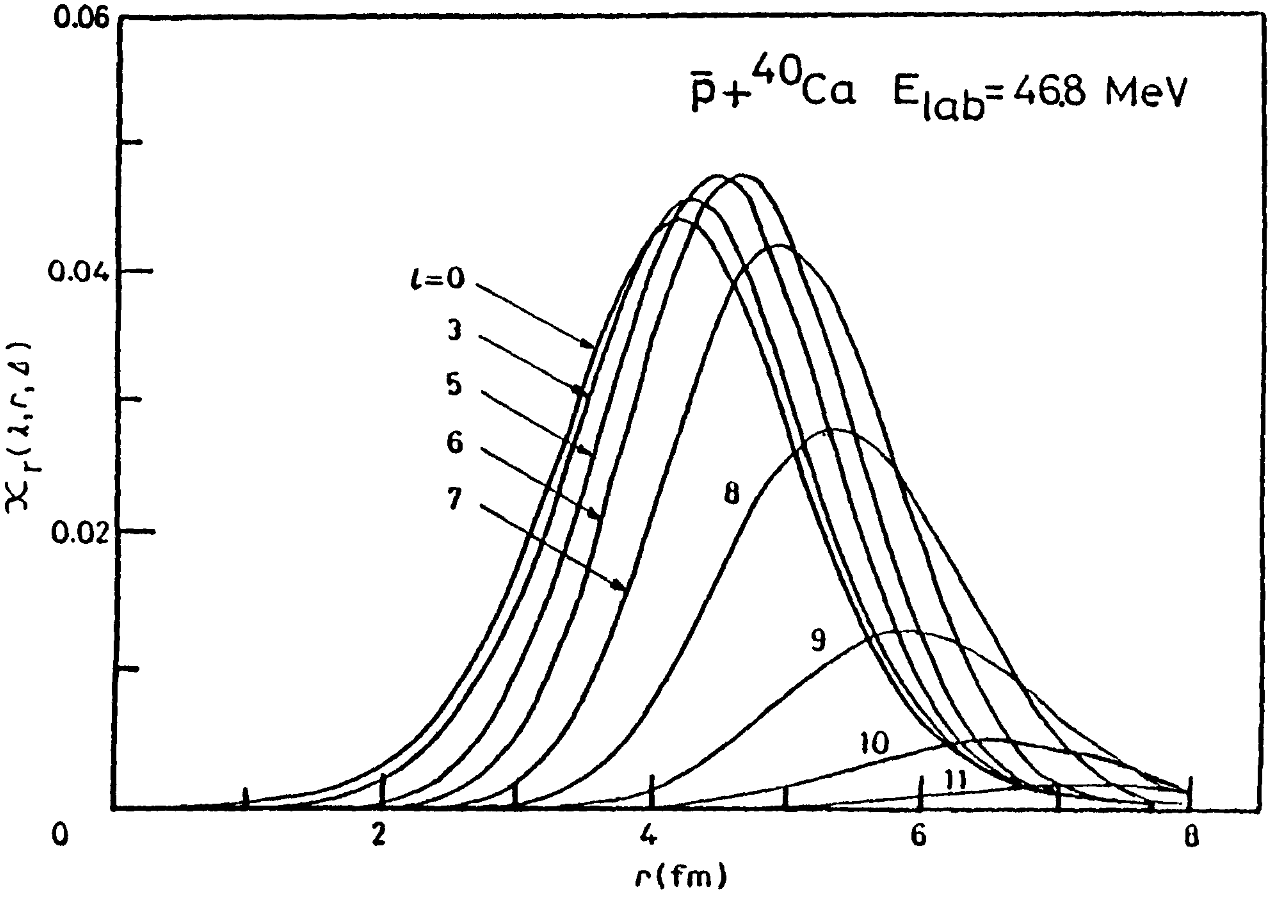

Fig.4.3.2 Same as Fig.4.3.1 for $\bar{p}$ + ^{40}Ca at E_{lab} = 46.8 MeV.

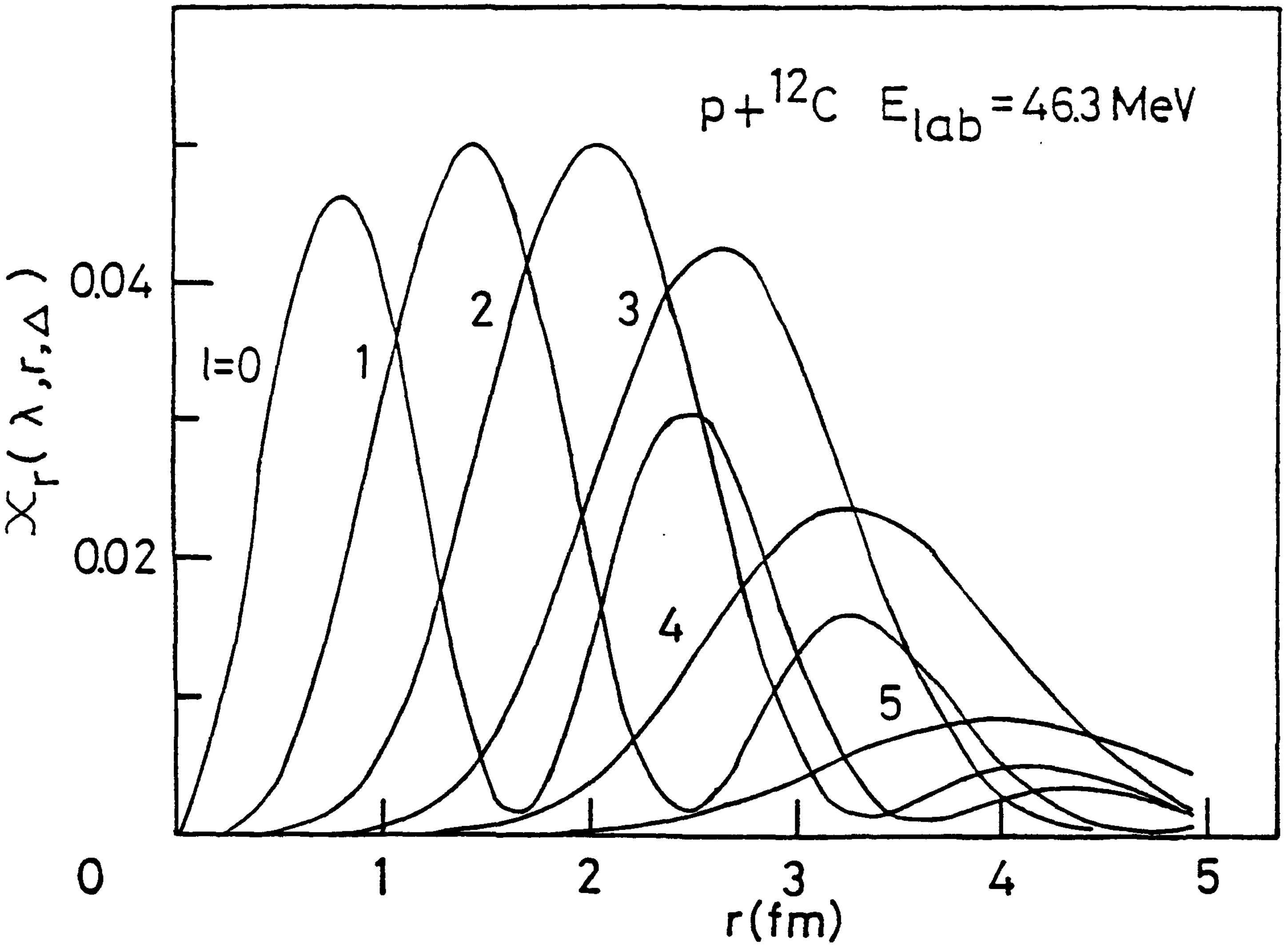

Fig.4.3.3 Same as Fig.4.3.1 for p + ^{12}C at E_{lab} = 46.3 MeV.

that in the case of proton-nucleus scattering, the entire region of the nuclear potential takes part in generating the contribution to $(1-\eta_l^2)$. The oscillatory nature of $\chi_r(\lambda,r,\Delta)$ (Fig.4.3.3) indicates that in some regions its contribution is less whereas in others it is more. Comparison of Figs. 4.3.1 and 4.3.2 with Fig. 4.3.3 illustrates the nature of surface dominance of $\bar{p}$-A scattering in contrast to p-A scattering for different partial waves. The cumulative effect of all the partial waves within the region $r_1 \leq r \leq r_1+\Delta$ is shown in Figs. 4.3.4 and 4.3.5 for $\bar{p}+{}^{12}C$ and $\bar{p}+{}^{40}Ca$ scattering systems at E_{lab}= 46.8 MeV respectively, where the nature of variation of $\sigma_r(r,\Delta)$ with r is depicted. It is also observed that when one uses different, but equivalent optical potentials, the general behaviour of $\sigma_r(r,\Delta)$ as a function of r remains practically same. To confirm the case we have chosen another set of equivalent optical model potential parameters at the same incident energy for $\bar{p}+{}^{12}C$ scattering system (for example, E_{lab} = 46.8 MeV, V_0= 90 MeV, W_0= 108.9 MeV etc. as mentioned in Table 4.3.1) and the trend of the function $\sigma_r(r,\Delta)$ calculated using this new set of parameters is shown graphically in Fig.4.3.6. Hence, we conclude that Figs. 4.3.4 and 4.3.5 represent the general pattern of region-wise absorption in $\bar{p}$-A scattering. These figues show that the maximum absorption occurs at $r=R_m$= 3.4 fm for $\bar{p}+{}^{12}C$ (Fig.4.3.6) and r = R_m= 4.61 fm for $\bar{p}+{}^{40}Ca$, where R_m represents the peak position. In Fig.4.3.5, we have also shown the corresponding results (i.e., $\sigma_r(r,\Delta)$) for p + ${}^{12}C$ scattering at E_{lab} = 46.3 MeV. The variation of $\left[\sigma_r\right]_0^r$ with r is also depicted in Figs. 4.3.4 - 4.3.6. In our analysis, we have

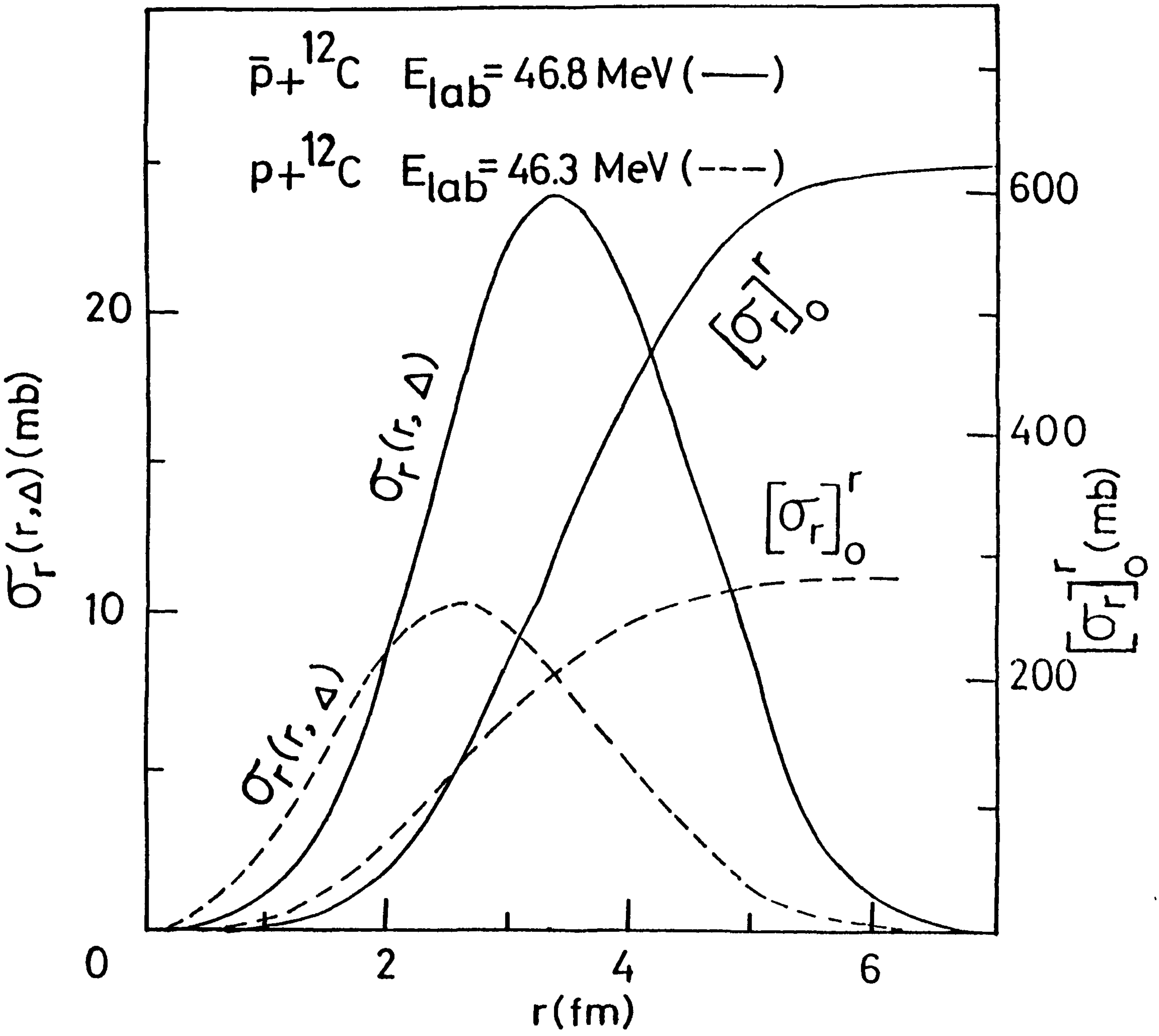

Fig.4.3.4 Variation of $\sigma_r(r,\Delta)$ and $\left[\sigma_r\right]_0^r$ as a function of r. The solid curves (——) represent $\bar{p}$ + ^{12}C scattering at E_{lab} = 46.8 MeV and dashed curves (----) represent p + ^{12}C scattering at E_{lab} = 46.3 MeV. The OM potential parameters are listed in Table 4.3.1. Δ = 0.1 fm.

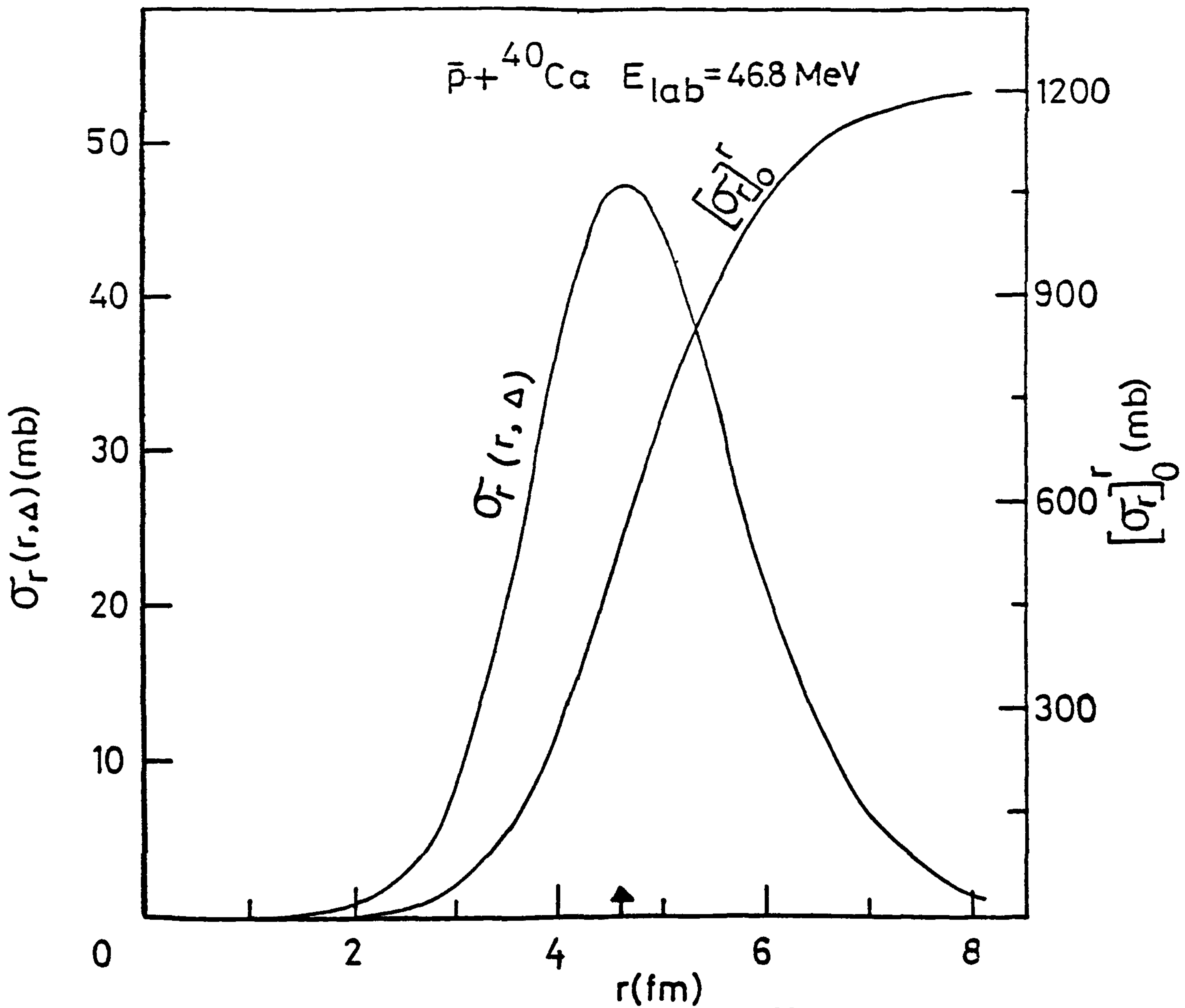

Fig.4.3.5 Same as Fig.4.3.4 for $\bar{p}$ + ^{40}Ca scattering at E_{lab} = 46.8 MeV. Arrow indicates the position of maximum absorption.

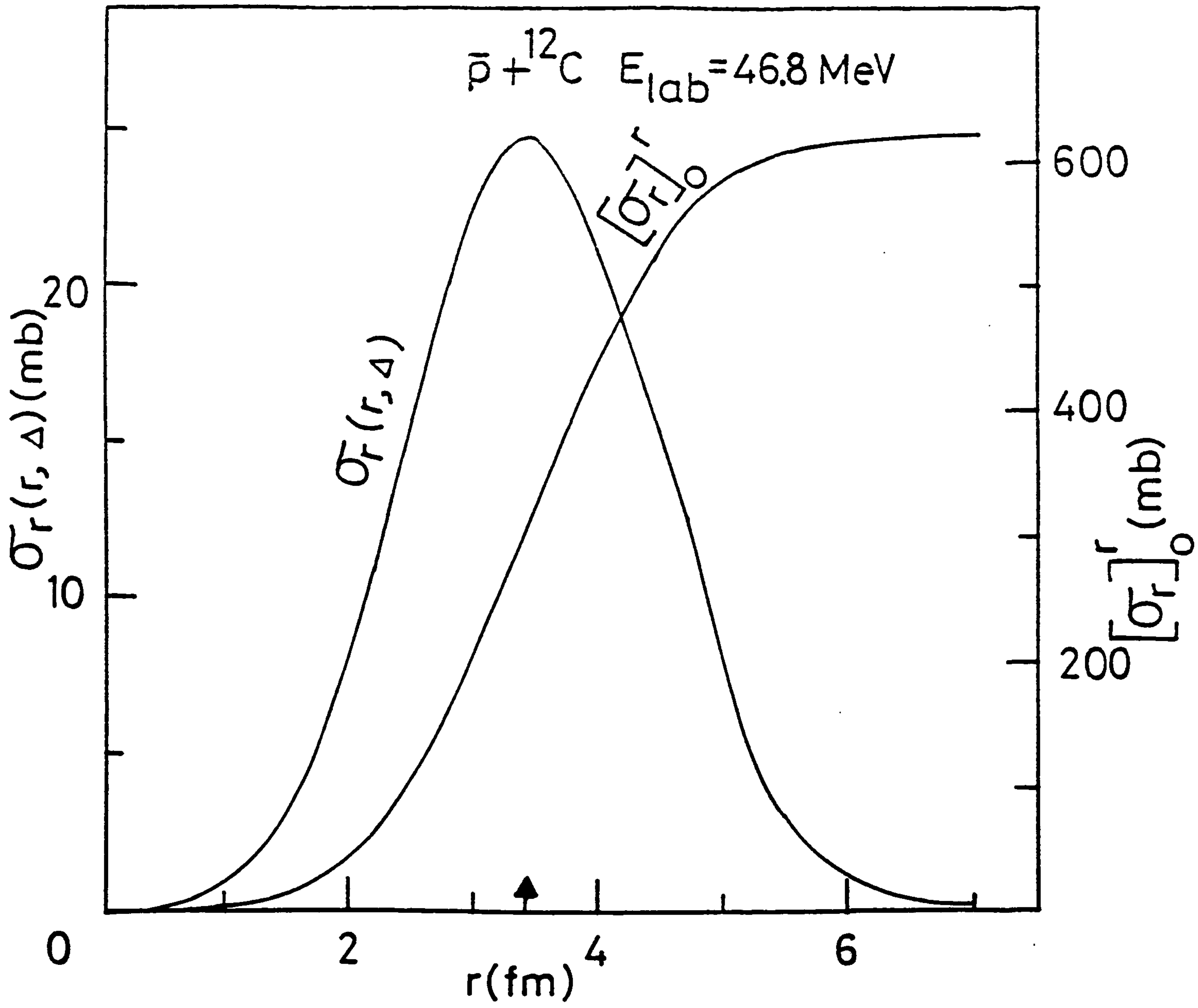

Fig.4.3.6 Same as Fig.4.3.4 for $\bar{p}$ + ^{12}C scattering at E_{lab} = 46.8 MeV. Arrow indicates the position of maximum absorption.

used Δ=0.1 fm in all cases. Here it is worth mentioning that the results of $\bar{p}$–A scattering can be compared with the corresponding results of HIS namely, $^{18}O + ^{58}Ni$ scattering at E_{lab}= 60 MeV. It has been shown that [Sh 84] for nucleus-nucleus scattering case, even if one takes volume absorptive potential, the contribution to absorption cross section from the surface region is more significant than from the interior region of the nuclear potential.

The radial variations of $\chi_r(\lambda,r,\Delta)$ for different l values and $\sigma_r(r,\Delta)$ within the region $(r,r+\Delta)$ are shown in Figs. 4.3.7 and 4.3.8 respectively for the case of $^{18}O + ^{58}Ni$ at E_{lab}= 60 MeV [Sh 83, Sh 84]. Variation of reaction cross section $\left[\sigma_r\right]_0^r$ is also shown in Fig. 4.3.8. In all cases $\left[\sigma_r\right]_0^r$ saturates to the reaction cross section σ_r for large r. The optical model potential parameters used in the calculation for $^{18}O + ^{58}Ni$ at E_{lab} = 60 MeV is also given in Table 4.3.1. Assimilating the previous work on HIS as well as the present work on various $\bar{p}$–A scattering systems we conclude that in both the cases reaction cross section data are insensitive to the interior region of interaction potential. Thus there is a close similarity between region-wise absorption in $\bar{p}$–A scattering and nucleus-nucleus scattering. Our results indicate that surface absorption is rather symmetrically distributed around the peak position R_m in the cases of $\bar{p} + ^{12}C$ and $\bar{p} + ^{40}Ca$ scattering systems. It may be noted that elastic scattering cross section data as such may not be useful in establishing conclusively the detailed nature of region-wise absorption. This is because, if a partial wave is fully absorbed, (i.e., $\eta_l = |S_l|$ =

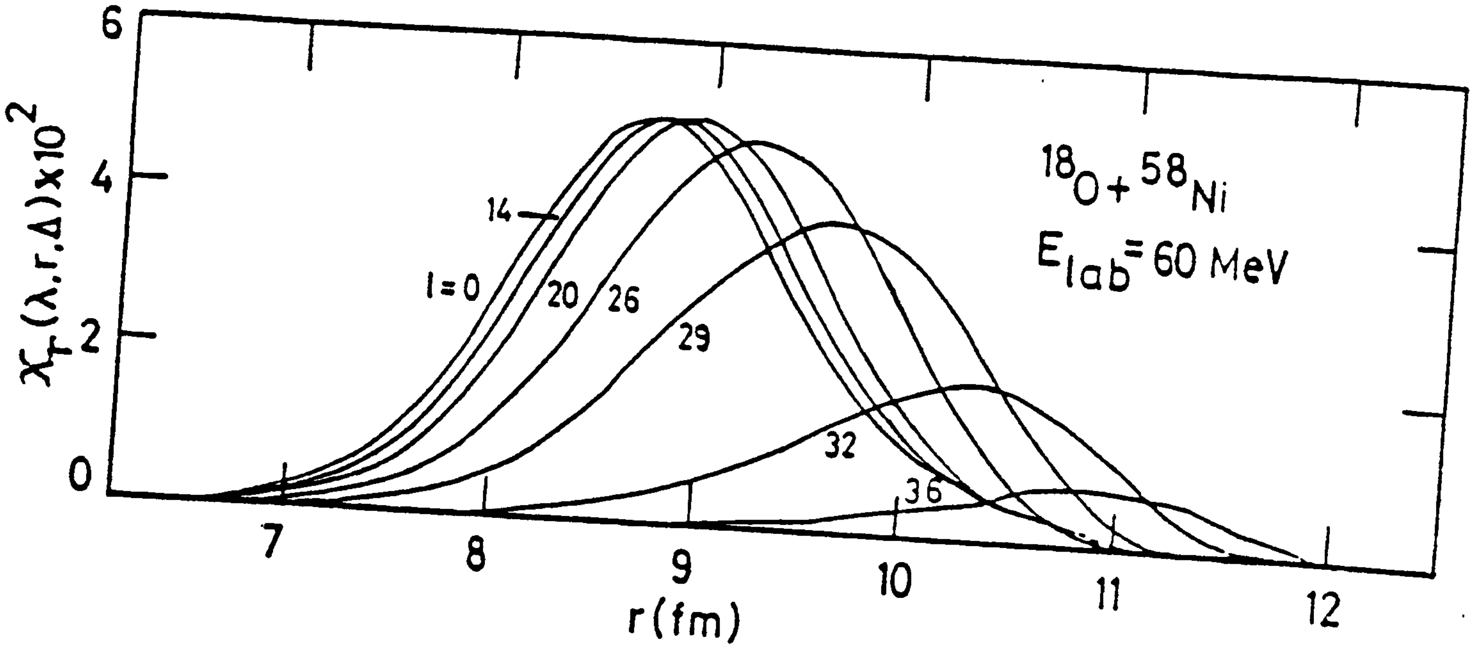

Fig.4.3.7 Same as Fig.4.3.1 for ^{18}O + ^{58}Ni at E_{lab} = 60 MeV. Δ = 0.09 fm. OM potential parameters are listed in Table 4.3.1.

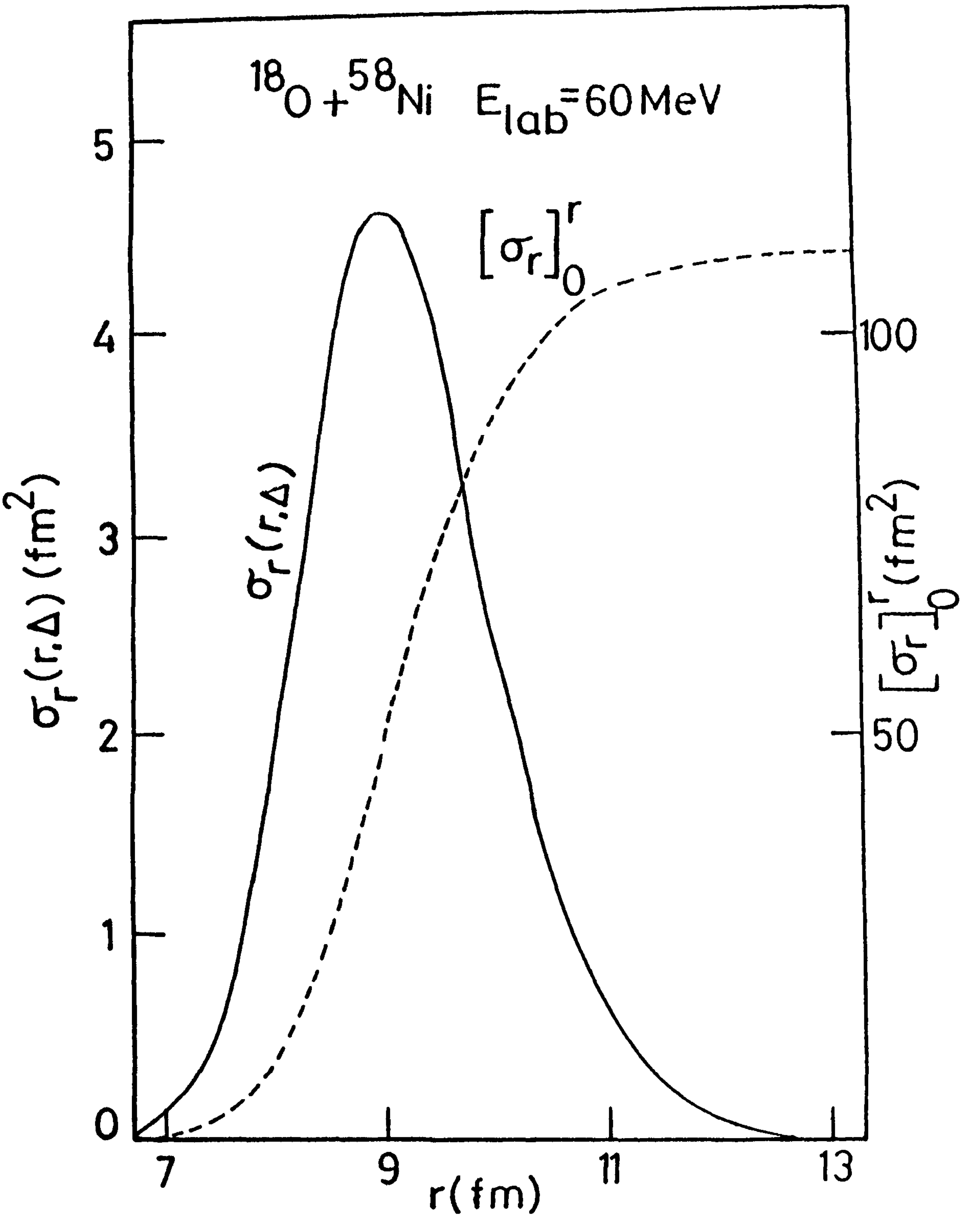

Fig.4.3.8 Same as Fig.4.3.4 for $^{18}O + ^{58}Ni$ at E_{lab} = 60 MeV. Δ = 0.09 fm.

0) it as such cannot give the details of the interaction region except its absorptive nature. For example, in the strong absorption model where $S_l = 0$ for $l \leq l_0$, one does not have any information regarding the details of absorption process. Using an optical potential one can always get the region-wise absorption. Such an information is useful if one has information regarding the cross section from the dominant channel like $\sigma^{\bar{p}A}_{ann}$ in addition to σ_r and differential scattering cross section. In such cases one can expect to get more details of $\bar{p}$-A interaction in different regions. An analogous situation is present in HIS as described below.

It is well known that HIS data are sensitive to the surface region of the potential, but recently some [Ud 85] procedures have been developed to understand the relative importance and the nature of the imaginary part of the potential from the fusion cross section data. In the vicinity of the Coulomb barrier one can write σ_r in HIS as

$$\sigma_r = \sigma_F + \sigma_S \ , \qquad (4.3.2)$$

where σ_F denotes the fusion cross section and σ_S denotes the cross section for other processes. Recently, a quite successful direct reaction model of fusion [Ud 85] has been developed which states that contribution to fusion reaction is from the region $r < R_F$, R_F being the fusion radius, which is of the order $R_F \simeq 1.4\times(A_P^{1/3} + A_T^{1/3})$ fm. Here A_P and A_T are the projectile and target mass numbers, respectively. Since, in HIC, fusion cross section data are available in addition to reaction and scattering cross section data, the direct reaction model of fusion helps us in understanding the potential, in particular its imaginary part, in the region $r < R_F$. Interestingly a somewhat analogous situation can be visualised in $\bar{p}$-A scattering. Annihilation being the most dominant channel in $\bar{p}$-A scattering, it wil be useful to write σ_r as

$$\sigma_r = \sigma_{ann}^{\bar{p}A} + \sigma_S , \qquad (4.3.3)$$

where $\sigma_{ann}^{\bar{p}A}$ represents the annihilation cross section inside the nucleus and σ_S is the contribution to reaction cross section from other channels. An important parameter, which is known in the literature as annihilation radius, characterises the range of annihilation. With the appearance of experimental data for $\bar{p}$-p cross sections, different cross sections like annihilation, charge exchange and elastic scattering, for $\bar{p}$-p collision were analysed by Shibata [Sh 87] between 180 - 600 MeV/c using a potential model. The result of his analysis indicates that the mean free path associated with $\bar{p}$-p collision is less than 2 fm and annihilation is peaked around 1fm. He has also anticipated that charge exchange reaction can extend upto 4 fm. It is also known that [Go 88] the average distance between nucleons in a nucleus is $\approx$ 1.3 fm. In view of these facts we have computed the mean free path Λ using the formula [Gr 68]

$$\Lambda = -\hbar^2 k/[2\mu W_I(r)] \qquad (4.3.4)$$

The radial positions R_1 and R_2 where the mean free paths are $\approx$ 1 fm and $\approx$ 2 fm, respectively are found out for different $\bar{p}$-A systems. In Table 4.3.2 we have given the positions R_1 and R_2 for $\bar{p}$ + ^{12}C and $\bar{p}$+ ^{40}Ca at E_{lab}= 46.8 MeV. It is interesting to note that the peak of region-wise absorption also occurs at r very

Table 4.3.2 Various radius parameters r_1, r_2 and r_s for three $\bar{p}$-A systems and contribution to σ_r from the regions $0 \le r \le R_2$ and $0 \le r \le R_s$ obtained from Figs. 4.3.4–4.3.6. $R_1 = r_1 A_T^{1/3}$, $R_2 = r_2 A_T^{1/3}$ and $R_s = r_s A_T^{1/3}$. R_1 and R_2 signify the distances at which the mean free paths Λ are about 1 fm and 2 fm respectively.

Systems	$\bar{p}$ + ^{12}C	$\bar{p}$ + ^{12}C	$\bar{p}$ + ^{40}Ca
E_{lab} (MeV)	46.8	46.8	46.8
$R_1(r_1)$ (fm)	2.8(1.223)	2.65(1.158)	4.25(1.243)
$R_2(r_2)$ (fm)	3.35(1.463)	3.30(1.442)	4.80(1.404)
$R_s(r_s)$ (fm)	3.65(1.59)	3.65(1.59)	5.30(1.55)
R_m (fm)	3.4	3.35	4.61
$\left[\sigma_r\right]_0^{R_2}$ (mb)	285	290	630
$\left[\sigma_r\right]_0^{R_s}$ (mb)	355	360	853
Remarks	Fig.4.3.6	Fig.4.3.4	Fig.4.3.5

close to $r = R_2$ where $\Lambda \simeq 2$ fm. If we conjecture that annihilation is the most predominant process in the region $r < R_2$, then we find that, the contribution of annihilation to σ_r is at least 50% in all cases. However, in a recent work [He 87] it has been shown that the probability of annihilation substantially increases inside the nuclear medium. Hernández and Oset [He 87] have shown that as $\bar{p}$ enters the nucleus annihilation cross section increases significantly. The result of their work shows that even at very low nuclear density annihilation cross section is enhanced substantially and large $\bar{p}$-N annihilation gives an idea that most of the annihilation occurs at the nuclear periphery. Based on this fact one can also expect that the contribution of $\sigma^{\bar{p}A}_{ann}$ to σ_r may be higher than 50% of σ_r. Using several alternative methods, they have evaluated $\sigma^{\bar{p}A}_{ann}$ for $\bar{p}+{}^{12}C$ system at $E_{lab} = 175$ MeV. Their estimate gives $\sigma^{\bar{p}A}_{ann}$ to be 350 mb to 450 mb whereas the experimental value is 422±25 mb. Our result, based on the mean free path of $\bar{p}$ inside the nucleus and region-wise absorption, indicates that $\sigma^{\bar{p}A}_{ann}$ should be more than 50% of σ_r if R_2 R_m. It will be of interest to have a precise measurement of $\sigma^{\bar{p}A}_{ann}$ in addition to σ_r. This will indicate whether there is substantial contribution to the annihilation cross section in the region $r <$ R_2 and whether considerable $\bar{p}$ annihilation can take place inside the nucleus even when $\Lambda > 2$ fm. In Table 4.3.2 we also give $\left[\sigma_r\right]_0^{R_2}$ and $\left[\sigma_r\right]_0^{R_s}$, i.e., the respective contribution to σ_r from the regions $0 \leq r \leq R_2$ and $0 \leq r \leq R_s$ where $R_s = r_s A_T^{1/3}$ is the strong absorption radius. R_s for different systems [Ja 86] is also given in the Table 4.3.2. Since in the region r R_2, Λ 2 fm, $\left[\sigma_r\right]_0^{R_2}$

gives a measure of $\sigma_{ann}^{\bar{p}A}$ in $\bar{p}$-A collision. It should be noted that if the $\bar{p}$-p annihilation distance inside the nucleus can be proved to be significantly larger than 2 fm, the estimates of $\sigma_{ann}^{\bar{p}A}$ by our method will be larger. For example, in the case of $\bar{p}$ $+^{12}C$ scattering at E_{lab}= 46.8 MeV (Fig.4.3.6) at $r = R_s$, Λ = 3.13 fm and $\left[\sigma_r\right]_0^{R_s}$ = 355 mb which is substantially larger than $\left[\sigma_r\right]_0^{R_2}$ = 285 mb.

4.4 Interaction time

The time scale plays a very important role in the detailed understanding of fusion process in HIC [Sa 88]. The time is estimated in a number of ways from different view points. Scalia [Sc 86] estimated the interaction time involved in the fusion process of HIC along the classical Coulomb trajectory. He estimated the time within the region where the process of fusion takes place. But it is more sensible if one incorporates the nuclear potential into it and then estimates the time spent by the system along the classical Coulomb-nuclear trajectory. The time spent along the classical trajectory within the region $r_{min} < r < R$ is given by

$$T = 2\int_{r_{min}}^{R} dr/\dot{r}, \tag{4.4.1}$$

where r_{min} is the distance of closest approach, where kinetic energy vanishes. In the case of Coulomb trajectory the time (T_c) spent is

$$T_c = \sqrt{2\mu}\int_{r_{min}}^{R} \frac{dr}{\left[E - V_c(r) - V_l(r)\right]^{1/2}}, \tag{4.4.2}$$

whereas the presence of short range potential modifies the denominator of Eq. (4.4.2) and consequently the time elapsed along the Coulomb-nuclear trajectory is

$$T_{CN} = \sqrt{2\mu} \int_{r'_{min}}^{R} \frac{dr}{\left[E-V_C(r)-V_R(r)-V_l(r)\right]^{1/2}} \, . \qquad (4.4.3)$$

Here only the real part of the nuclear potential is considered. Using the above expression fusion time above the barrier was estimated [Sa 88] for a number of pairs of nuclei at various energies. The estimation shows that the fusion formation time above the barrier along the classical Coulomb-nuclear trajectory is of the order of 10^{-22}- 10^{-21}s. It is also known that in $\bar{p}$-p collision, the time scale involved is of the order of $\tau_{\bar{p}p} =$ 5×10^{-24}s in free space. Thus to have an idea of the time in $\bar{p}$-A collision we have used the classical Coulomb-nuclear trajectory which $\bar{p}$ traverses as it passes through the nucleus. Use of this classical picture for the estimation of time is not unreasonable because in $\bar{p}$-A collision, semiclassical description is found to be valid. Using classical Coulomb-nuclear trajectory, we have estimated the time $\tau_{\bar{p}A}$ which $\bar{p}$ spends inside the region $r \leq R_C = r_C A_T^{1/3}$, where R_C is the Coulomb radius. Using Eq. (4.4.3) we can write $\tau_{\bar{p}A}$ as

$$\tau_{\bar{p}A} = \sqrt{2\mu} \int_{r'_{min}}^{R_C} \frac{dr}{\left[E-V_C(r)-V_R(r)-V_l(r)\right]^{1/2}} \, . \qquad (4.4.4)$$

We have evaluated the interaction time $\tau_{\bar{p}A}$ for a variety of target nuclei at various energies. The nuclear potential used in our analysis is of Woods-Saxon type. The parameters for different systems are also contained in Table 4.3.1. In Fig. 4.4.1 we have shown the variation of the time estimated for the systems $\bar{p}+^{12}C$, $\bar{p}$

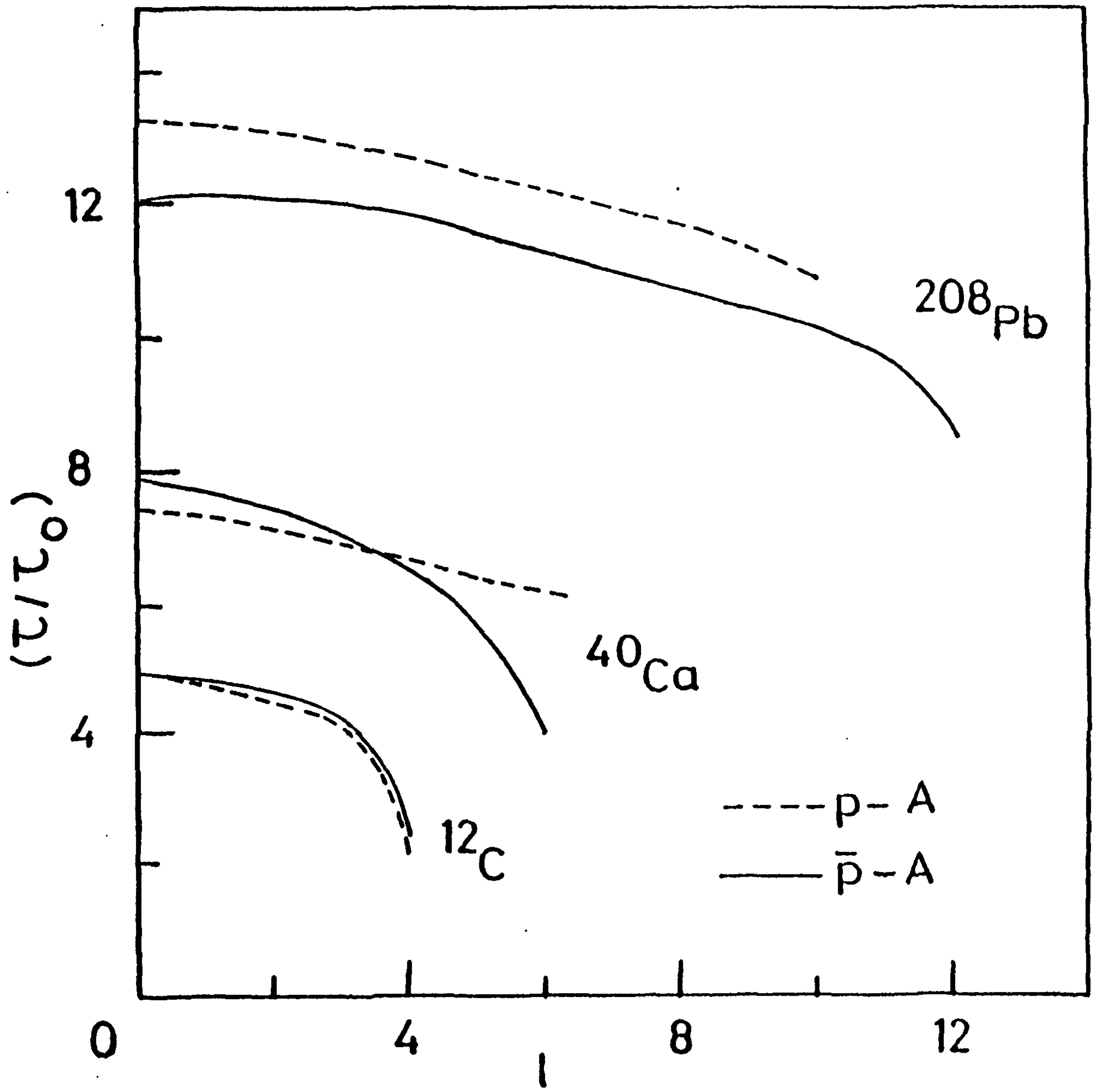

Fig.4.4.1 Variation of τ/τ_0 with l for $\bar{p}$ + ^{12}C, $\bar{p}$ + ^{40}Ca and $\bar{p}$ + ^{208}Pb at 46.8 MeV, 47.8 MeV and 47.9 MeV (all shown by solid curves (——)). Dashed curves (----) represent the results for the corresponding proton systems at the same energies. OM potential parameters are listed in Table 4.3.1. $\tau_0 = 10^{-23}$ s.

+ ^{40}Ca and $\bar{p}$ + ^{208}Pb at incident energy $E_{lab} \approx 47$ MeV for a number of partial waves. Figure 4.4.2 shows the results for the same $\bar{p}$-A systems at a higher incident energy ,i.e., at $E_{lab} \simeq 180$ MeV. The fusion time of a typical HIC namely, $^{81}Br + ^{90}Zr$ at $E_{lab} = 315.02$ MeV is also shown in Fig. 4.4.2 for comparision purpose. The estimated time increases marginally by about 10% if one uses R_2 instead of R_c. Figure 4.4.1 also shows the interaction times within the region r R_c for the corresponding p-A collisions at the same incident energy as that of $\bar{p}$-A collisions. It is interesting to note that the time obtained for $\bar{p}$-A system is practically same as those obtained for p-A system although the proton encounters a Coulomb barrier. Figure 4.4.3 depicts the interaction time for $\bar{p}$ + ^{40}Ca system at $E_{lab} = 179.8$ MeV using three different equivalent optical potential parameters. A close examination of the results of Figs. 4.4.1 – 4.4.3 leads to the following conclusions:

(i) The time scale involved in $\bar{p}$-A collision is approximately in the range 10^{-23}-10^{-22}s whereas in heavy ion fusion it is of the order of 10^{-21}s.

(ii) The time spent by the Coulomb-nuclear trajectories corresponding to different partial waves for a particular system at a particular energy are same except in the case of peripheral partial waves where they gradually fall off. This case is very similar to that of HIC for the partial waves which are significantly smaller than the grazing one.

(iii) From Fig. 4.4.3 one can conclude that the Coulomb-nuclear

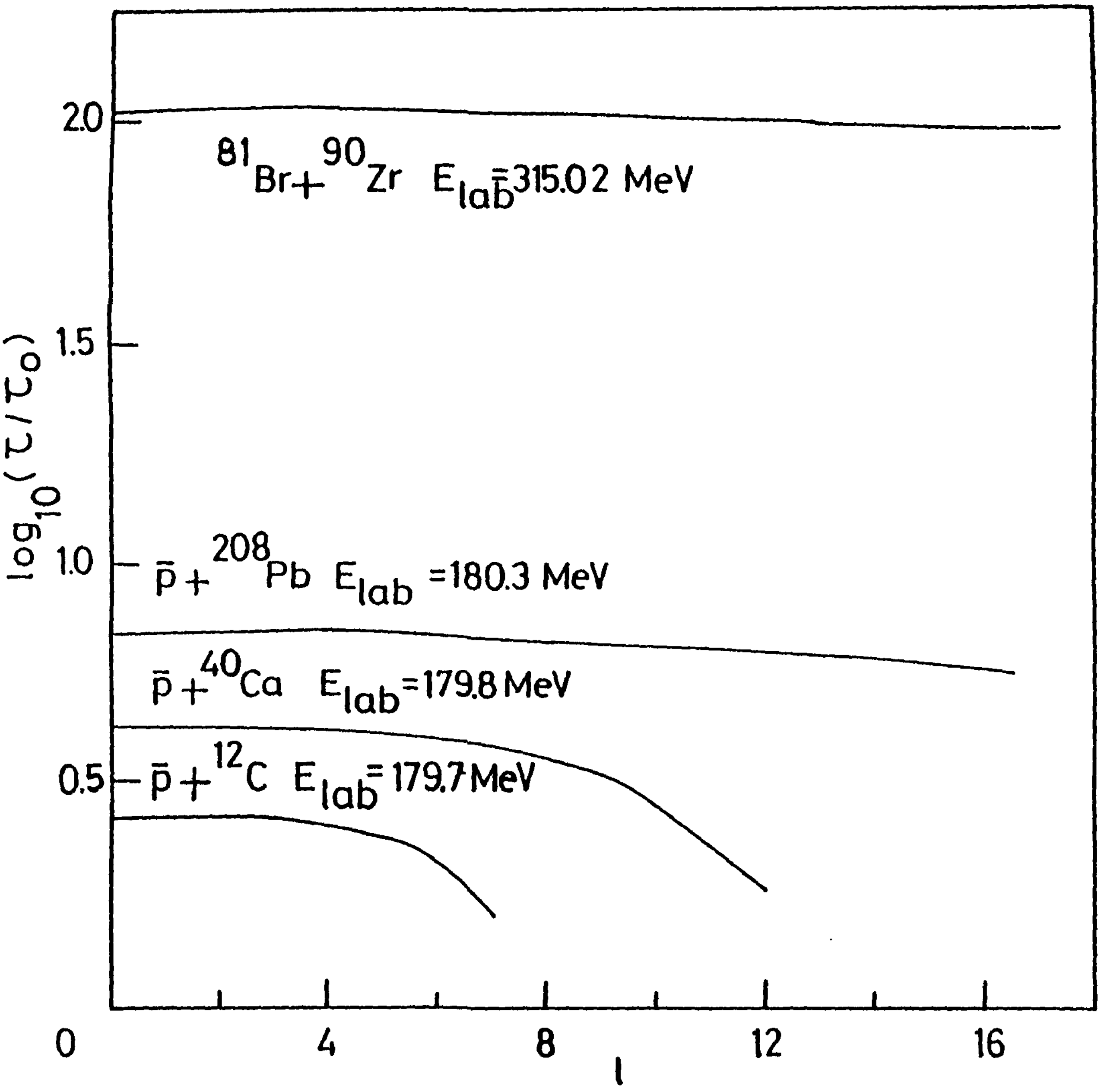

Fig.4.4.2 Variation of $\log(\tau/\tau_0)$ with l for $\bar{p}$ + ^{12}C, $\bar{p}$ +^{40}Ca, $\bar{p}$ + ^{208}Pb and ^{81}Br + ^{90}Zr at 179.7 MeV, 179.8 MeV, 180.3 MeV and 315.02 MeV respectively. OM potential parameters are listed in Table 4.3.1. $\tau_0 = 10^{-23}$ s.

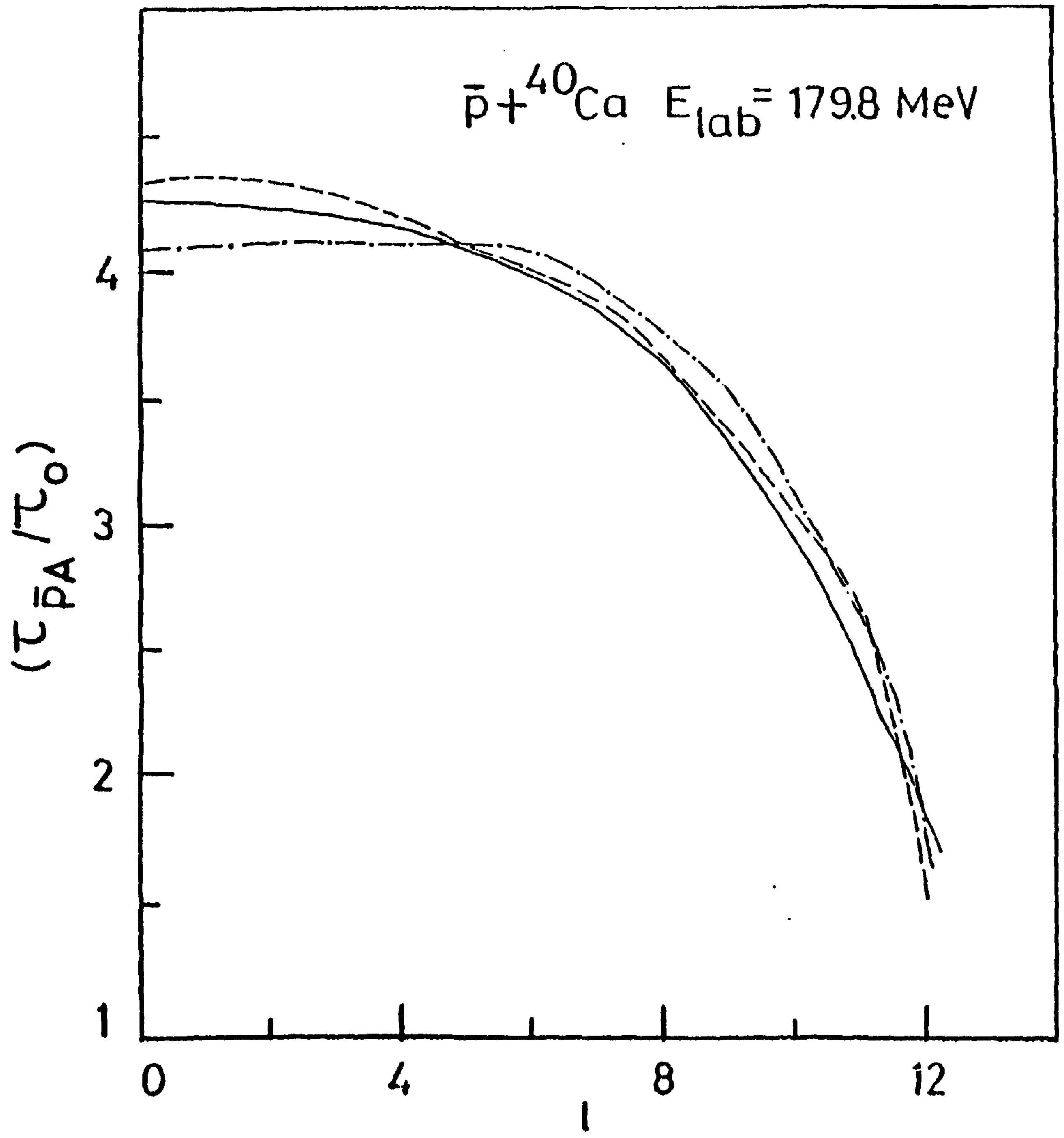

Fig.4.4.3 Variation of $\tau_{\bar{p}A}/\tau_0$ with l for $\bar{p}$ + ^{40}Ca at E_{lab} = 179.8 MeV for three equivalent optical potentials listed in Table 4.3.1. Solid curve (——), dashed curve(– – – –) and dash-dot-dashed (—•—) curve are obtained by using OM parameters represented by (a), (b) and (c) respectively in Table 4.3.1.

trajectory time obtained for a given system using different optical potentials which fit the scattering data are practically same.

(iv) At approximately the same bombarding energy the time spent by $\bar{p}$ in the Coulomb-nuclear trajectory increases by a factor of 2.5 with the increase of mass number of the target from 12 to 208.

Assuming that $\bar{p}$ gets annihilated before it reaches the inner most point in the classically allowed trajectory, we can compare $\bar{p}$-p annihilation time in free space (which is $\tau_{\bar{p}p} = 5\times10^{-24}$s) with the time required to reach the innermost turning point. Denoting the time spent by $\bar{p}$ along the classical Coulomb-nuclear trajectory within the region of strong absorption radius by τ_{R_s}, we assume $\tau_{R_s}/2$, as the time to reach the innermost turning point. Similarly one can compare the reaction cross section σ_r in $\bar{p}$-A collision with the free space $\bar{p}$-p annihilation cross section $\sigma_{ann}^{\bar{p}p}$. In Table 4.4.1 we have summarised these results for three systems $\bar{p}$ + ^{12}C, $\bar{p}$ + ^{40}Ca and $\bar{p}$ + ^{208}Pb at the bombarding energy $E_{lab} \simeq 47$ MeV. In Table 4.4.1, in order to give an idea of various orders of magnitude we have listed $\sigma_r/\sigma_{ann}^{\bar{p}p} A_T^{2/3}$. The approximate constancy of $\sigma_r/\sigma_{ann}^{\bar{p}p} A_T^{2/3}$ indicates that σ_r is proportional to the product of $\sigma_{ann}^{\bar{p}p}$ and the cross sectional area πR^2 of the target nucleus. It may be noted that the ratios $\sigma_r/\sigma_{ann}^{\bar{p}p}$ and $\tau_{R_s}/2\tau_{\bar{p}p}$ have similar order of magnitude.

Table 4.4.1 The ratios $\sigma_r/\sigma_{ann}^{\bar{p}p}$ and $\tau_{R_s}/2\tau_{\bar{p}p}$ for various systems. $\sigma_{ann}^{\bar{p}p} \simeq 153$ mb and $\tau_{\bar{p}p} = 5 \times 10^{-24}$ s.

System	E_{lab} (MeV)	σ_r (mb)	$\sigma_r/\sigma_{ann}^{\bar{p}p}$	$\sigma_r/\sigma_{ann}^{\bar{p}p} A_T^{2/3}$	$\tau_{R_s}/2\tau_{\bar{p}p}$
$\bar{p} + {}^{12}C$	46.8	642	4.22	0.805	6.4
$\bar{p} + {}^{40}Ca$	46.9	1210	7.91	0.676	9.1
$\bar{p} + {}^{208}Pb$	47.9	3321	21.70	0.618	13.0

4.5 Conclusion

In the present work we have shown that in the case of $\bar{p}$-A collision dominant contribution to σ_r comes from the surface region which is peaked around R =3.4 fm and R = 4.61 fm for $\bar{p}$ +^{12}C (Fig. 4.3.6) and $\bar{p}$ + ^{40}Ca at E_{lab}=46.8 MeV, respectively. These correspond to the radius parameters 1.485 fm in the case of ^{12}C and 1.348 fm in the case of ^{40}Ca. From Figs. 4.3.6 and 4.3.5 one finds that the absorption peak of $\sigma_r(r,\Delta)$ has a width which is of the order of 2.4 fm for ^{12}C and 2.3 fm for ^{40}Ca. It is interesting to note that the peak of absorption occurs at a region where mean free path is about 2 fm which is the order of distance required in $\bar{p}$-p annihilation. Assuming that the contribution to σ_r from the region r R_2 and $R_2 > R_m$ is predominantly due to annihilation, we conclude that $\sigma^{\bar{p}A}_{ann}$ should be more than 50% of σ_r. This is consistent with the results of Hernández and Oset [He 87] who obtained $\sigma^{\bar{p}A}_{ann}$ in the range 350 - 450 mb whereas experimental cross section is 422 ± 25 mb. Further, the time spent by $\bar{p}$ inside the nucleus in the region $r < R_c$ is estimated using classical Coulomb-nuclear trajectory. In brief, we have found that $\tau_{\bar{p}A}$ is of the order of $2.4\tau_0 - 4.99\tau_0$ for $\bar{p}$+ ^{12}C at E_{lab}=46.8 MeV, $4.1\tau_0-7.9\tau_0$ for $\bar{p}$+ ^{40}Ca at E_{lab}=47.9 MeV and $2.9\tau_0- 12\tau_0$ for $\bar{p}$+ ^{208}Pb at E_{lab}=47.9 MeV, where $\tau_0=10^{-23}$s. This time is practically same for different partial waves except for peripheral partial waves. Assuming $\tau_{R_s}/2$ to be the time spent by $\bar{p}$ inside the nucleus before annihilation takes place, we find that the ratios $\sigma_r/\sigma^{\bar{p}p}_{ann}$ and $\tau_{R_s}/2\tau_{\bar{p}p}$ are of the same order. If experimentally obtained $\sigma^{\bar{p}A}_{ann}$ is substantially larger than $\sigma_r/2$, it would imply that $\bar{p}$-p annihilation can take place inside the nucleus even when $\bar{p}$-p separation distance is more than 2 fm. This will be in conformity with the conclusion of Ref. [He 87] that $\bar{p}$ annihilation probability increases substantially inside the nucleus.

Reference

[Ab 64] Abramowitz. M and Stegun. I.A, *Handbook of mathematical functions* (New York, Dover 1964) p.504

[Ai 81] Aihara. H et al., Nucl.Phys. **A360** (1981) 291

[As 85] Ashford. V et al., Phys.Rev. **C31** (1985) 663

[Be 69] Becchetti. Jr.F.D and Greenlees. G.W , Phys.Rev. **182**(1969) 1190

[Br 83] Braun-Munzinger. P and Berkowitz. G.M, Phys.Lett. **125B**(1983) 19

[Co 84] Cohn. H.O, Phys.Rev. **C29** (1984) 332

[De 65] De Alfaro. V and Regge. T, *Potential scattering* (North Holland Publishing Co., Amsterdam 1965) p.34

[De 88] Dey. B, Shastry. C. S and Roy. T.K, Pramāna – J.Phys. **31**(1988) 173

[Ga 84] Garreta. D et al.. Phys.Lett. **135B**(1984) 266

[Ga 84a] Garreta. D et al., Phys.Lett. **149B**(1984) 64

[Go 88] Golubeva. Ye.S, Iljinov. A. S, Botvina. A. S and Sobolevski. N. M, Nucl. Phys. **A483**(1988) 539

[Gr 68] Green. A.E.S, Sawada. T and Saxon. D.S *The nuclear independent particle model* (Academic Press, New York, London, 1968) p.148

[Gu 88] Gupta. R.C and Goel. S.P, Acta.Phys.Slov. **38**(1988) 321

[He 85] Heiselberg. H et al., Nucl.Phys. **A446**(1986) 637

[He 87] Hernández. E and Oset. E, Phys.Lett. **184B**(1987) 1

[In 86] Ingemarsson. A, Nucl.Phys. **A454**(1986) 475

[Ja 86] Janouin. S et al., Nucl.Phys. **A451**(1986) 541

[Jo 47] Jost. R, Helv.Phys.Acta. **20**(1947) 256

[Jo 75] Joachain. C.J, *Quantum collision theory* (Amsterdam, New York, 1975) p.243

[Ko 87] Ko. C.M and Yuan. R, Phys.Lett. **192B**(1987) 31

[Ku 85] Kubo. K.-I, Toki. H and Igarashi. M, Nucl.Phys. **A435** (1985) 708

[Na 84] Nakamura. K et al., Phys.Rev.Lett. **52**(1984) 731

[Ni 83] Niskanen. J.A and Green. A.M, Nucl.Phys. **A404** 1983) 495

[Ra 80] Rafelski. J, Phys.Lett. **91B**(1980) 281

[Sa 67] Satchler. G.R, Nucl.Phys. **A100**(1967) 497

[Sa 88] Sahu. B and Shastry. C. S, Phys.Rev. **C38**(1988) 1262

[Sc 86] Scalia. A, Nuovo.Cim. **92A**(1986) 210

[Sh 83] Shastry. C.S and Gambhir. Y.K, Phys.Rev. **C28**(1983) 1109

[Sh 84] Shastry. C.S and Gambhir. Y.K, Pramāna – J.Phys. **23**(1984) 175

[Sh 87] Shibata. T.A, Phys.Lett. **189B**(1987) 232

[Ud 85] Udagawa. T, Kim. B.T and Tamura. T, Phys.Rev. **C32**(1985) 124

[Vi 76] Videbaek. F, Christensen. P.R, Hansen. O and Ulbak. K, Nucl.Phys. **A256**(1976) 301

CHAPTER 5

FUSION CROSS SECTION OF HEAVY ION SYSTEM USING EFFECTIVE FUSION BARRIER TRANSMISSION MODEL

5.1 Introduction

The mechanism of fusion in the nucleus-nucleus collision is an important area of investigation in heavy ion physics. This is particularly so because it was anticipated that heavy ion collisions can generate superheavy nuclei by the process of fusion reaction. In the nucleus-nucleus fusion process, the projectile and target form a compound nucleus through the fusion process. There have been a number of models to explain the different features of fusion process. They range from simple liquid drop model and classical equations of motion to the solution of Schrodinger equation with several variables pertaining to fusion. A review of different approaches used to describe heavy ion collisions are discussed in references [Ba 80, Ng 86. Rh 86]. In the macroscopic approach one uses one-dimensional barrier penetration model (BPM) [Bi 83, Hi 53, Va 81] for sub-barrier fusion, i.e., fusion below the Coulomb barrier and a two-parameter (R_{cr}, V_B) formula [Br 85] $\sigma_F = \pi R_{cr}^2(1 - V_B/E)$ for above barrier case. In general, the former underestimates the fusion data in the sub-barrier region (this fact is generally referred as the sub-barrier enhancement) whereas the latter overestimates the data at higher energies. Further there seems to be no formulation of the barrier transmission type which explains the σ_F data both below and above the barrier height in a unified way. In order to have a better understanding of fusion process a simple macroscopic approach within the framework of BPM has been formulated recently by Sahu and Shastry [Sa 89]. This model called effective fusion barrier transmission (EFB) model is found to be quite successful in explaining the experimental fusion data over a wide range of energies around the Coulomb barrier. It has been realised that EFB model and direct reaction model (DRM) of Udagawa et al. [Ud 84, Ud 85] are two alternative ways of analysing fusion data. In the DRM one assumes that when the two interacting nuclei approaching each other, reach a distance $r \leq R_F$ ($R_F = r_F(A_P^{1/3}+A_T^{1/3})$) fusion can take place due to absorption in the fusion channel. This distance R_F is characterised as the fusion radius. Thus within the region $r \leq R_F$ fusion is governed by the imaginary part of the optical potential. On the other hand, in EFB model when the colliding nuclei come within the sphere of radius R_F, complete fusion will take place and in this connection R_F signifies the point-of-no-return for the incoming wave, which is consistent with the concept of incoming wave boundary condition model of Christensen and Switkowski [Ch 77]. Thus transmission into this region is the primary process involved in the fusion process. For transmission into this region it has to overcome the effective barrier for complete fusion to take place. One advantage of this model is that it uses only the surface region of the potential where the potential parameters are well determined which is in contrast to DRM. This model is quite justifiable because of the fact that fusion radius parameter r_F obtained in the present EFB model is practically same as that of DRM of Udagawa et al. [Ud 84, Ud 85]. The physical significance of r_F has also been discussed in Ref. [Sa 89]. In view of all these facts, we have further applied the EFB model to study several heavy ion fusion processes. In the following sections the theory of EFB model and its application to few heavy ion systems are discussed.

5.2 Theory of effective fusion barrier transmission model

In the simplest model for fusion it is assumed that at a given energy if the angular momentum l is less than some critical value l_{fu} ($l \leq l_{fu}$) then the fusion probability is unity and above the critical value ($l > l_{fu}$) fusion probability is zero. Thus in the sharp cut-off model (SCM) [Br 85] the fusion cross section is given in terms of critical radius R_{cr} and barrier height V_B and is written as

$$\sigma_F = \pi R_{cr}^2 (1-V_B/E) , \qquad E > V_B$$
$$= 0, \qquad E < V_B. \qquad (5.2.1)$$

This model overestimates the data at higher energies which is due to the fact that all reactions may not give rise to fusion process and below the barrier, fusion is classically forbidden and results in a zero cross section. Hence, for energies below the barrier which is also known as sub-barrier fusion, fusion is possible due to quantum mechanical barrier penetration. For fusion to take place in the sub-barrier region a model called barrier penetration model (BPM) is used [Bi 83, Hi 53, Va 81].

Very recently, within the framework of direct reaction model (DRM) [Ud 84, Ud 85] a modified barrier transmission model known as EFB model has been developed by Sahu and Shastry [Sa 89].

In the DRM, it has been assumed that fusion takes place due to the absorption of the flux which is governed by the imaginary part of the potential within the region $r \leq R_F = r_F(A_P^{1/3} + A_T^{1/3})$, where R_F characterises the fusion radius. Thus, the transmission into this sphere is the primary process involved in the fusion process. Thus the barrier which has to be overcome for transmission into this sphere is given by

$$\begin{aligned} V_{EFB}(l,r) &= V_N(r) + V_c(r) + V_l(r), \qquad && r \quad R_F \\ &= 0, && r \quad R_F \qquad (5.2.2) \end{aligned}$$

where $V_l(r) = \dfrac{\hbar^2\, l(l+1)}{2\mu r^2}$, μ being the reduced mass and $V_c(r)$ is the Coulomb potential between two interacting nuclei. $V_N(r)$ corresponds to the real part of the nuclear optical potential. The total effective potential $V_{eff}(l,r)$ is given by

$$V_{eff}(l,r) = V_N(r) + V_c(r) + V_l(r). \qquad (5.2.3)$$

Here the Woods-Saxon form of nuclear optical model potential (OMP) is chosen. The optical model potential parameters alongwith the Coulomb radius parameter r_c for various heavy ion systems are listed in Table 5.2.1. The parameters V_0, r_r and a_r represent the strength, radius and surface diffuseness parameters respectively, of the real part of the optical model potential . The imaginary part of the potential parameters are denoted by W_0, r_i and a_i. Variation of effective potential as a function of r for various partial waves is shown in Fig.5.2.1 for ^{58}Ni + ^{58}Ni system. The solid curve (———) corresponds to the EFB model and the dashed curve (----) is that of the total effective potential. The barrier

Table 5.2.1 Various parameters used in EFB model

System	V_0 (W_0) (MeV)	r_r (r_1) (fm)	a_r (a_1) (fm)	r_c (fm)	V_B^0 (MeV)	r_B (fm)	r_F (fm)	Reference OMP
$^{16}O+^{63}Cu$	58.52 (27.53)	1.22 (1.22)	0.57 (0.57)	1.22	31.97	1.510	1.45	[Fe 89]
$^{16}O+^{65}Cu$	54.76 (25.94)	1.22 (1.22)	0.57 (0.57)	1.22	31.93	1.503	1.45	[Fe 89]
$^{28}Si+^{58}Ni$	50.00 (10.00)	1.20 (1.20)	0.65 (0.65)	1.20	53.14	1.420	1.35	[St 87]
$^{28}Si+^{62}Ni$	50.00 (10.00)	1.20 (1.20)	0.65 (0.65)	1.20	52.55	1.427	1.38	[St 87]
$^{28}Si+^{64}Ni$	50.00 (10.00)	1.20 (1.20)	0.65 (0.65)	1.20	52.26	1.427	1.44	[St 87]

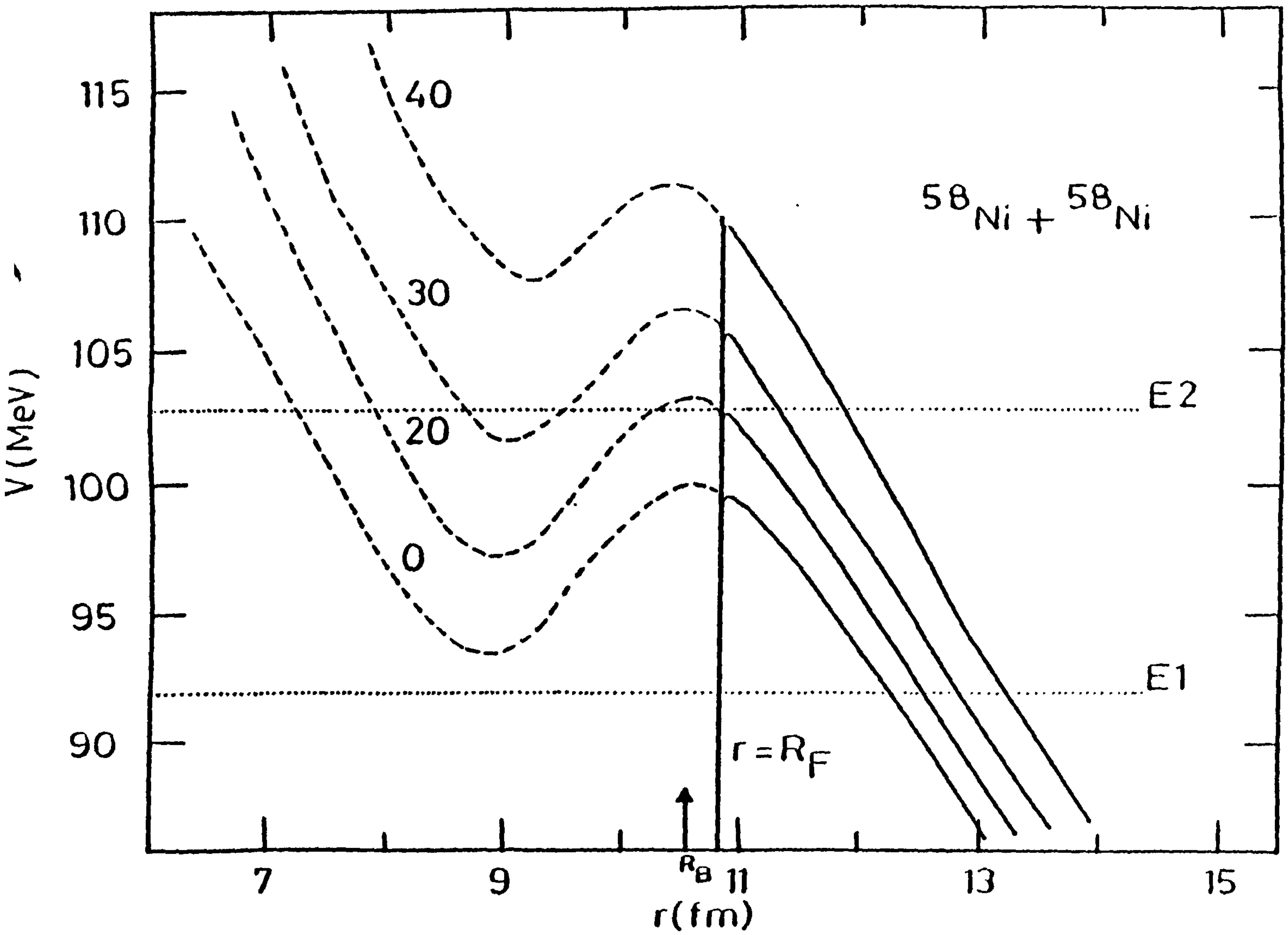

Fig.5.2.1 Variation of $V_{EFB}(l,r)$ (——) with r in the region $r > R_F = 10.83$ fm for a typical set of l for ^{58}Ni + ^{58}Ni. In the region $r < R_F$ dashed curves (-----) indicate variation of $V_{eff}(l,r)$ with r. When $r > R_F$, $V_{eff}(l,r) = V_{EFB}(l,r)$. Dotted lines (....) correspond to two typical incident energies, E1 and E2. Arrow indicates the Coulomb barrier position.

heights are denoted by V^{l}_{FB} and V^{l}_{B} in the cases of EFB model and total effective potential respectively. It is seen that V^{l}_{FB} for different partial waves in many cases is less than V^{l}_{B}, provided R_F is different from R_B ($R_B = r_B(A_F^{1/3} + A_T^{1/3})$), the Coulomb barrier position. Due to these and the condition in Eq.(5.2.2), the EFB model is found to be successful in explaining σ_F data in the sub-barrier region, in contrast to the earlier BPM. It has also been pointed out that [Sa 74], cutting off the total effective potential near a certain effective interaction region and assuming either vanishing or constant values of potential for smaller distances, has a negligible influence on the predicted elastic scattering cross section. Another point to be noted is that, in the BPM, sub-barrier and above barrier regions are identified based on two parameters namely, E, the centre-of-mass energy and the S-wave barrier height, V^{0}_{B} which is not fully justified. This can be understood in the following way. For a given energy $E = E_2 > V^{0}_{B}$ (as shown in Fig.5.2.1), $V_{EFB}(l,r) < E$ for several partial waves and for other partial waves ($l > 20$ in Fig.5.2.1) $V_{EFB}(l,r) > E$. The former corresponds to the above barrier fusion, while the latter to sub-barrier fusion and hence, for such energies both the aspects have to be taken into consideration.

Sahu and Shastry [Sa 89] have demonstrated that in the above barrier case the approximation $T_l = 1$ in SCM, is rather drastic. As the energy increases above the barrier, transmission coefficient approaches unity rather slowly. Comparison of transmission coefficients, T_F and T_C (where T_F is obtained by using a model potential and T_C by using the cut-off barrier of the same model potential) indicates that (i) below the barrier $T_C > T_F$ and (ii) above the barrier $T_C < T_F$. Morever, both the transmission coefficients approach unity rather slowly. Hence, by using results (i) and (ii) one can make the assumption that, in the case of nucleus-nucleus fusion, cutting off the potential may account for the enhancement of the experimental fusion data over the calculated values (obtained by using BPM with full barrier) and at the same time will be satisfactorily above the barrier also.

Based on the above observations, here we give more appropriate expression for $T_l(E)$. Using the WKB approximation one can find the transmission coefficient $T_l(E)$ for transmission across the barrier $V_{EFB}(l,r)$ which is given by [Sa 89]

$$T_l(E) = \left[1 + \exp\left(-2\int_{r_1}^{R_F} Q(r)dr\right)\right]^{-1}, \quad E \quad V_{FB}^{l} \qquad (5.2.4)$$

where

$$Q(r) = \left[\frac{2\mu}{\hbar^2}\left(V_{EFB}(l,r) - E\right)\right]^{1/2}.$$

Here r_1 is the outermost turning point. When E is very close to V_{FB}^{l} , but below the barrier top, Eq.(5.2.4) is not valid and the better approximation for $T_l(E)$ is

$$T_l(E) = \left[1/\theta + \theta/4\right]^{-2}, \qquad (5.2.5)$$

where

$$\theta = exp\left(\int_{r_1}^{R_F} Q(r)dr\right).$$

In the region where $E > V_{FB}^{l}$, $T_l(E)$ is given by

$$T_l(E) = \frac{4kF(r)}{(k+F(r))^2 + (F'(r)/2F(r))^2}\Bigg|_{r=r_F} . \qquad (5.2.6)$$

with $F(r) = \left[\frac{2\mu}{\hbar^2} \left(E - V_{EFB}(l,r) \right) \right]^{1/2}$ and $k^2 = 2\mu E/\hbar^2$

The transmission coefficients can be obtained by using Eq.(5.2.4), (5.2.5) or (5.2.6) at different energies below or above the barrier. Numerical analysis [Sa 89] shows that for almost all energies the comparison is quite satisfactory except for energies near but above the barrier. Hence, for those few partial waves for which E is close to V_{FB}^{l} but above it, the top of the barrier is assumed to be parabolic and the transmission coefficient is

$$T \simeq \left[1 + \exp\left(-2|M|\right) \right]^{-1}, \qquad (5.2.7)$$

where

$$M = \left\{ i \int_{x-iy}^{x+iy} Q(z)\, dz \right\} .$$

$x \pm iy$ are two complex conjugate zeros of $Q^2(z) = 2\mu(E-V(z))/\hbar^2$. Thus for those partial waves for which E is close to, but above V_{FB}^{l}, Eq. (5.2.7) has to be used instead of Eq.(5.2.6). Although this modification does not change the fusion cross section significantly, but in the study of σ_F as a function of l near the grazing l, Eq.(5.2.6) has its importance. Now the partial wave fusion cross section (σ_F^l) is given by

$$\sigma_F^l = (\pi/k^2)(2l+1)\, T_l(E) P_l(E). \qquad (5.2.8)$$

Here $k^2 = 2\mu E / \hbar^2$ and $P_l(E)$ is the energy dependent parameter indicating the probability of fusion. In the EFB model it has been assumed that $P_l(E) = 1$ in the energy region near the Coulomb barrier. With this approximation Eq.(5.2.8) becomes

$$\sigma_F^l = (\pi/k^2)\ (2l + 1)\ T_l(E)\ .$$

The total fusion cross section σ_F can be written as

$$\sigma_F = \sum_{l=0}^{\infty} \sigma_F^l$$

$$= \pi/k^2 \sum_{l=0}^{\infty} (2l + 1)\ T_l(E). \qquad (5.2.9)$$

Using the proper expressions for $T_l(E)$, σ_F can be calculated out. In the calculation of r_F, the cut-off l value is chosen in such a way that, for a given energy $T_l < 10^{-2}$, for $l > l_0$. Physically it is expected that $l_0 = l_{poc}$, where l_{poc} is that value of l for which $l > l_{poc}$ $V_{eff}(l,r)$ shows no pocket. It has been observed that for most of the systems $l_0 \leq l_{poc}$ in the energy range considered. In Table 5.2.2, a list of l_0 and l_{poc} for the highest energy, in the energy range studied, is given for five different systems. The fusion radius R_F is obtained by comparing experimental σ_F with the calculated value. The significance of r_F is discussed in Ref.[Sa 89].

Table 5.2.2 Energy range, $R_B - R_F$, l_O, l_{poc} for heavy ion systems.

System	range of E (MeV)	$R_B - R_F$ (fm)	l_O	l_{poc}	Reference. Expt.
$^{16}O + ^{63}Cu$	30-76	0.39	55	55	[Pe 89]
$^{16}O + ^{65}Cu$	30-76	0.35	55	55	[Pe 89]
$^{28}Si + ^{58}Ni$	47-63	0.483	32	56	[St 86]
$^{28}Si + ^{62}Ni$	48-58	0.329	35	56	[St 86]
$^{28}Si + ^{64}Ni$	47-64	-0.22	48	58	[St 86]

5.3 Results and Discussion

In this section we have applied this effective fusion barrier transmission model to study fusion barrier data of a few heavy ion systems like, $^{16}O + ^{63}Cu$, $^{16}O + ^{65}Cu$, $^{28}Si + ^{58}Ni$, $^{28}Si + ^{62}Ni$ and $^{28}Si + ^{64}Ni$ over a range of energies around V_B^0. The energy range studied for these systems is given in Table 5.2.2. Using Eqs. (5.2.4), (5.2.5) and (5.2.6), the transmission coefficients $T_l(E)$ can be obtained and substituting it in Eq. (5.2.9) fusion cross section σ_F can be calculated. Table 5.2.1 shows a list of the optical model parameters used in the calculation for all the above systems studied alongwith the values of other relevant quantities like, fusion radius parameter r_F, Coulomb barrier parameters V_B^0 and r_B. It is worth mentioning here that the same optical model parameters have been used for the entire energy range. The number of significant partial waves l_0 such that for l l_0, T_l 10^{-2}, at the highest energy of the energy range, and l_{poc}, i.e., the value of the partial waves beyond which pocket of the effective potential vanishes, have been found out for all these systems and a list is given in Table 5.2.2.

The fusion cross sections, which are obtained using EFB model, are plotted as a function of centre-of-mass energy E in Figs. 5.3.1 - 5.3.3. These results are compared with the available experimental data. While explaining σ_F^{Expt} it may be noted [Ba 80] that complete fusion is given by the sum of the cross sections due to evaporation residue formation and fusion followed by fission. However, at incident energies around V_B^0, the former alone practically accounts for the whole of σ_F in general. In Figs.5.3.1

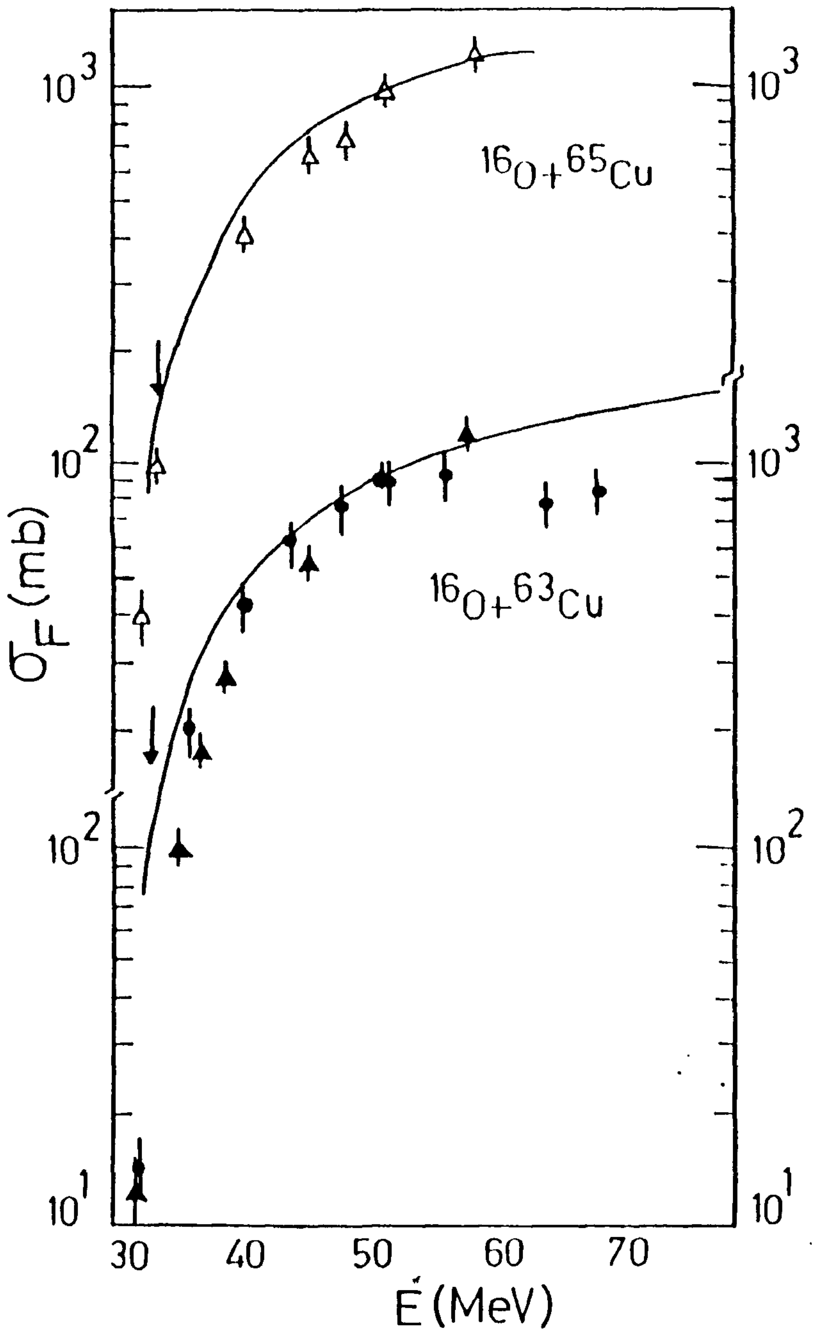

Fig. 5.3.1 Plot of fusion cross section σ_F as a function of incident centre-of-mass energy E for ^{16}O + $^{63,65}Cu$ systems. The solid curves correspond to EFB model . Arrows indicate Coulomb barrier heights V_B^0. The experimental points are represented by (⧫) and (▲) for ^{16}O + ^{63}Cu and Δ for ^{16}O + ^{65}Cu.

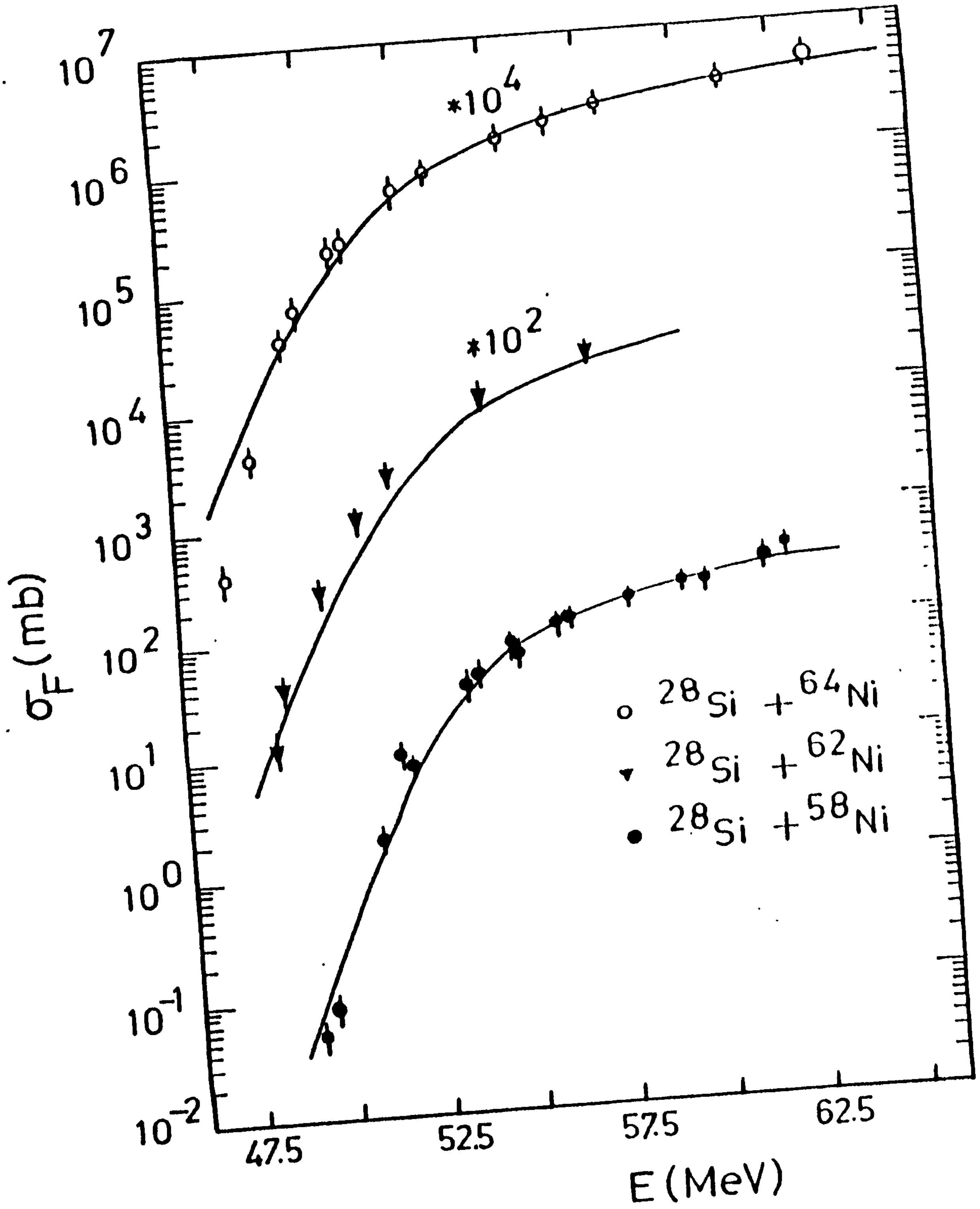

Fig.5.3.2 Same as Fig.5.3.1 for $^{28}Si + ^{58,62,64}Ni$ systems. The numbers indicated by stars (*) are read as 10^0 on the σ_F axis for the corresponding curve.

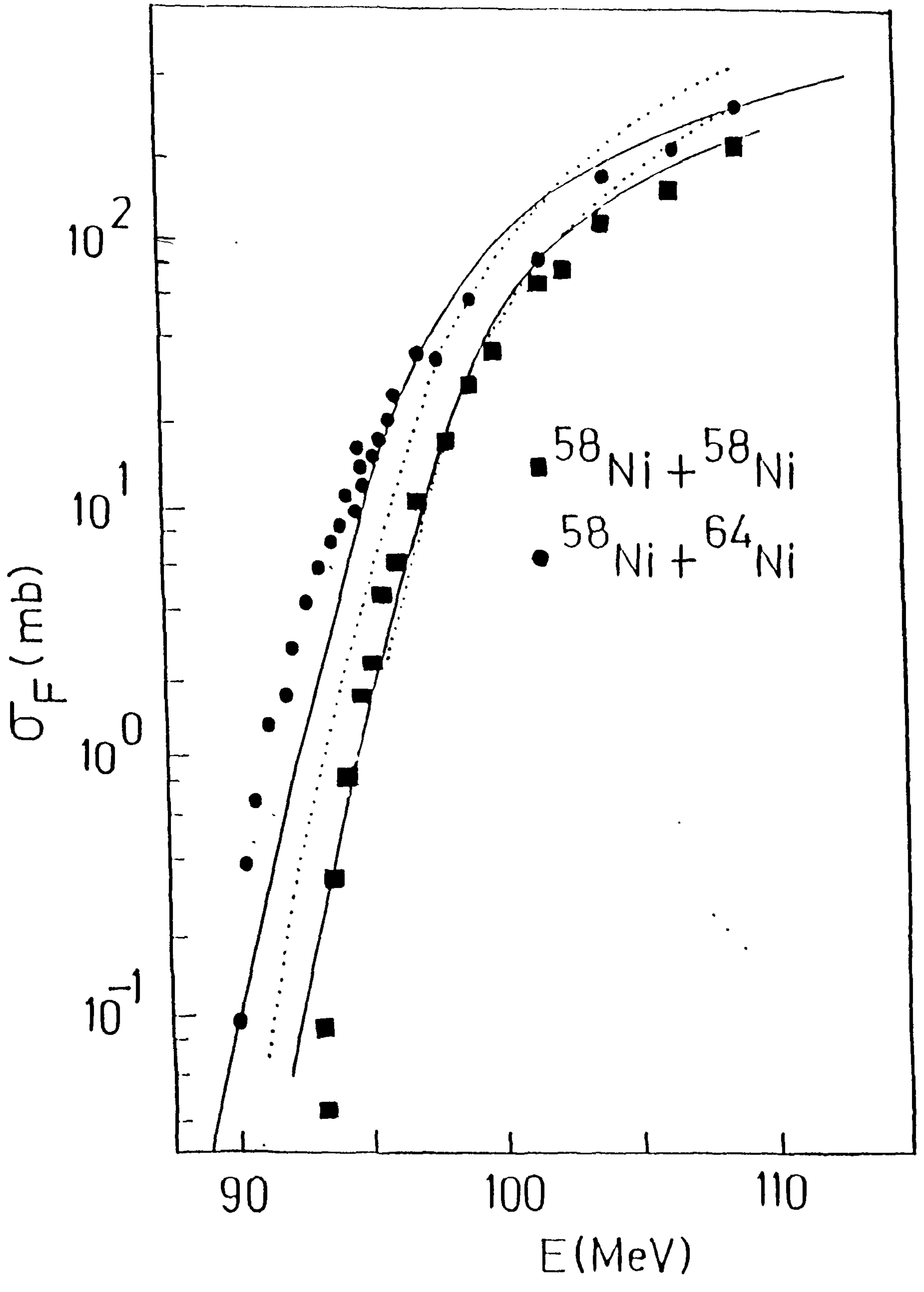

Fig.5.3.3 Comparison of σ_F calculated using EFB model and the DRM with the experimental data for ^{58}Ni + ^{58,64}Ni system. Solid curves, EFB model ; dotted curves, DRM.

and 5.3.2, we have illustrated the results of σ_F^{EFB} obtained by using EFB model as a function of E for the five pairs of nuclei listed in Table 5.2.1. In each figure the solid curve (——) corresponds to the results of σ_F^{EFB}. The results of σ_F^{EFB} for ^{16}O + $^{63,65}Cu$ systems are shown in Fig. 5.3.1. The corresponding results of σ_F^{EFB} for ^{28}Si + $^{58,62,64}Ni$ systems are shown in Fig.5.3.2. The experimental points are denoted by solid triangles and circles for ^{16}O + ^{63}Cu and open triangles for ^{16}O + ^{65}Cu correspond to evaporation residue cross section [Pe 89]. From these figures it is seen that the fit of σ_F^{EFB} to σ_F^{Expt} is reasonably good. Thus EFB model is quite successful as a general macroscopic method for analysing the fusion data around the Coulomb barrier.

For relative comparison we have shown the results of fusion cross section obtained by using both DRM and EFB models for ^{58}Ni + $^{58,64}Ni$ systems in Fig.5.3.3 [Sa 89]. From Figs. 5.3.3 it is clear that in the case of ^{58}Ni + ^{58}Ni, both the models give equally good fits to the experimental data. However in the case of ^{58}Ni + ^{64}Ni system the fit of EFB model is much better than that of DRM. It has been seen that in some cases, DRM results are superior to that of EFB model. It may, however, be noted that results of DRM are obtained by changing the optical model parameters suitably, whereas in EFB model, energy independent optical model parameters are used. Good agreement of the EFB result ascertains the fact that EFB and DRM models of fusion essentially describe the same physical process in two different and complementary ways within the framework of macroscopic approach.

5.4 Summary and Conclusion

In this section we briefly summarise the work discussed in this thesis. The thesis contains the investigations of several features of antiproton-nucleus scattering and some aspects of heavy ion scattering. The low energy antiproton-nucleus scattering has opened up a new field of research in nuclear reactions which has interesting implications in the study of nuclear matter, strange particle production, antiprotonic atoms, etc. In Chapter 2, we have given a brief review of several accumulated results of antiproton-nucleus scattering. The main thrust of this thesis is on the comparative study of antiproton-nucleus scattering and heavy ion scattering and the applicability of several techniques used in heavy ion scattering to the analysis of antiproton-nucleus scattering. The whole work comes within the broad framework of nuclear optical model. The semiclassical and other related theoretical analyses have greatly helped to understand diffractive, refractive, absorptive and resonance aspects of heavy ion scattering. On the basis of several similarities between antiproton-nucleus scattering and heavy ion scattering, we have investigated the applicability of theoretical techniques developed for heavy ion scattering to the analysis of antiproton-nucleus scattering. At present the experimental data in antiproton-nucleus scattering is considerably less extensive as compared to that in heavy ion scattering, particularly polarisation and differential cross section data at large angles which are yet to be accumulated. Similarly in the absence of cross section data over a continuous range of energies, features like possible resonance phenomena are not yet available from experiments. However, we believe that as more diverse data become available in antiproton-nucleus scattering at low energies, the theoretical techniques studied in this thesis will be useful in the analysis and physical interpretation of the data. This thesis also contains some calculation of nucleus-nucleus fusion within the framework of effective barrier model which gives a comprehensive understanding of the direct reaction model based on optical potential in the interior region and the barrier penetration model where the effective potential in the barrier region is most important.

In chapter I, we have studied semiclassical and closed formalism approaches to antiproton-nucleus scattering. A smooth behaviour in the effective potential of antiproton-nucleus interaction suggests that, one-turning point WKB approximation can be applied successfully to study $\bar{p}$-A scattering. Using this approximation, closed form expressions for nuclear phase shifts have been obtained which were then used to find the scattering cross sections. The method was illustrated by carrying out the cross section calculations of $\bar{p}+^{12}C$ and $\bar{p}+^{40}Ca$ scattering systems at E_{lab} = 46.8 MeV. The study of closed formalism or parametric S matrix approach, using two well known parametrisation schemes of nuclear S matrix, gives a good fit to the $\bar{p}$-A scattering data. Few typical scattering data for $\bar{p}$-A systems like, $\bar{p}+^{12}C$, $\bar{p}+^{40}Ca$ and $\bar{p}+^{208}Pb$ at E_{lab} = 46.8 MeV and $\bar{p}+^{12}C$ at E_{lab} = 180 MeV, have been analysed using parametric S matrix approach, which were then compared with the experimental data. The results indicate that the closed formalism approach which was applied earlier for the analysis of heavy ion scattering data can be successfully applied in the case of antiproton-nucleus scattering data as well.

In chapter 4, we have examined the relative importance of different regions of antiproton-nucleus optical potential in generating the total reaction cross section using the method of region-wise absorption, as formulated in heavy ion scattering. It has been found that in antiproton-nucleus collision most of the contribution to reaction cross section comes from the surface region which is peaked at $\sim$ 3.4 fm for $\bar{p}$ + ^{12}C at E_{lab} = 46.8 MeV and $\sim$ 4.61 fm for $\bar{p}$ + ^{40}Ca at the same value of E_{lab}. We have also estimated the mean free path of antiproton inside the nucleus and obtained the radial positions R_1 and R_2 where the corresponding mean free paths are about 1 fm and 2 fm repectively. From our study of region-wise absorption it was observed that the peak of region-wise absorption takes place around the region where the mean free path is about 2 fm. Using the method of region-wise absorption, together with the estimate of antiproton mean free path inside the nucleus and the critical distance for $\bar{p}$-p annihilation, it was estimated that the contribution of annihilation cross section to reaction cross section would be about 50% or more. The time scale involved in $\bar{p}$-A collision using classical Coulomb-nuclear trajectory was estimated. The time spent by antiproton in the classical Coulomb-nuclear trajectory was found to be approximately in the range 10^{-23} - 10^{-22} seconds. It was also found that the time elapsed for different partial waves within the region r R_c (R_c, the Coulomb radius) for a given nucleus at a given energy were practically same except for the peripheral partial waves where they gradually fall off. This result is also very similar to the corresponding result as in the case of heavy ion scattering.

In chapter 5, heavy ion fusion cross section, using the effective fusion barrier transmission model have been studied around the Coulomb barrier region. Good agreement of the calculated fusion cross section data with the corresponding experimental result establishes the fact that, effective fusion barrier transmission model, which has been applied earlier, can be widely applied to the analysis of heavy ion fusion cross section near the Coulomb barrier region. This model for fusion is complementary to the direct reaction model of fusion developed by Udagawa et al.

Reference

[Ba 80] Bass. R, *Nuclear reactions with heavy ions* (Springer Verlag New York, 1980)

[Bi 83] Birkelund. J.R and Huizenga, J.R Ann.Rev. Nucl.and Part. Sci., **33**(1983) 265

[Br 85] Brink. D.M, *Semiclassical methods in nucleus-nucleus scattering* (Cambridge University Press, 1985) p.177

[Ch 77] Christensen. P.R and Switkowski. Z.E, Nucl.Phys. **A280** (1977) 205

[Fr 65] Froman. N and Froman. P.O, *JWKB approximation contribution to the theory* (Amsterdam North-Holland Publishing Co, 1965) p.101

[Hi 53] Hill. D.L and Wheeler. J.A, Phys.Rev. **89**(1953) 1102

[Ng 86] Ngô. Ch, *Progress in particle and nuclear physics*, Vol.**16** Ed.by A. Faessler (Oxford, Pergamon, 1986) p.139

[Pe 89] Pereira. D et al., Phys.Lett. **220B**(1989) 347

[Rh 86] Rhoades-Brown. M.J, *Annual review of nuclear and particle science* **36** Ed. by J.D.Jackson (Annual Reviews Inc. Palo. Alto, USA, 1986) p.649

[Sa 74] Satchler. G.R, *Proceedings of the international conference on reaction between complex nuclei*, Nashville, June 1974, Ed. by R.C.Robinson, F.K.McGowan, J.B.Ball and J.H.Hamilton (North-Holland, American Elsevier, 1974) p.171

[Sa 89] Sahu. B and Shastry. C.S, J.Phys.G: **15**(1989) L149

[St 86] Stefanini. A.M et al., Nucl.Phys. **A456**(1986) 509

[St 87] Stefanini. A.M et al., Phys.Lett. 185B(1987) 15

[Ud 84] Udagawa. T, and Tamura. T, Phys.Rev. C29(1984) 1922

[Ud 85] Udagawa. T, Kim. B.T and Tamura. T, Phys.Rev. C32 (1985)124

[Va 81] Vaz. L.C, Alexander. J.M and Satchler. G.R, Phys.Rep. 69 (1981)373